

Magnetorheological Fluids for
Controlling Pharmaceutical Crystal
Growth

Rodolfo Andres Estrada Tun

MSc by Research

University of York

Chemistry

April 2018

Abstract

Magnetorheological (MR) fluids are suspensions of magnet iron microparticles known as carbonyl iron (CI). MR fluids have the ability to increase in viscosity and display high yield stress with the application of an external magnetic field. Herein we explore the feasibility of using these materials to influence the crystallisations of active pharmaceutical ingredients in an attempt to affect crystal morphology. Within the context of this study we developed a range of magnetorheological fluids by modifying carbonyl iron (CI) particle surfaces with a series of ligands. We used acid terminated PEG, oleic acid, carminic acid and 1-naphthaleneacetic acid as the functionalising ligands. We demonstrated control over crystal morphology in carbamazepine (CBZ) with the use of MR fluids. We managed to selectively crystallise form II of CBZ in PEG and carminic acid functionalised CI, and form III (commercially available/active form) with oleic acid and 1-naphthaleneacetic acid functionalities.

The second part of this study was concerned with improving the heat generation efficiency of iron oxide nanoparticles (NPs) for thermotherapy. Iron oxide NPs can generate heat loss through interaction with an alternating magnetic field (AMF). It was shown in the literature that a “tight” clustering of nanoparticle clusters can be used to increase heat generation efficiency. We therefore investigated the effect of coupling a temperature sensitive polymer (with a LCST of 32 °C), poly-N-isopropyl acrylamide (PNIPAM), to a “tight” clustering of magnetic iron oxide nanoparticles. The aim was that this coupling could produce a temperature induced aggregation of the NP clusters, concentrating them and therefore increasing the total heating power. Unfortunately, modification of PNIPAM for coupling resulted in an unknown product that failed to exhibit the desired properties.

Table of Contents

Abstract	2
List of Abbreviations.....	6
List of Figures	7
List of Tables	10
Acknowledgments	11
Author's Declaration	12
Chapter 1. Introduction	14
1.1 Magnetic Micromaterials.	14
1.2 MR Fluid Composition and Properties	14
1.3 Rheology Fundamentals.	15
1.4 MR Foams	17
1.5 MR Elastomers	17
1.6 Magnetic Nano Materials	18
1.7 Synthesis and Properties.....	19
1.8 Surface Modification and Targeting Ability	21
1.9 Conclusion	23
Research Objectives	24
Chapter 2. Magnetorheological Fluids for Controlling Pharmaceutical Crystal Growth	26
2.1.1 Crystallisation and Polymorphism.	26
2.1.2 Crystal Engineering in Confined Spaces.....	28
2.1.3 Magnetorheological Fluids	30
2.2 Adapting Magnetorheological Fluids for Crystallisations	32
2.3 Properties of Carbonyl Iron (CI) Particles	32
2.4 Surface Modification of Carbonyl Iron.....	35
2.5 Surface Modification of Carbonyl Iron with mPEG-NDA	42
2.6 Surface Modification with Carboxylic Acid Moieties	44
2.7 Crystallisation of Carbamazepine in Toluene MR Fluids.....	50
2.8 Crystallisation of Carbamazepine in water MR Fluids	56

2.9 Separation of CBZ Crystals from MR Fluid	58
2.10 Conclusion	59
Chapter 3. Synthesis and Surface Modification of Magnetite (Fe₃O₄) Nanoparticle clusters	61
3.1 Background	61
3.2. Synthesis of Iron Oxide Clusters	62
3.3 Polymer Synthesis and Characterization	66
3.4 Functionalisation of Clusters	72
3.5 Thermally Induced Aggregation	75
3.6 Conclusion	76
Chapter 4. Experimental	79
4.1. MR Fluids for Controlling Pharmaceutical Crystal Growth	79
Materials	79
Preparation of magnetic suspensions	79
Synthesis of acid terminated mPEG	79
Synthesis of NDA terminated mPEG	80
Functionalisation of CI with Carboxylic Acid Moieties	80
Crystallisation of Carbamazepine in Toluene	81
Crystallisation of Carbamazepine in Water	81
Hydrolysis of PEG Ligands for Characterisation of Functionalised CI	81
Maleic Acid Displacement of Carboxylic Acid Moieties for Characterisation of Functionalised CI	81
4.2. Synthesis and Surface Modification of Magnetite NP Clusters	82
Materials	82
Initial Cluster synthesis	82
Modified Cluster Synthesis	82
PNIPAM Synthesis	82
Synthesis of ethylenediamine-coupled PNIPAM (A-PNIPAM)	83
Functionalisation of Iron Oxide Clusters with A-PNIPAM	84
Characterisation	84
Chapter 5. Conclusions and Future Work	85
Future Work	85

References	86
Appendix	91
Estimating the mass of PEG polymer required for functionalisation of carbonyl iron	91
Calculating the grafting density of PEG on carbonyl iron from qNMR	91
Estimating the efficiency of functionalisation from UV-Visible Spectroscopy data	92
Grafting Density Calculations for Magnetite NP Clusters.....	92
Bare Clusters	92
A-PNIPAM Clusters	93

List of Abbreviations

A-PNIPAM	Amine modified Poly-N-isopropyl acrylamide
AMF	Alternating Magnetic Field
API	Active Pharmaceutical Ingredient
CBZ	Carbamazepine
CI	Carbonyl Iron
DLS	Dynamic Light Scattering
IUT	In-Use-Thickening
LCST	Low Critical Solution Temperature
LMWG	Low Molecular Weight Gel
mPEG	Poly(ethylene glycol) methyl ether 5000
MR	Magnetorheological
NDA	Nitrodopamine Anchor
NP	Nanoparticle
PNIPAM	Poly-N-isopropyl acrylamide
PPy	Polypyrrole
PVA	Polyvinyl alcohol
PyCOOH	Pyrrole-3-carboxylic acid
SPM	Superparamagnetic
T _g	Glass Transition Temperature
TGA	Thermogravimetric Analysis
TOC	Total Organic Content
COMU	(1-Cyano-2-ethoxy-2-oxoethylideneaminoxy) dimethylamino-morpholino-carbenium hexafluorophosphate

List of Figures

Figure 1.3.1. Schematic Representation of simple shear flow. Reprinted from [2].

Figure. 1.4.1 The basic elements of MR foam. Reprinted from [6]

Figure 1.7.1. (A) TEM image of 16 nm Fe₃O₄ NPs. Copyright 2002 American Chemical Society. (B–D) TEM images of (B) 7 ± 0.5 nm, (C) 8 ± 0.4 nm, and (D) 10 ± 0.8 nm Fe₃O₄ NPs. The scale bars are 20 nm. Copyright 2009 American Chemical Society. (E) TEM image of octahedral Fe₃O₄ NPs. Copyright 2009 Royal Society of Chemistry. (F) TEM image of Fe₃O₄ nanoprisms. Copyright 2010 Royal Society of Chemistry. TEM images of (G) 14 nm spherical and (H) 32 nm and (I) 53 nm truncated octahedral FeO NPs and (J) SEM image of truncated octahedral FeO NPs. Figure is a reprint from [21].

Figure 1.8.1. 10.7 nm/PNIPAM 20 kDa, 5 mg/mL in a poly(methyl methacrylate) (PMMA) cuvette placed upon a neodymium magnet, (A) at room temperature, (B) at 40 °C. In plastic cuvettes, a discoloration of the cuvette wall remains, interpreted as a high affinity of the dehydrated PNIPAM for the cuvette walls. Reprint from [38].

Figure 1.8.2. Schematic Representation of (a) liposomes containing iron oxide NPs in their bilayer (reprint from [41]) and (b) clustered iron oxide NPs encapsulating DOX in its polymer functionality (reprint from [39]).

Figure 2.1.1. Schematic Representation of the pathway leading from solution to solid showing (a) supersaturated solution, (b) ordered subcritical cluster of solute molecules, (c) ordered crystalline nuclei, and (d) solid crystal. Image and caption are a reprint from [44].

Figure 2.1.2. Hydrogen bonding network for Ritonavir (a) form I and (b) form II. Reprint from [49].

Figure 2.1.3. (a) and (b) are surface structures of form II facets preferentially nucleated on polymer surfaces. (c) Surface structure of a facet characteristic of form I not grown from polymer surface. (d) Functionality in CBZ inferred to interact preferentially with PEGDA polymer (colored blue). Image and caption are a reprint from [58].

Figure 2.1.4. Schematic Representation of a magnetorheological damper. Reprint from [62].

Figure 2.1.5. Schematic Representation demonstrating the MR effect in response to a magnetic field.

Figure 2.3.1. Reaction scheme for the decomposition of iron pentacarbonyl.

Figure 2.3.2. SEM images of bare carbonyl iron particles.

Figure 2.3.3. Schematic Representation of MRF setup

Figure 2.3.4. Images displaying MR fluid in (a) 0 G field, (b) 1000 G field, (c) upside-down in 1000 G field and (d) upside-down in 0 G field.

Figure 2.4.1. Synthetic scheme for Nitrodopamine PEG

Figure 2.4.2. FTIR spectra mPEG, Carboxylated mPEG and mPEG-NDA

Figure 2.4.3. (a) UV-Visible absorption spectra of functionalised mPEG-NDA and (b) calibration curve obtained from UV-Visible spectra of nitrodopamine (NDA).

Figure 2.4.4. ¹H NMR Spectra of (a) mPEG, (b) carboxylated mPEG and (c) mPEG-NDA.

Figure 2.4.5. MALDI-TOF mass spectra of mPEG, carboxylated mPEG and mPEG-NDA.

Figure 2.5.1. UV-Visible absorption spectra during functionalisation with mPEG-NDA of (a) bare CI in PBS, (b) bare CI in DMF.

Figure 2.5.2. (a) optical image of water droplet on powder of oleic acid functionalised CI and (b) a graphical representation of functionality attached to the particle surface.

Figure 2.6.1. Carbonyl iron functionalities employed in this study. (a) Carboxylated mPEG, (b) carminic acid, (c) 1-naphthaleneacetic acid and (d) oleic acid.

Figure 2.6.2. Schematic Representation for the quantification of PEG adsorbed onto CI

Figure 2.6.3. Optical image of water droplet on powder of (a) mPEG-CI, (b) 1-naphthaleneacetic acid-CI and (c) carminic acid-CI.

Figure 2.6.4. SEM images of (a) Carminic acid-CI, (b) 1-naphthaleneacetic acid-CI and (c) PEG-CI.

Figure 2.6.5. UV-Visible absorption spectra during the functionalisation of CI with carminic acid.

Figure 2.7.1. Optical microscopy (10x magnification, 1.6 mm field of view) of CBZ grown in toluene containing no CI.

Figure 2.7.2. Optical microscopy (10x magnification, 1.6 mm field of view) of CBZ grown in toluene containing (a) bare CI, (b) PEG-CI and (c) Oleic acid-CI in a 200 G magnetic field.

Figure 2.7.3. Optical microscopy (10x magnification, 1.6 mm field of view) of CBZ grown in toluene containing (a) bare CI, (b) PEG-CI, (c) Oleic acid-CI and (d) 20uL of Oleic acid in a 1000 G magnetic field.

Figure 2.7.4. Packing diagrams of (a) form I, (b) form II, (c) form III and (d) form IV of CBZ showing hydrogen-bonding patterns. Reprint from [78].

Figure 2.7.5. Optical microscopy (10x magnification, 1.6 mm field of view) of CBZ grown in toluene containing (a) carminic-CI, (b) naphthalene-CI in a 1000 gauss magnetic field.

Figure 2.8.1. Optical microscopy (10x magnification, 1.6 mm field of view) of CBZ grown in water containing (a) pure solvent, (b) Bare-CI, (c) PEG-CI, (d) Oleic acid-CI, (e) Carminic-CI and (f) Naphthalene-CI in a 1000 G magnetic field.

Figure 3.2.1. Schematic Representation of nanoparticle cluster synthesis

Figure 3.2.2. TEM images of (a) Fe_3O_4 clusters prepared with 3.8% PVA, (b) Fe_3O_4 clusters prepared with 7% PVA and (c) Fe_3O_4 clusters functionalised with PNIPAM.

Figure 3.2.3. Changes in shape factor as a function of PVA concentration. Reprint from [86].

Figure 3.3.1. Coupling mechanism for COMU in the reaction between ethylenediamine and PNIPAM with DIPEA as the base.

Figure 3.3.2. Synthesis of amine functionalised PNIPAM

Figure 3.3.3. ^1H NMR spectra of (a) PNIPAM and (b) A-PNIPAM

Figure 3.3.4. FT-IR spectra of (a) bare clusters, functionalised clusters, PNIPAM and A-PNIPAM and (b) selected region of PNIPAM and A-PNIPAM.

Figure 3.3.5. MALDI-TOF mass spectra of PNIPAM and A-PNIPAM where the zoomed in regions show mass peaks of a series are separated by 113 Da.

Figure 3.4.1. FT-IR spectra of bare clusters and clusters functionalised with A-PNIPAM.

Figure 3.4.2. TGA Curves for Bare (Un-functionalised) and A-PNIPAM functionalised Clusters.

Figure 3.5.1. DLS data showing cluster size (blue line) and count rate (red line) vs temperature of (a) bare clusters and (b) A-PNIPAM clusters. Where three measurements were taken every 5 °C with an equilibration time of 5 min per measurement.

List of Tables

Table 1.3.1. Comparison of measured dynamic yield stresses for 40 vol% MR fluids containing coarse or fine powder.

Table 2.6.1. Quantitative NMR Spectroscopy results from the hydrolysis of PEG-Cl

Table 2.7.1. Known polymorphs of Carbamazepine (CBZ)^(b).

Table 2.7.2. Summary of crystallisations of CBZ in toluene MR fluids at 1000 gauss.

Table 3.4.1. Properties of Bare and Functionalised Clusters.

Acknowledgments

I would like to thank Dr. Chechik for his patience, wisdom and support, for without him none of this would be possible.

To my parents, for accepting nothing less than excellence and for always being there for me.

Author's Declaration

The work presented in this thesis is my own and I am the sole author. This work has not previously been presented for an award at this, or any other, University. All sources are acknowledged as References.

Chapter 1

Introduction

Chapter 1. Introduction

1.1 Magnetic Micromaterials. Magnetorheological (MR) materials are fluids composed of soft magnetic particles dispersed in a non-magnetic fluid medium. The properties of these fluids can switch between a fluid-like state and a solid-like state in milliseconds by controlling the strength of an applied magnetic field [1]. The properties of MR fluids are a result of induced dipoles leading the particles to form chain-like structures parallel to the direction of the applied magnetic field [2]. The magnetic particles are also applied to materials such as elastomers and foams to induce an MR effect and realise a wide range of flow and shear properties [3]. The variable rheological properties of MR fluids have found widespread use in industry, where their discovery stemmed from an extensive research programme to overcome the speed limitations of computers in 1948 [4]. Their applications now range from dampers such as those in braking and shock absorbing systems in vehicles, to force sensors in bridge bearings [5].

1.2 MR Fluid Composition and Properties. MR fluids contain a high concentration of magnetisable particles. Differences in particle size and concentration can produce significant differences in the behaviour of the fluid [6]. Particle sizes typically range from 0.1 – 10 μm , and larger particles will support many hundreds of magnetic domains. This is important because a larger number of magnetic domains translates into maximum inter-particle attraction and magnetorheological effect [2]. Optimising conditions for a maximum magnetorheological effect also means choosing a particle material with a high saturation magnetisation, M_S [7]. In terms of pure metals, this material is iron, which has a saturation magnetisation of $2.21 \mu_B$ [8].

Saturation magnetisation is the property of magnetic materials that determines the maximum amount of magnetisation the material can hold. It is the point at which any increases in magnetic field cannot affect the magnetisation of the material. Magnetisation, M is related to magnetic induction or magnetic flux density, B , expressed by the following relationship:

$$B = \mu_0(H + M) \quad (1)$$

Where μ_0 is the permeability of free space and H is the induced magnetic field. The magnetic response of these materials also varies linearly with the applied magnetic field, H , and this is referred to as susceptibility (dimensionless quantity), χ :

$$\chi = \frac{M}{H} \quad (2)$$

Both magnetisation and susceptibility of the magnetic material play important roles in the design of an MR fluid [9]. These properties lead to variations in the intensity of the magnetorheological effect displayed by the MR fluid. The high saturation magnetisation of iron is the reason why the most common magnetic material used in the preparation of MR fluids is pure iron. This is also referred to as carbonyl iron, because it is produced from the thermal decomposition of iron pentacarbonyl [10].

The carrier fluid is typically chosen based on its rheological properties and temperature stability. Considering that many MR fluids are used in moving parts, it is important that the viscosity of the carrier fluid is low and independent of temperature. This is why many lubricants and oils are used as carrier fluids, because in the ‘off’ state their natural viscosities will not interfere with the workings of the mechanism [11].

It is also important to note that MR fluids can often contain other additives to improve lubrication and reduce sedimentation of the particles in the carrier. Sedimentation is often controlled by the addition of thixotropic agents such as silica gels [12] and surfactants such as stearates and carboxylic acids [13]. However, during development and commercialisation of MR products, it became apparent that the high stress and high shear rates over time led to the thickening of the MR fluids, known as “In-Use-Thickening” (IUT). This phenomenon describes behaviours observed in MR fluids that have been in service for long time periods, where the ‘off’ state viscosity increases to a point where the fluid compromises the functionality of the product. The cause of IUT has been identified as a result of nano-sized particulates being expelled from the surface of the iron particles from shear forces, leading to thickening of the fluid [12].

1.3 Rheology Fundamentals. In its simplest form, rheology is the study of the flow and deformation of matter. The field-dependent chaining of particles in an MR fluid produces

forces that resist deformations from shear stress without breaking, which is what gives the fluid its solid-like appearance [14]. Shear stress arises from resistance to a force component parallel to the cross-section of the material (Fig. 1.3.1) [15]. The value required to exceed the shear stress, leading to the breakdown of the structure, is referred to as the yield stress of the material. The data in Table 1.3.1 demonstrates how the yield stress of typical MR fluids increases as a function of magnetic field strength.

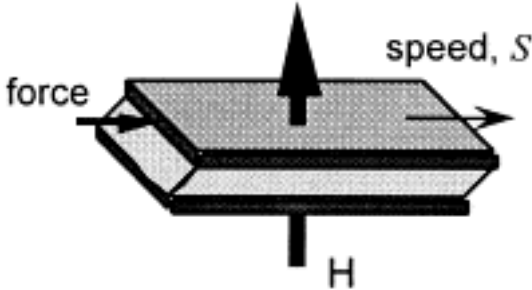


Figure 1.3.1. Schematic Representation of simple shear flow. Reprinted from [2].

Table 1.3.1. Comparison of measured dynamic yield stresses for 40 vol% MR fluids containing coarse or fine powder.

Magnetic Field Strength (G)	Coarse CI Powder (7-9 μm)	Fine CI Powder (2 μm)
	Measured Dynamic Yield Stress (kPa)	
2000	22 \pm 1	14 \pm 1
4000	45 \pm 3	35 \pm 1
6000	84 \pm 2	71 \pm 2
8000	124 \pm 3	102 \pm 2

*Data was collected and organised from [10].

We can therefore model the field dependent behaviour of MR fluids as Bingham plastics where the shear stress, τ is a function of the sum of the field dependent yield stress τ_y and the dynamic viscosity, η :

$$\tau = \tau_y + \eta\gamma \quad (3)$$

Dynamic viscosity is defined as:

$$\eta = \frac{\tau}{\gamma} \quad (4)$$

Where γ is the shear rate [2, 11, 14].

The rheological properties of MR fluids, specifically the display of high yield stress, makes these materials very attractive for mechanical applications. However, their off-state rheological properties make the application of MR fluids to odd geometries difficult. Problems such as these have led to increased interest in MR foams.

1.4 MR Foams. To keep MR fluids in the active region of a device, an absorbent matrix such as a sponge or open-celled foam is used as a lining containing the MR fluid. The fluid is thereby constrained by capillary action in the absorbent matrix [16]. As seen in the image below (Fig. 1.4.1) the absorbent matrix is attached to one of the poles. Applying a magnetic field produces a yield strength in the foam, and therefore a resistance to shear motion. Due to the variable shapes that the foams can adopt, MR fluid foams can be applied to both linear and rotary devices [2]. Furthermore, these devices are free of the sedimentation issues normally faced in MR fluids because of the capillary action of the matrix. This action allows the foams to retain the fluid even in the absence of a magnetic field.

Reported leakages from MR devices have led to concerns around environmental contamination [17]. To combat these issues, MR elastomers are being investigated as replacements.

1.5 MR Elastomers. MR elastomers differ from foams and fluids in that the carrier fluid is a polymer medium. Therefore, the application of a magnetic field results in a field dependent modulus, as opposed to a field-dependent yield stress. Hence, elastomers find more use in the application of shock absorption rather than dampening [18]. Although the

applications of elastomers are few, their ability to affect stiffness suggests the potential for use in devices that require variable stiffness such as vibration absorbers in propeller aircraft [19].

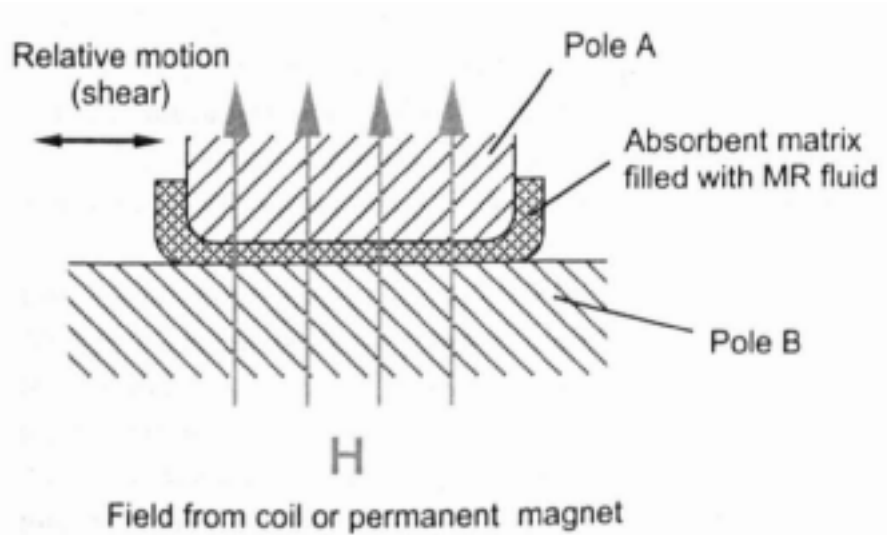


Figure. 1.4.1 The basic elements of MR foam. Reprinted from [6].

1.6 Magnetic Nano Materials. The important role of nanomaterials is evidenced by their ubiquity in the consumer market, from beauty to healthcare products, and the broad range of disciplines they encompass, from agriculture to space technology [20]. The unique properties of these materials stem from their nanoscale (1 – 100 nm) behaviours. Of particular interest is the property of superparamagnetism in iron oxide nanoparticles, which is a result of thermal fluctuations on very small ferromagnetic clusters within the particle [21]. This property (described in more detail in the next section) manifests in induced magnetisation under an applied magnetic field and no observed magnetisation in the absence of a magnetic field, making them readily stable in physiological conditions [22]. Furthermore, to be superparamagnetic, the particles must be below a critical size. For iron, this is < 20 nm, below which the particles experience spontaneous magnetisation reversal and hence no net magnetisation in the absence of a field [23]. The small size of superparamagnetic (SPM) nanoparticles (NPs) and their strong magnetic response makes them attractive materials for biomedicine, where they can be used as magnetic probes for bio imaging and therapeutic

applications [24]. In the next section, we will concentrate on monocomponent nanomaterials such as iron oxide.

1.7 Synthesis and Properties. In the past, iron oxide nanoparticles (NPs) for magnetic fluids were commercially manufactured by the mechanical grinding of magnetite (Fe_3O_4) in the presence of surfactants, producing large particle size distributions. Therefore, the pioneering synthesis of monodisperse iron oxide nanoparticles by the decomposition of iron pentacarbonyl in the presence of oleic acid, was well received [25]. However, the demand for superparamagnetic nanoparticles led research to achieve more precise size and distributions. These investigations into organic phase methods indicated that particle size could be tuned by controlling the ratio of surfactant to solvent (Fig. 1.7.1A-D) [26, 27]. Furthermore, particle geometries such as the octahedral Fe_3O_4 NPs and the Fe_3O_4 nanoprisms seen in Fig. 1.7.1 E and F were also a result of controlling surfactant concentrations. The octahedral NPs were formed in a 1:2 molar ratio of iron (III) oleate to oleylamine, where altering the ratios to 4:1 or 1:1 produced irregular octhedra (Fig 1.7.1E) [28]. Nanoprisms formed as a result of an oleylamine surfactant and a high pressure synthetic method. This high pressure from the autoclave allowed oleylamine to preferentially bind to (111) facets, slowing those facet growths and leading to a prism-like geometry (Fig 1.7.1F) [29].

Although surfactant ratio can regulate competitive growth to produce specific morphologies, temperature control can produce other oxidation states and facilitate size control. Fig. 1.7.1 G-J demonstrates size and morphology control of FeO obtained by varying heating parameters [30].

The magnetic behaviour of a material can vary depending on the structure and its electron configuration. The relevant magnetic properties of superparamagnetic (SPM) NPs are described by the Néel-Arrhenius equation:

$$\tau = \tau_0 \exp\left(\frac{\Delta E}{k_B T}\right) \quad (5)$$

Where ΔE is the energy barrier to the reversal of the magnetic moment, $k_B T$ is the thermal energy and τ is the time between magnetisation flips. Considering that ΔE is equal to the product of the anisotropy constant and volume of the particle, superparamagnetism is only

observed in very small particle geometries. Because only at this scale is ΔE comparable to the thermal energy, $k_B T$ at room temperature [31, 32]. This explains why the flipping of magnetic moments happens spontaneously at room temperature for SPM NPs.

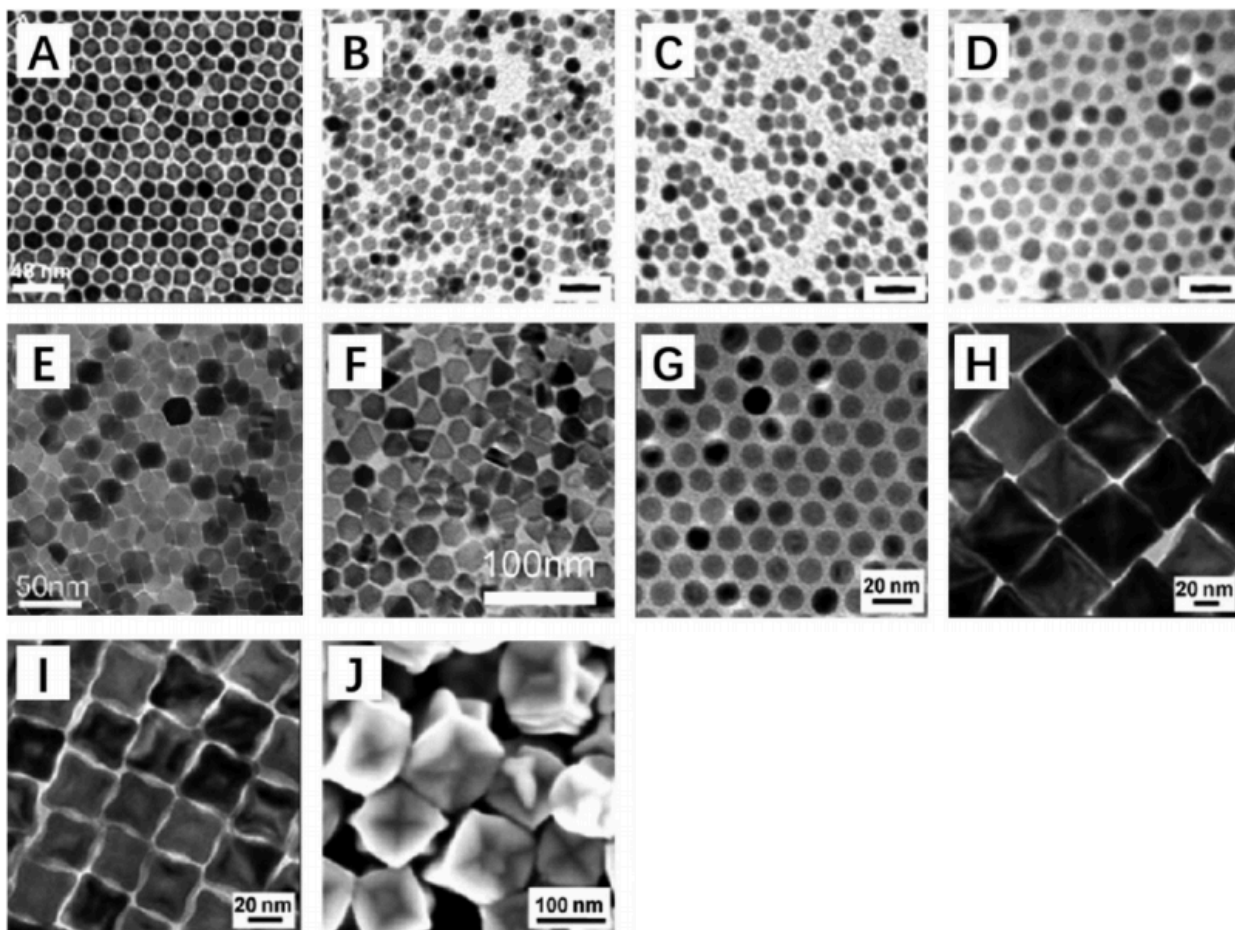


Figure 1.7.1. (A) TEM image of 16 nm Fe_3O_4 NPs. Copyright 2002 American Chemical Society. (B–D) TEM images of (B) 7 ± 0.5 nm, (C) 8 ± 0.4 nm, and (D) 10 ± 0.8 nm Fe_3O_4 NPs. The scale bars are 20 nm. Copyright 2009 American Chemical Society. (E) TEM image of octahedral Fe_3O_4 NPs. Copyright 2009 Royal Society of Chemistry. (F) TEM image of Fe_3O_4 nanoprisms. Copyright 2010 Royal Society of Chemistry. TEM images of (G) 14 nm spherical and (H) 32 nm and (I) 53 nm truncated octahedral FeO NPs and (J) SEM image of truncated octahedral FeO NPs. Figure is a reprint from [21].

Expanding this concept, we can see that inducing several flips in magnetization by applying an alternating magnetic field (AMF) can generate heat loss. As a result, the thermotherapy of

magnetic hyperthermia treatment exploits the heat generation capabilities of iron oxide nanoparticles. Under an AMF these particles generate a local temperature increase significant enough to kill cancer cells [33, 34]. The application of iron oxide nanoparticles to facilitate cellular level local heating is possible because magnetically induced aggregation of the particles can increase heat generation power, and the surfaces of the nanoparticles can easily be modified with a biocompatible functionality.

1.8 Surface Modification and Targeting Ability. An attractive property of iron oxide nanoparticles is their high surface area to volume ratio, because it provides the opportunity for high loading with relevant ligands [24]. For NPs to be successful in thermotherapy they have to be internalised by their target with high efficiency. Cellular internalization means interacting with membrane-embedded receptors or the lipid-bilayer [35]. Therefore, NPs have to be functionalised with ligands that can bind with specificity and high affinity to receptors on its target. Recent work in China has shown that dopamine-modified cyclodextrin nanoparticles display superior intracellular internalisation [36]. Unfortunately, these catechol moieties also show a high affinity for iron oxide, binding irreversibly, and hence cannot be expressed on iron oxide NP surfaces. However, the affinity of catechol moieties, like nitrodopamine, to iron oxide provides the opportunity of converting these into anchors for facile functionalisation of iron oxide NP surfaces [37].

Nitrocatechols can be easily coupled to an acid-terminated polymer via an amidation reaction. This process allows for seemingly endless modification of iron oxide NP surfaces. Reimhult et al. used this method to modify iron oxide NPs with a temperature sensitive polymer that could allow for temperature induced aggregation of NPs (Fig. 1.8.1) [38].

Improving the efficacy of iron oxide NPs in nanomedicine has led to several developments. Among these are the encapsulating of pharmaceuticals in NP polymer brushes for intracellular delivery, and the incorporation of iron oxide NPs into lipid membrane vesicles for a NP triggered release of pharmaceuticals [39, 40]. The lipid membrane vesicles can allow for both hydrophobic and hydrophilic pharmaceuticals to be incorporated as the vesicles contain an aqueous interior and an amphiphilic membrane (Fig. 1.8.2). Both of these developments exploit the magnetic properties of iron oxide nanoparticles by using AMF induced heating to soften the polymer brushes releasing the encapsulated drug.

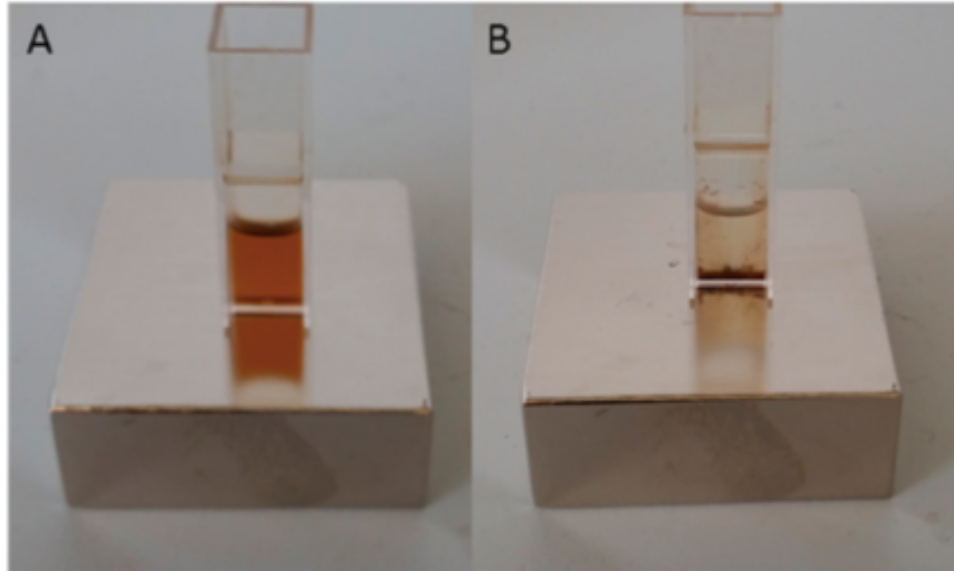


Figure 1.8.1. 10.7 nm/PNIPAM 20 kDa, 5 mg/mL in a poly(methyl methacrylate) (PMMA) cuvette placed upon a neodymium magnet, (A) at room temperature, (B) at 40 °C. In plastic cuvettes, a discoloration of the cuvette wall remains, interpreted as a high affinity of the dehydrated PNIPAM for the cuvette walls. Reprint from [38].

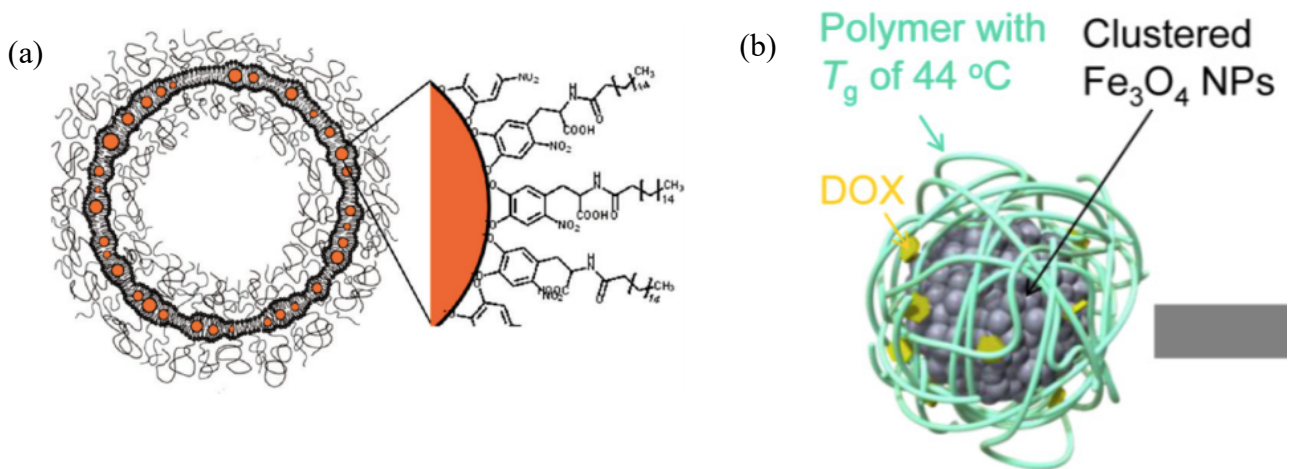


Figure 1.8.2. Schematic Representation of (a) liposomes containing iron oxide NPs in their bilayer (reprint from [41]) and (b) clustered iron oxide NPs encapsulating DOX in its polymer functionality (reprint from [39]).

1.9 Conclusion. The importance of iron in the micro and nano world is due its unique magnetic properties. Magnetic microparticles exhibit ferromagnetism that allows for the manipulation of the rheological properties of a fluid in response to a magnetic field. Their behaviour under an applied magnetic field forms networks of confined microenvironments as a result of a chain-like self-assembly. This response has found many uses in industry, especially in shock absorbers and dampers. In contrast, magnetic nanomaterials display superparamagnetism, a property that allows for magnetically induced heating. This property, along with their small size and relatively easy surface modification makes these materials excellent tools in nanomedicine.

Research Objectives. Our study contains two primary objectives:

1. To develop magnetorheological fluids as smart media for controlling crystallisations.

In order to achieve this goal, we have set out the following objectives:

- a.** Develop a range of MR fluids by modifying the surface of iron micro particles with stabilising ligands. The goal is that these ligands aid in deterring the sedimentation rate of the particles and provide a means of interacting with drug molecules.
- b.** Investigate the crystallisation of an active pharmaceutical ingredient (API) with emphasis on the effect of MR fluid on crystal morphology.
- c.** Determine if different solvent systems can be used in the development of MR crystallisation media.

2. To synthesise and modify iron oxide nanoparticle clusters with a temperature sensitive polymer, poly-N-isopropyl acrylamide (PNIPAM), for improving heating efficiencies in thermotherapy. To achieve this, we set the following objectives:

- a.** Synthesise and stabilise iron oxide nanoparticle clusters by reproducing the method published by Hayashi et al. [39].
- b.** Synthesise and characterise PNIPAM.
- c.** Modify iron oxide nanoparticle clusters with PNIPAM polymer.

Chapter 2

Magnetorheological Fluids for Controlling Pharmaceutical Crystal Growth

Chapter 2. Magnetorheological Fluids for Controlling Pharmaceutical Crystal Growth

2.1.1 Crystallisation and Polymorphism. Solution crystallisation is one of the most widely used methods for the manufacturing of active pharmaceutical ingredients (APIs) [43]. It is an attractive method because a single process combines both particle formation and purification. The complex process of crystallisation is very sensitive to environmental conditions and hence we often obtain more than one form of an API known as polymorphism. In an ideal case, we want to obtain a pharmaceutical with a specific size, crystal habit, crystal structure and low degree of imperfection. Considering that the spontaneous appearance of a new phase occurs in a system that is in non-equilibrium, the crystallisation process first begins with the formation of a supersaturated solution. Then, the dissolved molecules can begin to aggregate, leading to fluctuations in the bulk concentration, eventually forming nuclei. The nuclei begin to grow as particles diffuse to the surface of existing nuclei (Fig. 2.1.1) [44].

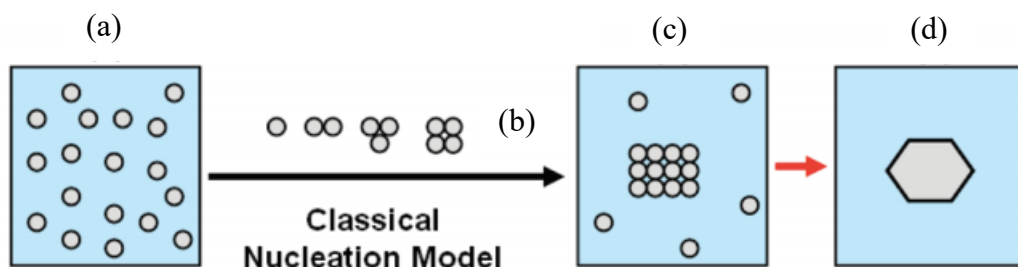


Figure 2.1.1. Schematic Representation of the pathway leading from solution to solid showing (a) supersaturated solution, (b) ordered subcritical cluster of solute molecules, (c) ordered crystalline nuclei, and (d) solid crystal. Image and caption are a reprint from [44].

Polymorphism describes the variation in solid form that an active pharmaceutical ingredient (API) can take. This plays an important role in defining the stability and drug release properties of an API because crystalline variations such as polymorphism are responsible for differences in bio-inequivalence and chemical and physical stability [45]. In fact, these variations have increased interest in polymorphism, crystallisation and process development in the pharmaceutical industry [46].

Ostwald's step rule states that in general, the least stable (less soluble) polymorph crystallises first. This is because the state which is sought out is the nearest in stability to the original, instead of the more thermodynamically stable one [47]. Although this rule is not a universal law, it is a possible preferred tendency. This behaviour is the source of much trouble in industry as the more thermodynamically stable polymorphs tend to form during storage of a pharmaceutical, i.e. on the shelves [48]. In the summer of 1998 the protease inhibitor ritonavir was removed from the market because the storage of the API led to the formation of a much less soluble crystal form II, which greatly reduced oral bioavailability (Fig. 2.1.2) [49]. Similarly, in 2008 the dopamine agonist rotigotine (Neupro) was recalled because of the appearance of a new, less soluble polymorph [50]. Hence the topic of controlling the polymorphism of pharmaceutical ingredients has attracted increasing attention.

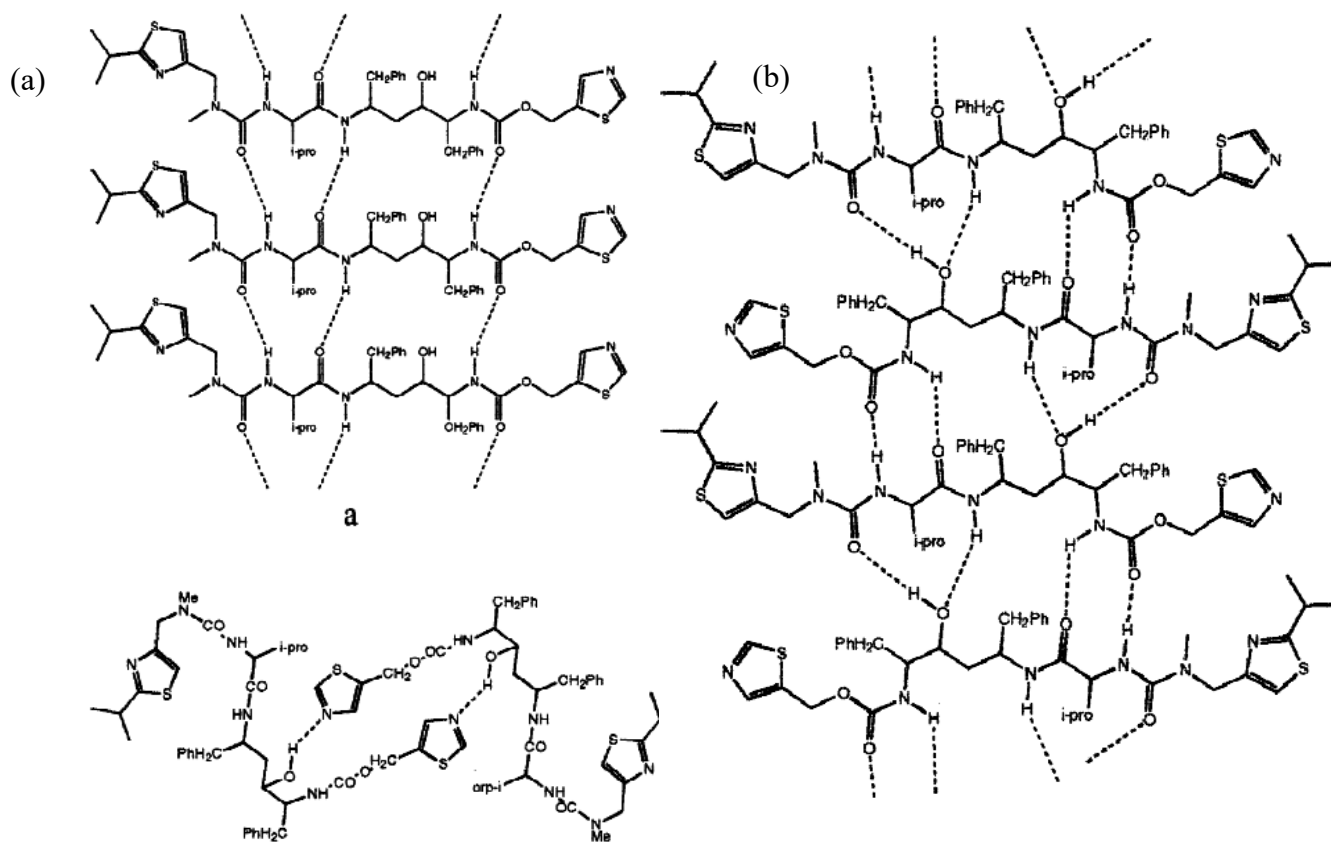


Figure 2.1.2. Hydrogen bonding network for Ritonavir (a) form I and (b) form II. Reprint from [49].

In an effort to address the shortfalls of solution crystallisation in controlling polymorphism, pharmaceutical industries are moving towards the addition of guest molecules such as salt-formers, co-formers and solvates. These work by pairing a drug with a counterion to create a salt version of the drug, a process that creates new chemical entities and widens the selection basis without altering the drug [51, 52]. However, these methods would require extensive testing in order to determine a suitable guest molecule, making these methods expensive and time consuming [53]. It is known that the physical characteristics of a crystal can be improved in a crystallisation media that promotes the suppression of convection currents, sedimentation and nucleation rates. A medium like this can be realised in a viscous gel environment. The technique of growing crystals in gels was first reported in the work of Raphael Eduard Leisegang who, in 1896, observed patterns arising from the periodic precipitation of a weakly soluble salt in a hydrogel [54].

2.1.2 Crystal Engineering in Confined Spaces. For a long time, a very wide range of materials had been recognised to form gels. It wasn't until the late 1990's however, that ureas, amides, porphyrin derivatives and many others, were discovered to form fibrous gels. The assembly of these low molecular weight compounds (known as low molecular weight gelators, LMWG), into fibrous gel networks offers the potential to tune gelators to specific conditions [55], i.e. solvent systems or crystal substrates. LMWGs can be synthesised to match the chemistry of an API, and hence provide an active nucleation surface [56].

In 2010, Steed et al. crystallised a range of drug substances in organic LMWGs, referred to as organogels [57]. The procedure involved the warming of the gelator and drug in a compatible solvent system and allowing the mixture to cool. The crystallisation of carbamazepine (CBZ) in these organogels produced significantly larger crystals, up to 30 times larger in toluene gels, however, the crystal habits observed in these gels were the same as those in their corresponding reference (i.e no gel). Adjusting the ratios of co-solvent to toluene and varying the CBZ concentrations resulted in a preference for one form over another. More importantly, the lack of gelator-drug co-crystal formations indicated a phase separation between gel and crystals. It is possible that the microenvironment afforded by these LMWGs was small enough to restrict the mobility of solute molecules, but not to force interactions between solute molecules and the gel network chemical structure.

A study performed on crystallisations of CBZ in polymer microgels suggests that the crystallisation process in gels is aided by confined environments formed from the fibrous networks of gels [58]. These create microenvironments that facilitate solute-solute interactions and in some cases, the walls of these microenvironments (gel fibre network) can interact with solute molecules to act as nucleation “catalysts”, lowering the nucleation barrier of a polymorph. Furthermore, the results of this study suggest that polymorph selectivity can be obtained from nucleation arising from specific polymer-solute interactions which are facilitated by an optimum spatial configuration (Fig. 2.1.3). In this case the confinement effect created by the gel network provides the spatial configuration necessary to facilitate polymer-solute interactions.

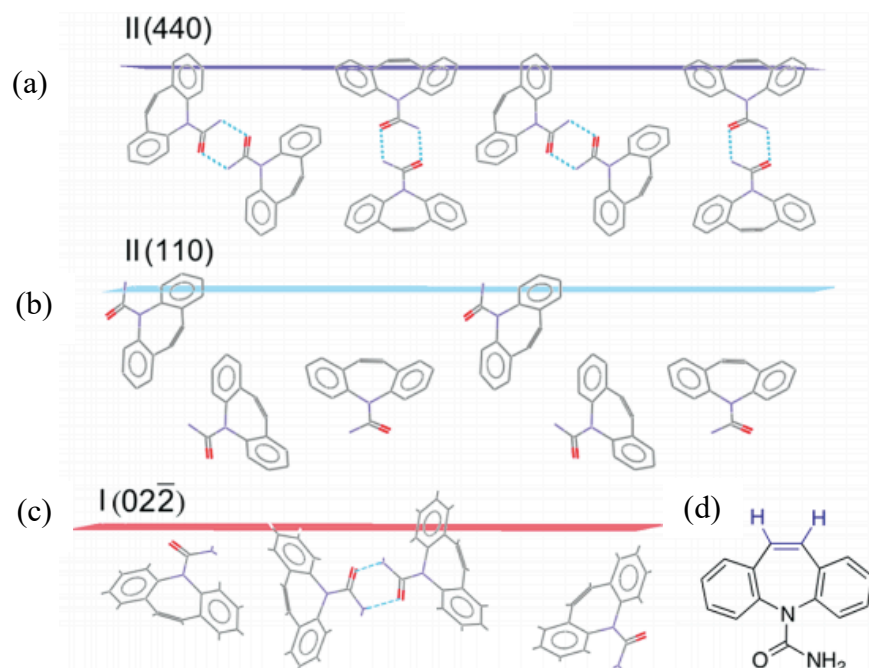


Figure 2.1.3. (a) and (b) are surface structures of form II facets preferentially nucleated on polymer surfaces. (c) Surface structure of a facet characteristic of form I not grown from polymer surface. (d) Functionality in CBZ inferred to interact preferentially with PEGDA polymer (coloured blue). Image and caption are a reprint from [58].

2.1.3 Magnetorheological Fluids. The knowledge that confinement effects can facilitate polymer-solute interactions allows for the possibility of designing nucleation substrates. This led us to consider magnetorheological fluids as a means of controlling crystal polymorphism.

Magnetorheological (MR) fluids are suspensions of magnetisable iron micro particles dispersed in a carrier fluid that exhibit the property of changing their rheology under a magnetic field [59]. Their relatively large size (up to 10 μm) means that they are magnetically multi-domain particles and hence do not possess a permanent magnetic dipole moment. Therefore, these suspensions exhibit a field-dependent change in rheology, displayed by an increase in viscosity and display of yield stress. Phulé and Ginder reported a yield stress of 100 kPa at a 10,000 G field for 40 vol. % iron-based MR fluids [60]. In contrast, in the absence of a magnetic field, i.e. the “off” state, the MR fluids exhibit viscosities similar to that of the carrier fluids.

The properties of these materials have attracted considerable attention in mechanical engineering as active devices that can be used to reduce mechanical vibrations. MR fluids are employed in active suspension, like that found in vehicles, and other dampers. The MR fluids act by performing real-time adjustments in the viscosity of a carrier fluid, in most cases oil, in order to affect the pressure exerted on a piston. The piston itself is an electromagnet with small channels that allow fluid to pass through (Fig. 2.1.4). This piston is immersed in an MR fluid, and as force from the vehicle is exerted on to the piston, a computer adjusts the magnetic field necessary to affect the rheology of the fluid and hence control the motion of the piston [61].

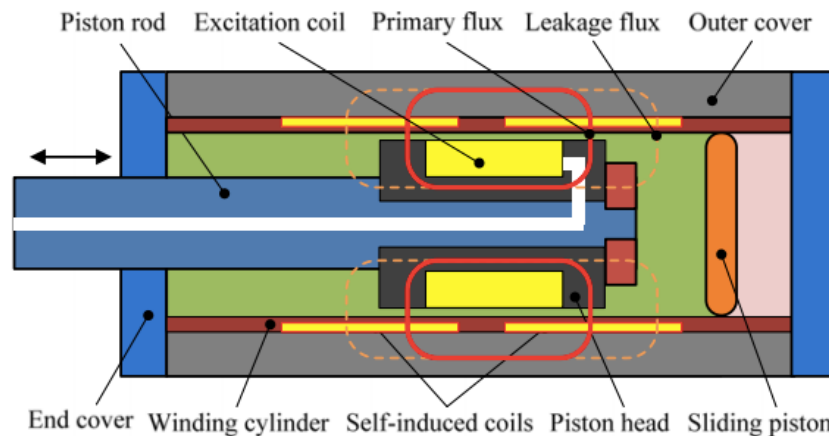


Figure 2.1.4. Schematic Representation of a magnetorheological damper. Reprint from [62]

Unfortunately, a major drawback of MR fluids is their tendency towards sedimentation in the absence of a magnetic field. Their high density and large size means that keeping the particles evenly dispersed is a challenge and hence much of the research into these fluids has been towards affecting their density [63].

MR fluids affect viscosity by creating confined environments from the self-assembly of particles into chains along the direction of magnetic flux. The application of a magnetic field induces a magnetic dipole in each particle, causing them to assemble into chains, thereby preventing the flow of fluid (Fig. 2.1.5) [64]. These assemblies can be considered more ordered versions of a fibrous gel network, whereby the size of the confined environment is dependent on the magnetic field.

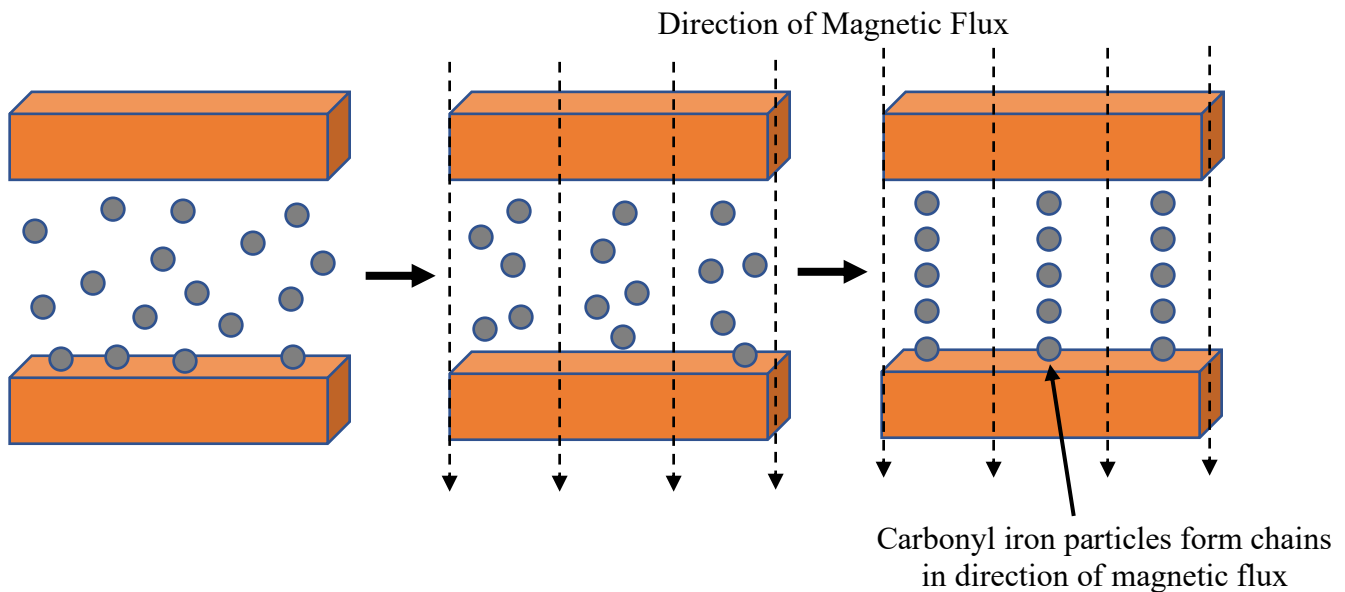


Figure 2.1.5. Schematic Representation demonstrating the MR effect in response to a magnetic field.

Furthermore, as a result of efforts to reduce the sedimentation of MR fluids, it has been shown that the surface of these iron micro particles can be modified with a variety of functionalities [65]. The ability to modify the surface of these particles opens up the possibility of designing interactions between particles and solute (drug) molecules.

2.2 Adapting Magnetorheological Fluids for Crystallisations. Favourable active pharmaceutical ingredient (API) properties are defined by chemical purity and physical properties such as crystal habit and size, crystal structure and degree of crystal imperfection [43]. The physical characteristics of a crystal can be improved by creating a crystallisation media that promotes the suppression of convection currents, sedimentation and nucleation rates. A tuneable crystallisation medium would not only improve the physical characteristics of a crystal but also provide some control over polymorphism, enantiomorphism and other crystal habits [57]. Such a medium can be realised in low-molecular-weight supramolecular gels (LMWGs), whose inert matrix can support crystal growth. However, LMWGs have the disadvantage of incorporating into the crystal matrix and recovery of the crystals requires several washing steps that can damage or dissolve the crystals in the process. Alternatively, magnetorheological (MR) fluids can provide the confinement necessary to facilitate crystal growth, with the added advantage of an easy separation of crystal and iron particles, as the particles can be magnetically separated.

The potential of MR fluids as a medium for crystal growth remains unexplored. Herein we propose the use of MR fluids as reversible “gelators” for the control of crystal growth in active pharmaceutical ingredients (APIs). We propose tuning the interactions between the MR fluid and the growing crystal by introducing a diverse array of functionalities onto the iron micro particle surface.

2.3 Properties of Carbonyl Iron (CI) Particles. The form of iron particles employed in this study is commonly referred to as carbonyl iron. Carbonyl iron (CI) is a highly pure iron prepared by the chemical decomposition of iron pentacarbonyl. The process is based on the fact that at a temperature of 300 °C iron pentacarbonyl vapours decompose according to the reaction in Fig. 2.3.1. This process produces a powder containing a range of particle sizes. The manufacturing process ends with a milling and size classification step that results in a narrow size distribution. CI is manufactured and distributed by BASF and Sigma Aldrich and can be obtained in sizes ranging from 1 to 6 μm . In this study we use CI obtained from Sigma Aldrich with a reported particle size of 1 – 3 μm and a bulk density of 7.86 g/cm^3 . SEM analysis revealed CI particles to be spherically uniform and of an average size distribution of 1

– 3 μm , with the odd appearance of particles smaller than 1 μm , likely due to the milling and separation process employed by Sigma Aldrich (Fig. 2.3.2).

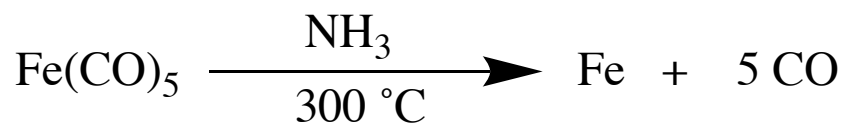


Figure 2.3.1. Reaction scheme for the decomposition of iron pentacarbonyl.

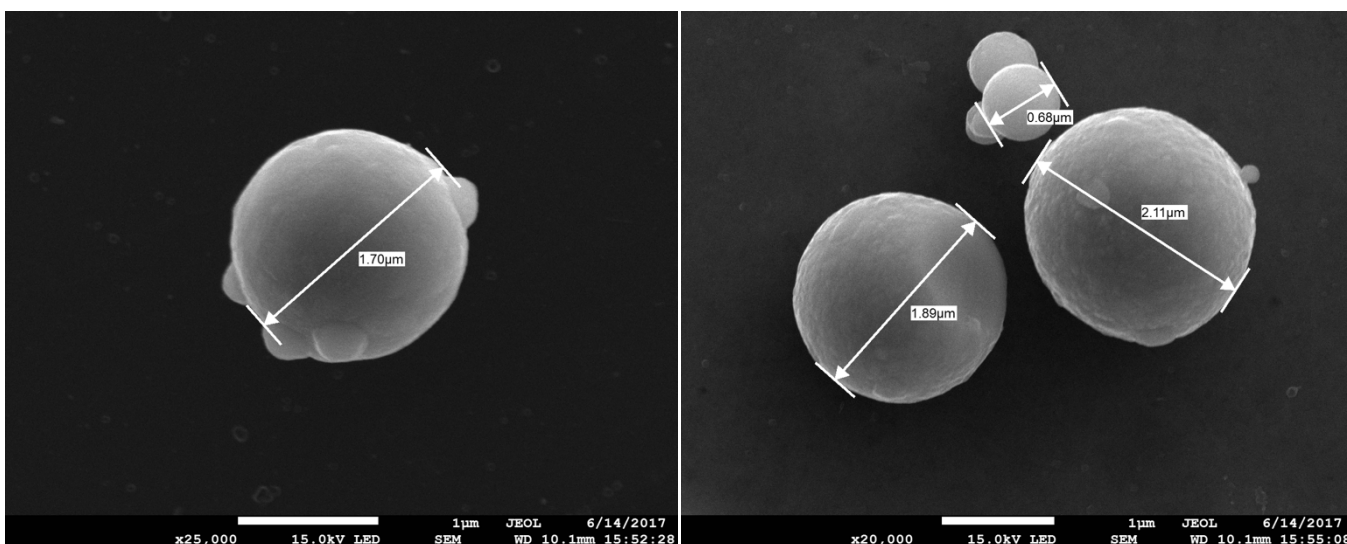


Figure 2.3.2. SEM images of bare carbonyl iron particles.

The magnetism of the particles was confirmed when during the preparation of an MR fluid a nearby neodymium magnet was attracted to the fluid and broke the container. The degree of magnetization in response to a magnetic field is known as magnetic susceptibility and is represented as a dimensionless proportionality constant. The extreme magnetic behaviour of our sample of CI made it clear that magnetic susceptibility measurements could prove difficult, since the measurement relies on the response of very sensitive magnets. Inserting a ferromagnetic substance like CI into a magnetic susceptibility scale could permanently damage it. It may be possible to dilute a sample in an inert gel media to collect a

measurement; however, this measurement may not be reliable as an absolute value for the material. The magnetic susceptibility of CI of this size has been reported in the literature as 1.63 – 3.00 SI [66].

An MR fluid is made up of two main components, the carrier fluid and the magnetic iron particles, in this case CI. The behaviour of MR fluids in the absence of a magnetic field is similar to that of the carrier fluid, except that the presence of CI makes the fluid a bit more viscous. It is the fluid's increase in viscosity and display of yield stress under a magnetic field which is characterised as the magnetorheological effect. In this work, MR fluids were prepared from CI iron (bare or modified) particles in 40 wt. % concentrations in a toluene or water carrier fluid. Initial experiments utilised silicone oil as the carrier fluid, however, for crystallising drug molecules this was changed to toluene. The samples were prepared in small vials, shaken to disperse the particles evenly, and then placed in between the poles of an electromagnet from a Bruker EMX EPR instrument (Fig. 2.3.3).

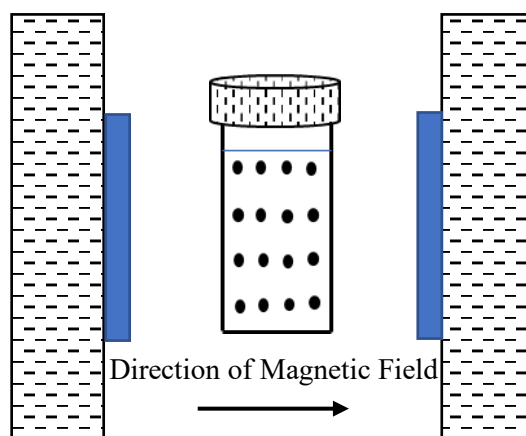


Figure 2.3.3. Schematic Representation of MRF setup

This instrument provides a homogeneous field throughout the sample area, unlike a small permanent magnet where the magnetic field varies with distance from the source. In toluene, a 100 G field produced increases in viscosity which were significant enough to demonstrate a decrease in fluid flow, but not significant enough to immobilise the fluid, which we observed by simply inverting the container. To obtain fluid immobility in toluene a magnetic field strength of 200 G is required. The absence of a magnetic field results in the

sedimentation of the particles in a matter of seconds (Fig. 2.3.4a and d) and a 1000 G field results in a very strong magnetorheological effect that maintains the CI particles evenly dispersed in the carrier fluid (Fig. 2.3.4b). Inversion of the container at 1000 G shows the immobility of the carrier fluid, but also reveals a layered structure (Fig. 2.3.4c). This layered structure was only revealed at 1000 G because the container was inverted while in the field, however, we observed behaviours like the one in Fig. 2.3.4c at field strengths above 1000 G, where the layers became more defined at higher field strengths. We observed that as the field strength was increased, the layers became visible and more uniform in size, while at lower field strengths the layers were of random sizes. Unfortunately, we did not measure the gap sizes, nor did we investigate the phenomenon further.

Although not visible at or below 1000 G, these layers represent the mechanism by which fluid immobility is attained. The self-assembly of CI particles into chains induced by a magnetic field (Fig. 2.1.5) create pockets which trap the carrier fluid. Removing the container from the magnetic field demonstrates that the CI particles sediment in the absence of a field, and the carrier fluid returns to its original viscosity (Fig. 2.3.4d).

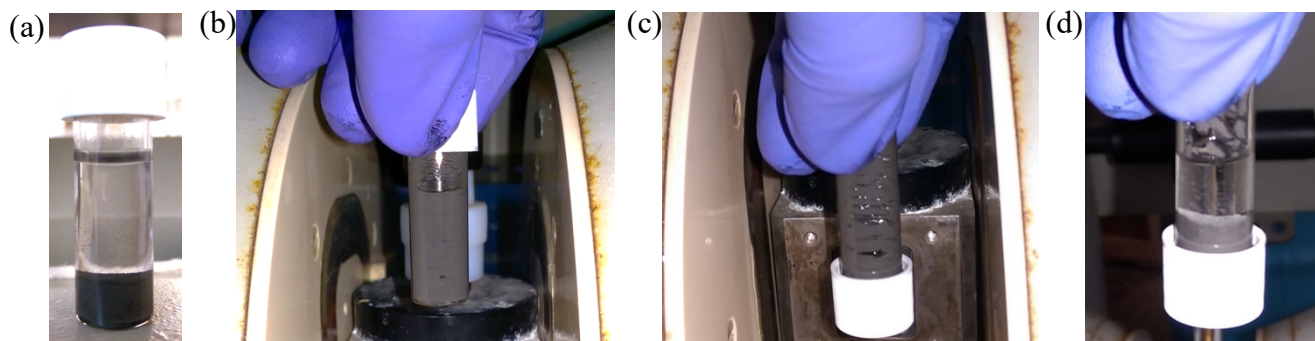


Figure 2.3.4. Images displaying MR fluid in (a) 0 G field, (b) 1000 G field, (c) upside-down in 1000 G field and (d) upside-down in 0 G field.

2.4 Surface Modification of Carbonyl Iron. Sedimentation of CI in an MR fluid is mainly due to the large density and size of the micro particles. A lower sedimentation rate would facilitate the handling of these fluids in the absence of a field. To improve the particles' colloidal stability a high molecular weight polymer can be adsorbed to the particle surface to

decrease the particle's overall density and increase interactions with the solvent molecules. We chose a PEG functionality because of its relatively simple synthesis and high-water solubility. Owing to the reports of facile surface modification of iron oxide nanoparticles with nitrodopamine anchors, we decided to attach nitrodopamine to our PEG functionality, because our CI particles most likely have oxidised surfaces.

First, acid terminated poly(ethylene glycol) methyl ether 5000 (mPEG) was prepared by modification of the hydroxyl end group of mPEG with succinic anhydride to generate the carboxyl end group (Fig. 2.4.1). Subsequently, the nitrodopamine molecule was coupled to the carboxylated mPEG through a conventional uronium reaction with COMU to generate mPEG-NDA (Fig. 2.4.1) [67,68]. The characteristic peaks of mPEG, carboxylated mPEG and mPEG-NDA were observed by FTIR and NMR at each step of the synthesis (Fig. 2.4.2).

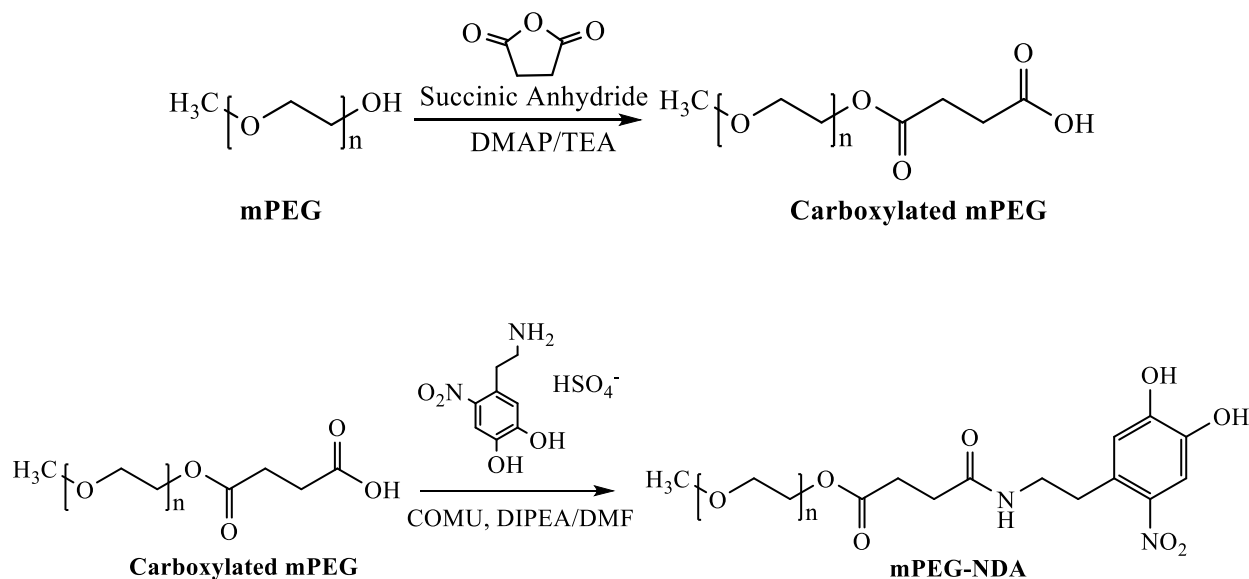


Figure 2.4.1. Synthetic scheme for Nitrodopamine PEG

In Fig. 2.4.2, the bands attributed to the C-O bond in ether are highlighted by a green box; the blue box indicates the presence of C=O of carboxylic acid and the orange box shows both the C=O bond in carboxylic acid (1734 cm^{-1}) and the C=O bond of the amide (1645 cm^{-1}) from

the addition of nitrodopamine. The presence of both bands at 1645 and 1734 cm^{-1} in mPEG-NDA indicated that not all the carboxylated mPEG was coupled to nitrodopamine. UV-Visible spectroscopy analysis was performed by creating a dilution series of nitrodopamine in PBS. Concentrations ranging from 18.75 μM to 150 μM were prepared and the peak absorbances at 425 nm were used to plot a calibration curve. We then prepared a 300 μM sample of mPEG-NDA in PBS and measured the absorbance at 425 nm. Using the formula obtained from the calibration we determined that only 20% of the carboxylated mPEG had been successfully converted to mPEG-NDA (Fig. 2.4.3).

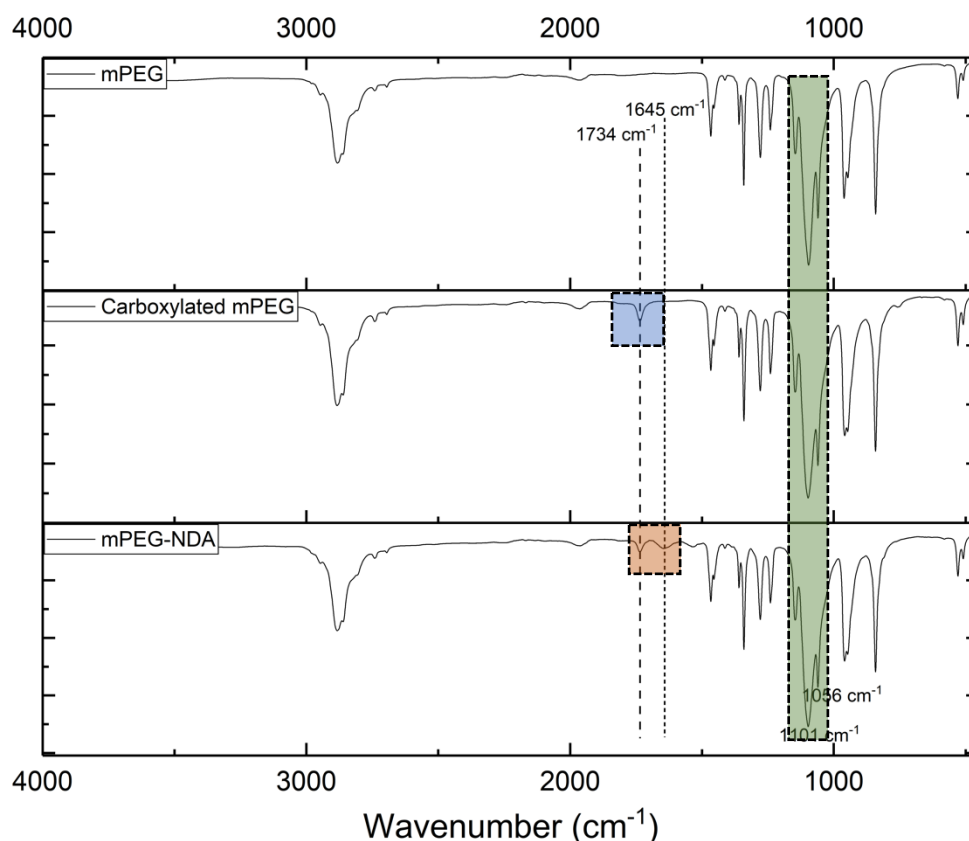


Figure 2.4.2. FTIR spectra mPEG, Carboxylated mPEG and mPEG-NDA

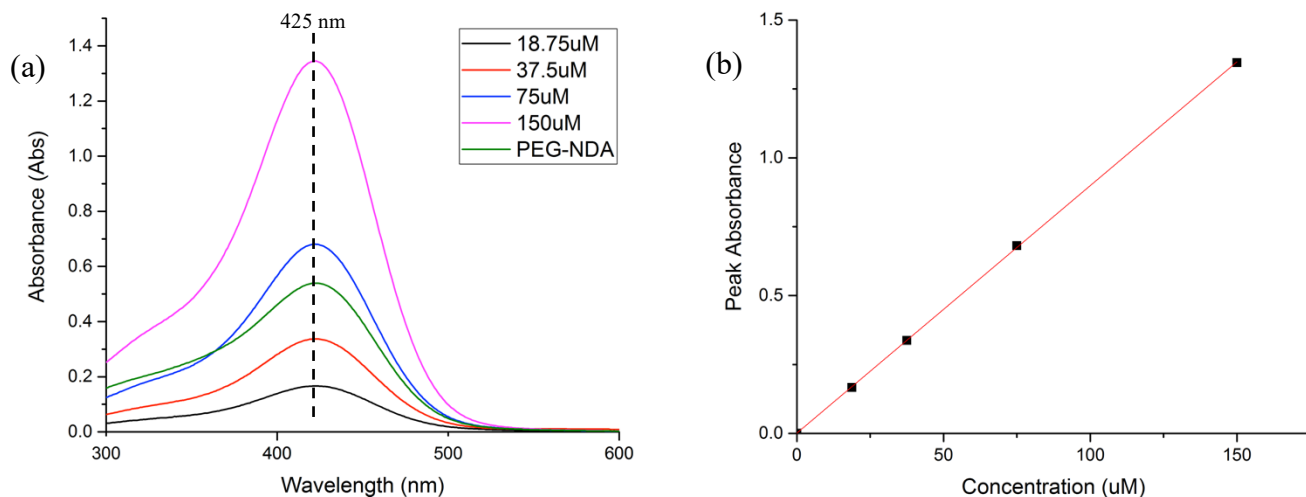
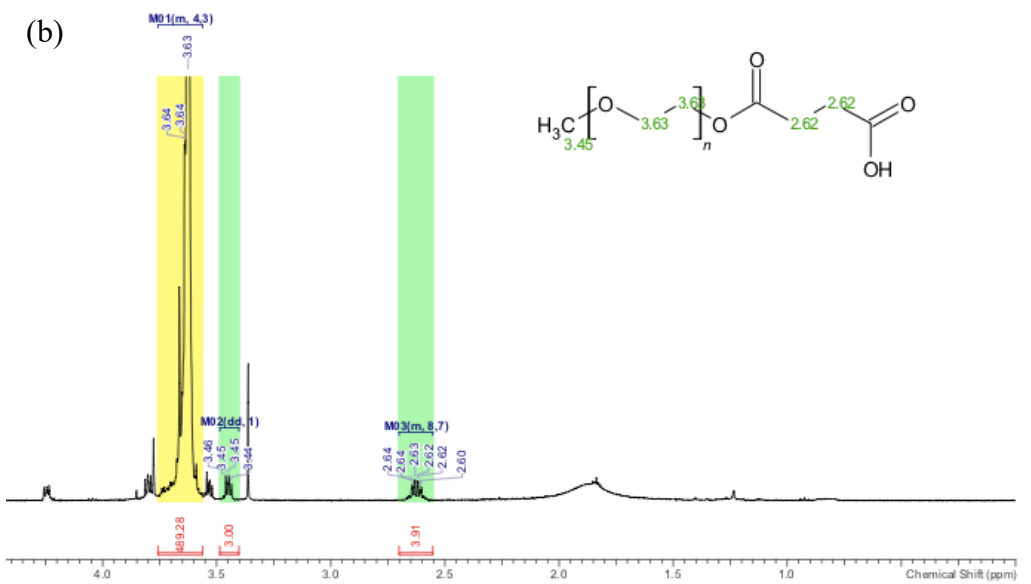
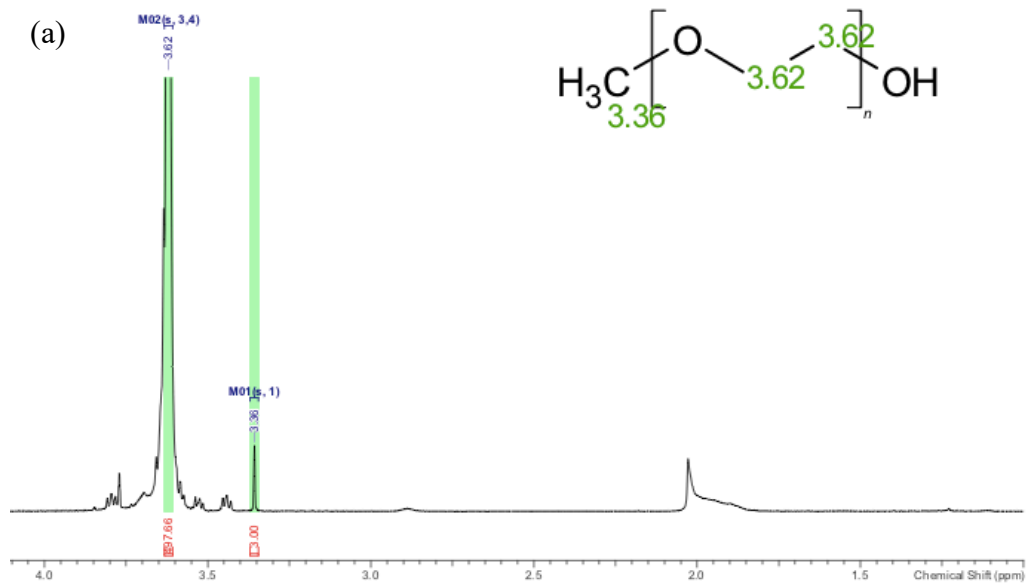


Figure 2.4.3. (a) UV-Visible absorption spectra of functionalised mPEG-NDA and (b) calibration curve obtained from UV-Visible spectra of nitrodopamine (NDA).

This result may explain the absence of nitrodopamine peaks in ^1H NMR Spectra. To remedy this low conversion, the experiment was repeated with an excess of coupling agent, COMU. Modification of the synthesis resulted in a 53% conversion of carboxylated mPEG to mPEG-NDA. The chemical structures and compositions of the synthesised polymers were determined by ^1H NMR spectroscopy (Fig. 2.4.4). The resonances at 3.36 and 3.62 ppm were attributed to $\text{CH}_3\text{-O}$ and $\text{-O-CH}_2\text{-CH}_2\text{-O}$ protons respectively in the mPEG unit.

The resonances of the $\text{-CH}_2\text{-CH}_2\text{-}$ protons from the addition of succinic anhydride appeared at 2.62 ppm (Fig. 2.4.4b), and the appearance of two singlet peaks at 6.77 and 7.66 ppm (Fig. 2.4.4c) associated with the two protons in the aromatic ring of the nitrodopamine molecule confirm the conversion to mPEG-NDA.

Additional confirmation of the formation of carboxylated mPEG and mPEG-NDA was provided by performing mass spectrometry at each step of the synthesis (Fig. 2.4.5). As can be seen from the zoomed-in regions in Fig. 2.4.5, mass peaks of a series are separated by the monomer weight of PEG, 44 Da.



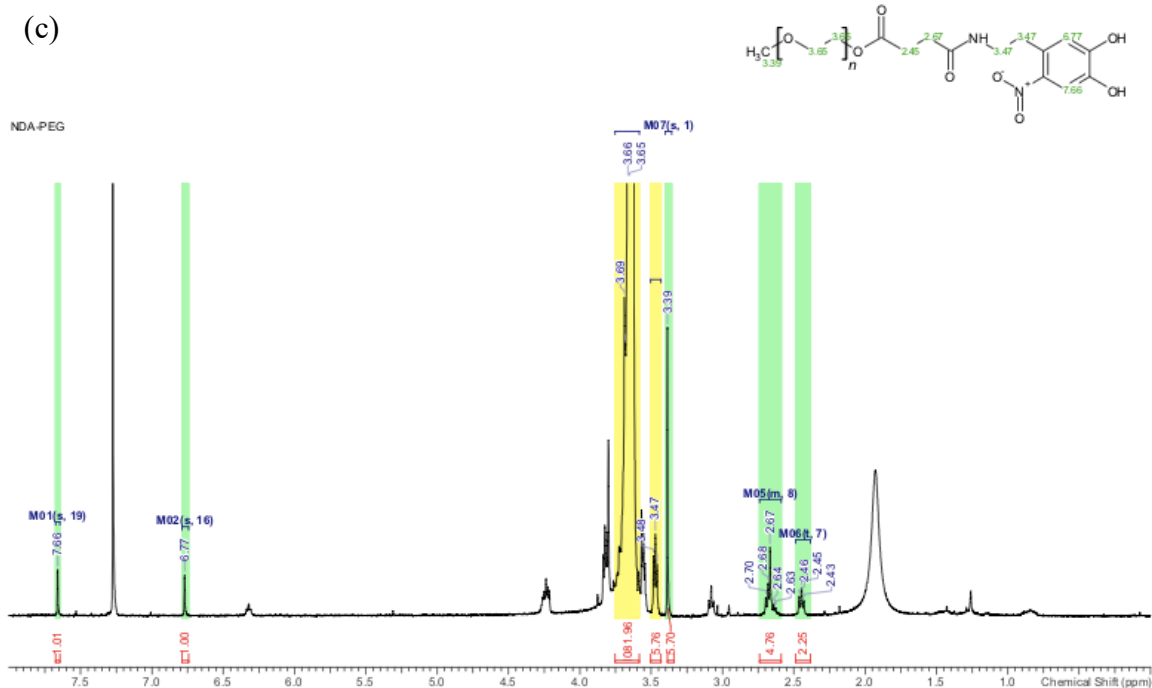


Figure 2.4.4. ^1H NMR Spectra of (a) mPEG, (b) carboxylated mPEG and (c) mPEG-NDA in CDCl_3 .

It is possible to take a peak from the MALDI fingerprint for mPEG, add the mass corresponding to the addition of succinic anhydride (100 Da), and subtract the monomer weight of PEG (44 Da) until you arrive at a peak observed in the fingerprint for carboxylated mPEG. For example, if we take the peak at 5430 in the spectrum for mPEG and add 100 (corresponding to the addition of succinic anhydride) we get 5530, which is a peak observed in the spectrum for carboxylated mPEG (Fig. 2.4.5). Subtracting 44 (monomer weight of PEG) we get 5486, which is also observed in the fingerprint of carboxylated mPEG. This confirms that the fingerprint obtained is a result of the addition of succinic anhydride. The same can be done with mPEG-NDA, except that we add the mass corresponding to the addition of nitrodopamine (166 Da). Using this method, we were able to confirm the conversion of mPEG to carboxylated mPEG and mPEG-NDA. The peaks in each fingerprint line up with the peak positions expected for each step of the synthesis.

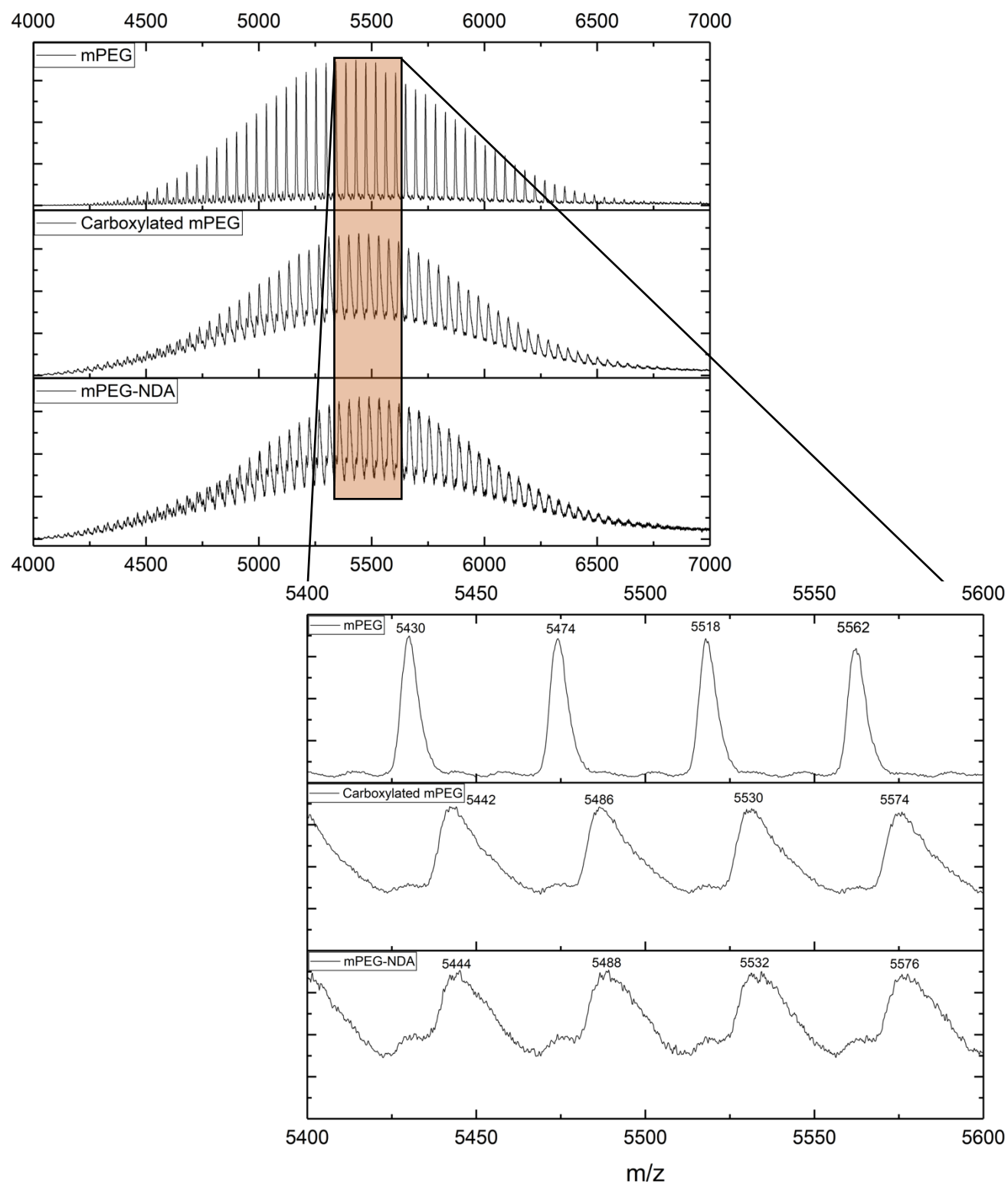


Figure 2.4.5. MALDI-TOF mass spectra of mPEG, carboxylated mPEG and mPEG-NDA.

However, the broad line-shape and lack of resolution observed at each conversion step indicates that some starting material remains at the end of the reaction.

2.5 Surface Modification of Carbonyl Iron with mPEG-NDA. To graft polymer chains onto CI particles, mPEG-NDA (20 mg) was sonicated with bare CI particles (1 g) in 20 mL of pH 7 phosphate buffer solution (PBS) for 8 h. Grafting densities for mPEG-NDA on iron oxide nanoparticles have been reported at $(0.5 - 2) \times 10^6$ chains/ μm^2 [68]. Using the higher estimate of 2×10^6 chains/ μm^2 , we calculated the mass of chains on a CI particle with a diameter of 2 μm and then calculated the ratio of particle mass to mass of chains [Appendix]. By this method, it was calculated that the mass of polymer required was approximately 0.70% of the mass of CI used. A 7 mg excess of polymer (i.e. 14 mg) was used to facilitate functionalisation.

To determine if functionalisation was successful, 1 mL aliquots of the reacting solution were taken every hour and examined using UV-Visible absorption spectroscopy. Fig. 2.5.1a shows the results of this experiment at 0, 2 and 3 h. It is clear from the graph that the absorption band of nitrodopamine at 425 nm is replaced by a continuum that precludes positive assignment. The solution was centrifuged to remove the iron particles prior to analysing the mother liquor, therefore the absorption continuum is likely due to a leachate. It was also clear that the signal for nitrodopamine disappeared before the 2 h mark and that the pH of the solution had increased from 7 to 9.

To improve functionalisation, nitrodopamine anchors were complexed with carbonyl iron in dimethylformamide (DMF) because iron particles have greater colloidal stability in this solvent compared to PBS – due mainly to the fact that PBS causes aggregation of iron particles due to the strong interaction of phosphates with iron ions. Also, the greater viscosity of DMF results in improved colloidal stability [69, 70]. It should be noted that the absorption band corresponding to nitrodopamine shifts from 425 nm in PBS to 445 nm in DMF.

The grafting of polymer chains onto CI particles was attempted in DMF by sonicating mPEG-NDA (20 mg) with bare CI particles (1 g) in 20 mL of DMF. Functionalising a sample of bare-CI with mPEG-NDA in DMF showed a decrease in the intensity of the absorption band at 445 nm (Fig. 2.5.1b), indicating a depletion of nitrodopamine after 20 min, which suggests that functionalisation was beginning to take place on bare-CI particles. However, the previously observed absorption continuum increased after 40 and 60 min, indicating that

leaching from the particle surface was still taking place. This eventually led to the obstruction of the signal at 445 nm. Using Beer's law, we calculated the mass of mPEG-NDA grafted onto CI in the first 20 min [Appendix]. The decrease in absorbance at 445 nm from 0 to 20 min was consistent with a 0.51 mg depletion of mPEG-NDA (Fig. 2.5.1b). This result would indicate a 7.3% functionalisation efficiency; however, this cannot be taken as the absolute efficiency as particle leachate obstructed further analysis of the peak at 445 nm. The resultant particles from the functionalisation in DMF were filtered and dried and made into an MR fluid. MR fluids were prepared by mechanically stirring 1 g of CI with 1.56 mL of silicone oil. A mPEG-NDA MR fluid was prepared and compared against a bare CI control, however, both exhibited similar sedimentation rates, which we observed by visually monitoring the samples over a 1 h period. Thermogravimetric analysis of this sample also failed to confirm the presence of polymer as the expected 0.70% change in weight was virtually undetectable by this method.

We observed no marked decrease in the sedimentation rate when comparing the mPEG-NDA MR fluid with our bare CI control, which suggested that the particles were too large to be affected by the polymers. Nevertheless, the labour-intensive nature of functionalisation with nitrodopamine anchors led us to explore other methods for surface modification of CI.

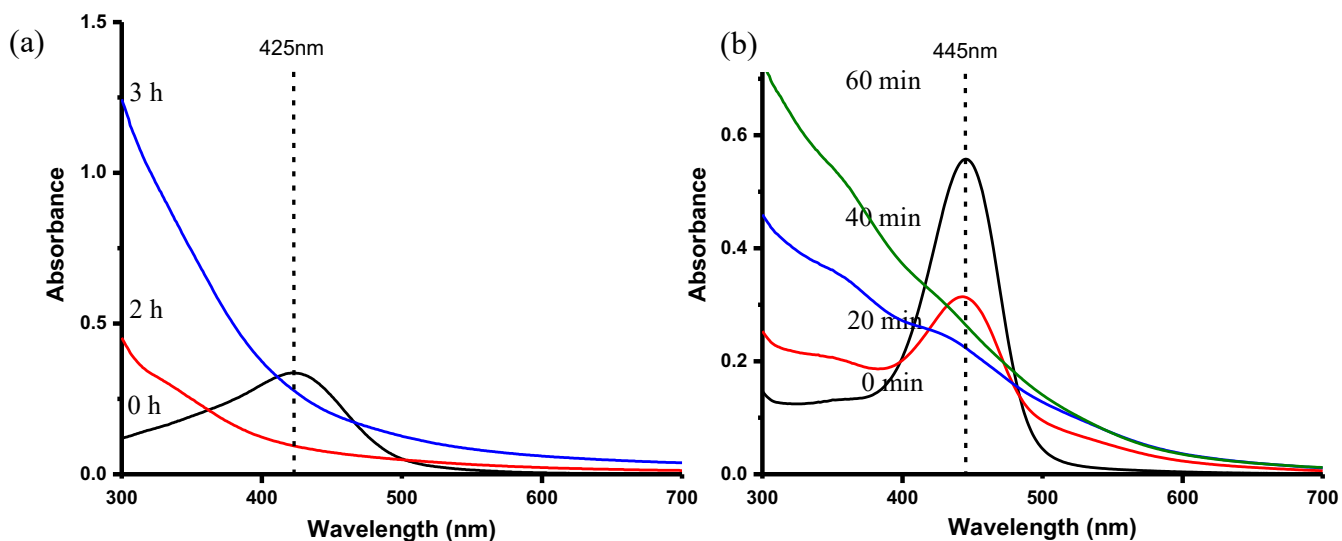


Figure 2.5.1. UV-Visible absorption spectra during functionalisation with mPEG-NDA of (a) bare CI in PBS, (b) bare CI in DMF.

Successful functionalisation of carbonyl iron (CI) particles with oleic acid has been demonstrated before [71,72]. Modifying CI particles with oleic acid was done by sonication of CI (1 g) and oleic acid (large excess, 3 mL) in 20 mL ethanol at 40 °C for 3 h. The hydrophobic behaviour of the resultant powder (Fig. 2.5.2) suggested that carboxylic acid moieties could provide a more facile means of modifying CI surfaces. Furthermore, changes in hydrophobicity could serve as an indicator of functionalisation. We probed the hydrophobicity of CI samples by taking a 200 mg sample, compressing it with a glass microscope slide, and then placing a 1 mL drop of water on the surface. Although only qualitative, this measurement provides evidence of changes to the surface properties of functionalised CI when compared to bare-CI. Considering the powder-like nature of CI it was not possible to reproducibly obtain contact angle measurements, and hence we were forced to rely on this qualitative analysis of hydrophobicity as an indicator of functionalisation.

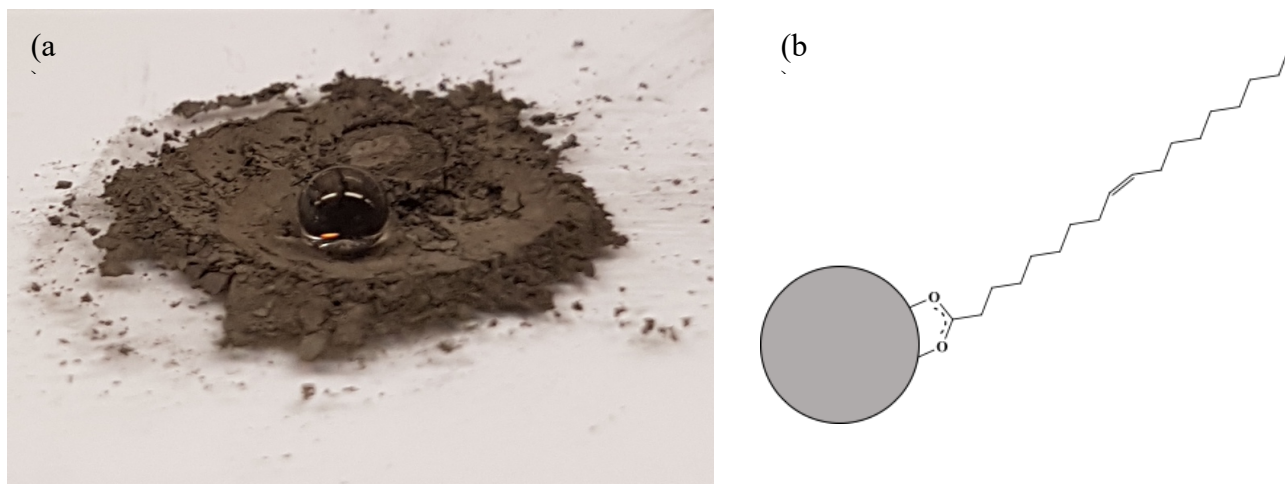
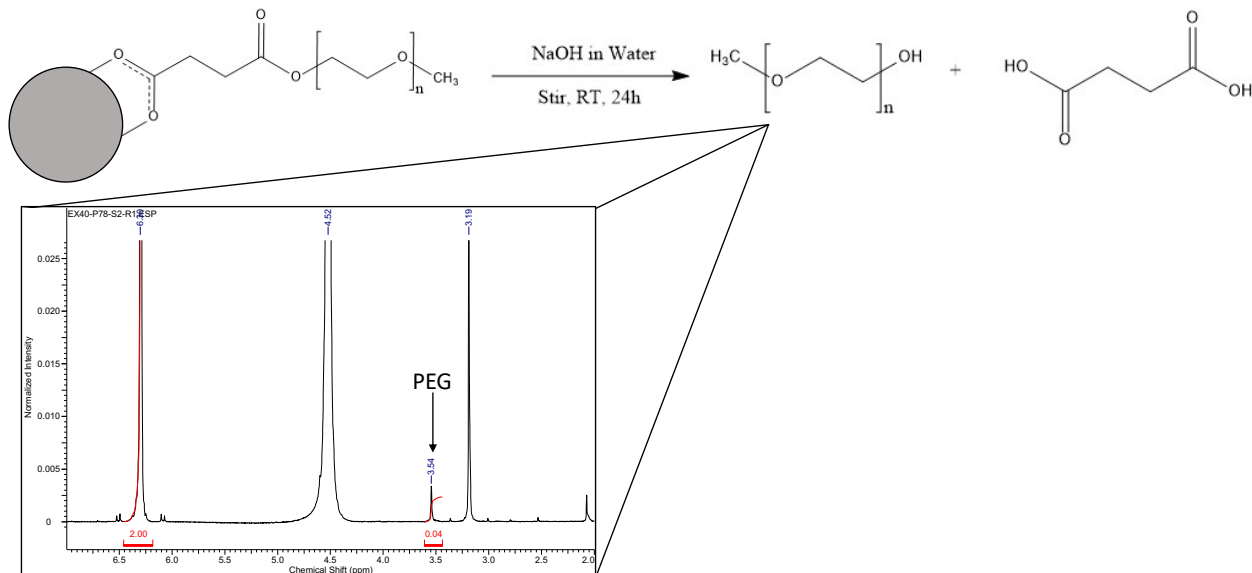


Figure 2.5.2. (a) optical image of water droplet on powder of oleic acid functionalised CI and (b) a graphical representation of functionality attached to the particle surface.

2.6 Surface Modification with Carboxylic Acid Moieties. The fundamental procedure for the functionalisation of CI with carboxylic acid moieties was adapted from the technique used by Huang et al. [71]. In our adapted procedure, CI (5 g) and the carboxylic acid-terminated moiety (1 g) were sonicated in ethanol at 40 °C for 3 h under a nitrogen atmosphere. The solution was then centrifuged and washed several times with the appropriate

To determine the amount of ligand adsorbed on to the CI surface, hydrolysis of the ligand in carboxylated mPEG functionalised CI (mPEG-CI) was performed in a 2 M solution of sodium hydroxide. This was done by stirring a 4 g sample in a 50 mL alcoholic solution of sodium hydroxide (2.0 M, methanol/water 9/1) for 24 h at RT. By hydrolysing the ester bond in the PEG ligand, we were able to release free PEG from the particle surface into solution that could be simply quantified using ^1H NMR spectroscopy as shown in Fig. 2.6.2. The results of this analysis are detailed in Table 2.6.1, where 4 g of PEG-CI was hydrolysed to release 0.54 ± 0.06 mg of PEG. From this result it was calculated that the grafting density for carboxylated mPEG onto CI micro particles was 3.9×10^4 chains/ μm^2 .



Particle Sizes (μm)	Functionality	Mass Calc. by qNMR (mg)	Grafting Density ^(a) (Chains/ μm^2)
1-3	Carboxylated mPEG	0.54 ± 0.06	3.9×10^4

Figure 2.6.2. Schematic Representation for the quantification of PEG adsorbed onto CI

Table 2.6.1. Quantitative NMR Spectroscopy results from the hydrolysis of PEG-CI

^(a)For the calculation of grafting density it was assumed that the average particle size was $2 \mu\text{m}$ and that the molecular weight of carboxylated mPEG was 5486 g/mol from (Fig. 2.4.5).

Carminic acid and 1-naphthaleneacetic acid were chosen because of their drastically different polarities and the presence of a carboxylic acid terminus, which make them capable of forming coordination bonds with CI [73]. The behaviour of functionalised CI to a drop of water can be seen in Fig. 2.6.3. Carminic acid functionalised CI (carminic acid-CI) and acid-terminated-mPEG CI (PEG-CI) powders exhibited more hydrophilic behaviours compared to 1-naphthaleneacetic acid-CI (naphthalene-CI) (Fig. 2.6.3) and oleic acid-CI (Fig. 2.5.2).

SEM analysis showed the surfaces of coated particles (Fig. 2.6.4) to be rougher than bare particles (Fig. 2.3.2), due mainly to etching of the particle surface by the acidic environment. The carminic acid-CI and naphthalene-CI seemed to retain more of the original shape of CI compared to the PEG-CI (Fig. 2.6.4c), which produced more irregularly shaped particles.

We were able to demonstrate the depletion of carminic acid in the presence of 100 mg of CI by monitoring the absorbance of a 5 ppm solution of carminic acid over a period of 12 min (Fig. 2.6.5). We observed a decrease in the intensity of the absorption band for carminic acid at 278 nm every 4 min which indicated carminic acid groups were adhering to the CI particles. The shifting of the peak to higher wavelengths over time is attributed to a substance leaching from the particles that affected the pH of the solution, and hence we could not provide an accurate quantitative analysis.

In a report by Zirbs et al., it was shown that the maximum grafting density attainable with PEG (5 kDa) on iron oxide nanoparticles is approximately 3×10^6 chains/ μm^2 . Furthermore, grafting densities $> 5 \times 10^5$ chains/ μm^2 for PEG-dispersants in the 3-10 kDa range have been reported as necessary for colloidal stability [37]. Therefore, the grafting density we obtained in our CI particles was too low to significantly affect the colloidal stability of the micro particles, however, it may be dense enough to interact with an active pharmaceutical ingredient (API) during crystallisation.

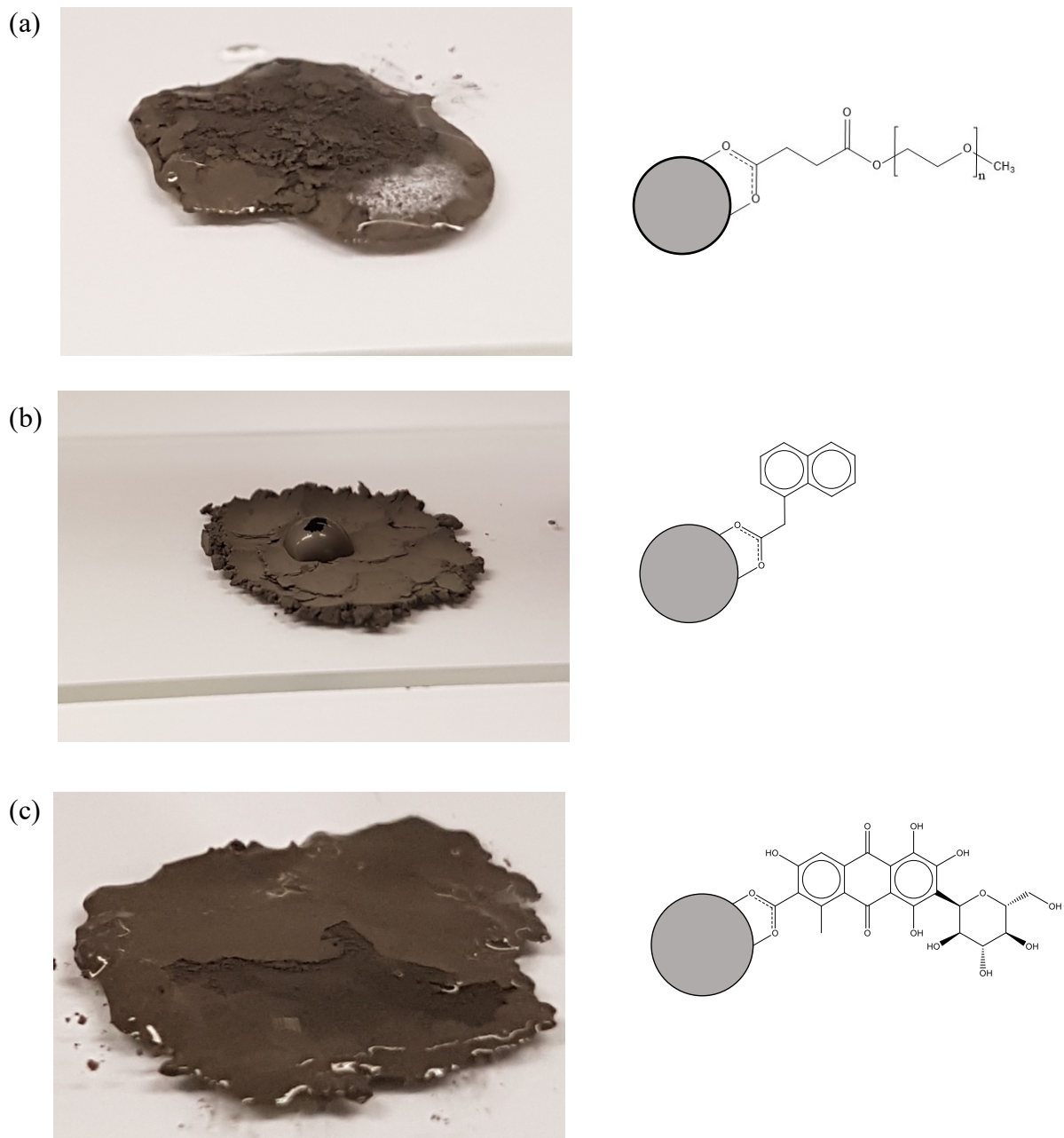


Figure 2.6.3. Optical image of water droplet on powder of (a) mPEG-CI, (b) 1-naphthaleneacetic acid-CI and (c) carminic acid-CI.

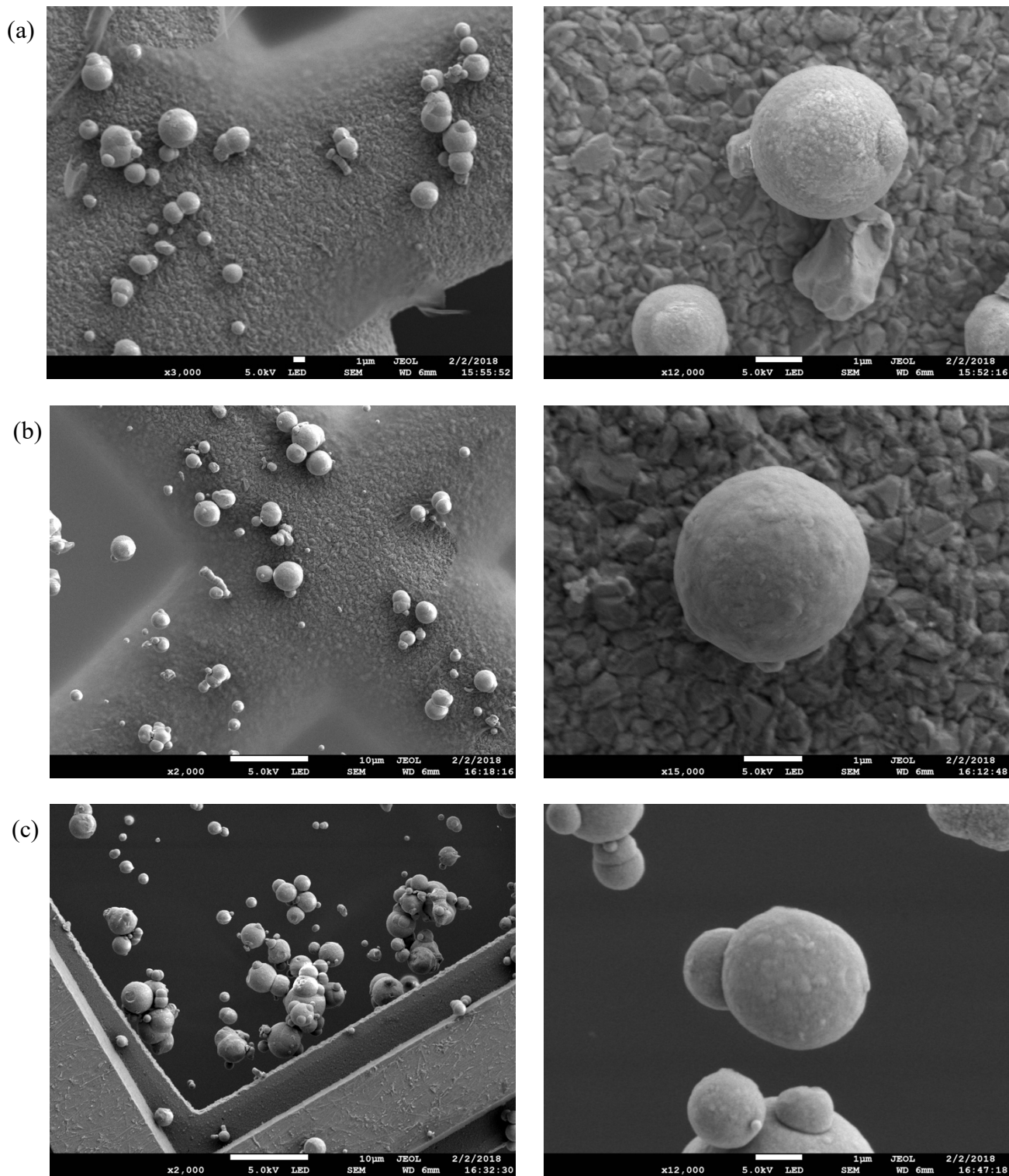


Figure 2.6.4. SEM images of (a) Carminic acid-CI, (b) 1-naphthaleneacetic acid-CI and (c) PEG-CI.

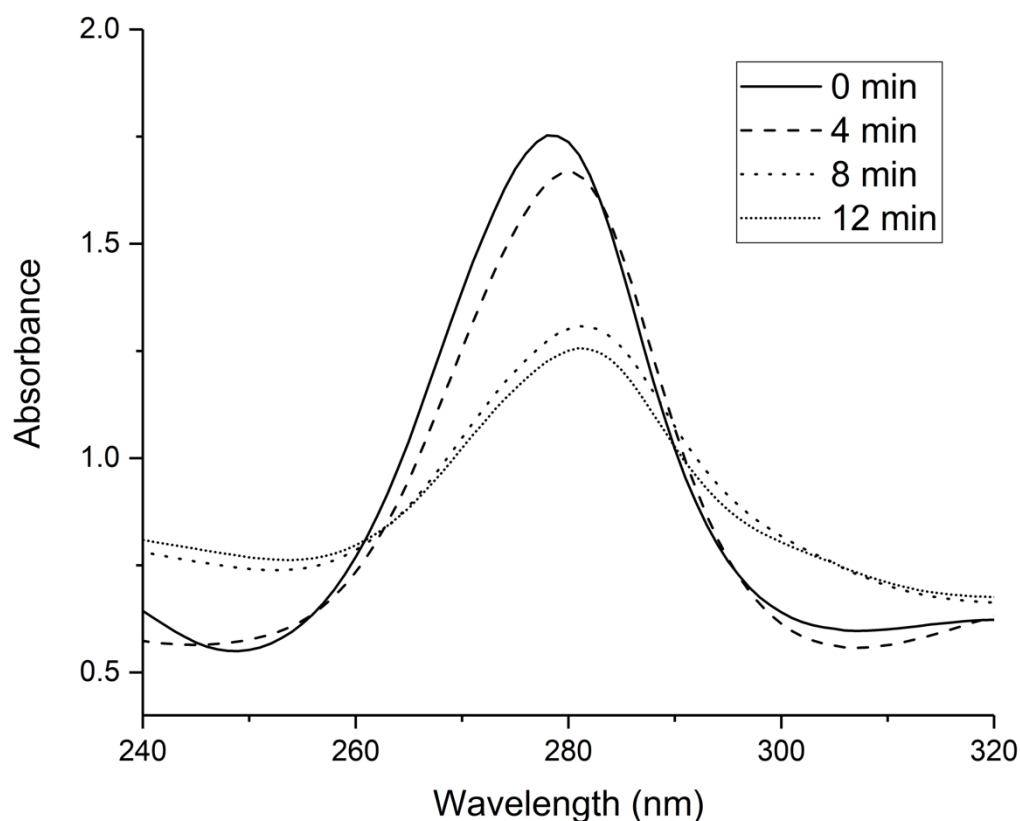


Figure 2.6.5. UV-Visible absorption spectra during the functionalisation of CI with carminic acid.

2.7 Crystallisation of Carbamazepine in Toluene MR Fluids. In this study we examined the anticonvulsant drug carbamazepine (CBZ) because it is an active pharmaceutical ingredient (API) which serves as a model compound for many studies on polymorphism [74, 75]. CBZ's bioavailability has been shown to be dependent on the polymorph administered, and therefore its polymorphism plays a crucial role in pharmacokinetics [76]. There are four known polymorphs of CBZ, the details of which are summarised in Table 2.7.1, each of which demonstrate different thermal stabilities. It has been shown that the most stable of the polymorphs at room temperature is the monoclinic form III, the commercially available form, and the only one which exhibits the desirable therapeutic effects [77].

We wanted to determine if MR fluids can be used to affect the polymorphism of CBZ during crystallisation. To do this, we needed to determine if the particle functionality interacted with the API to affect the packing of the crystal units and promote one crystal habit over another.

Table 2.7.1. Known polymorphs of Carbamazepine (CBZ)^(b).

Form	Space Group	Habit	Stability Order	Crystallisation Method
I	Triclinic P1	Needle	2	Melt at 192 °C
II	Trigonal R3	Needle	4	Cooled (5 ° C) from ethanol for 5 h
III	Monoclinic P2 ₁ /c	Block	1	Slow evaporation from ethanol
IV	Monoclinic C2/c	Prism	3	Slow evaporation from ethanol in the presence of hydroxypropyl cellulose

^(b)Data was collected from [78] and formatted according to [57].

Crystallisation of CBZ was initially performed in 1.73 mL of toluene containing 1 g of CI and 20 mg of CBZ. This solution was sonicated for 1 min and placed into a 70°C water bath for 10 min, after which the CBZ had dissolved. The solution was then shaken to disperse the particles and immediately placed in-between the poles of an EPR magnet (like in Fig. 2.3.3) using a Styrofoam support, for 12 h, in a 21 °C air-conditioned room. Control crystallisations of CBZ under identical conditions, i.e. without CI, were performed in parallel. Crystallisations were performed at 200 and 1000 G, where the higher magnetic field resulted in higher MR fluid viscosities. We observed that under control conditions (no CI), the crystal habit was evenly populated by needles and blocks (Fig. 2.7.1), which we later confirmed by XRD to be the monoclinic form III (block) and trigonal form II (needle).

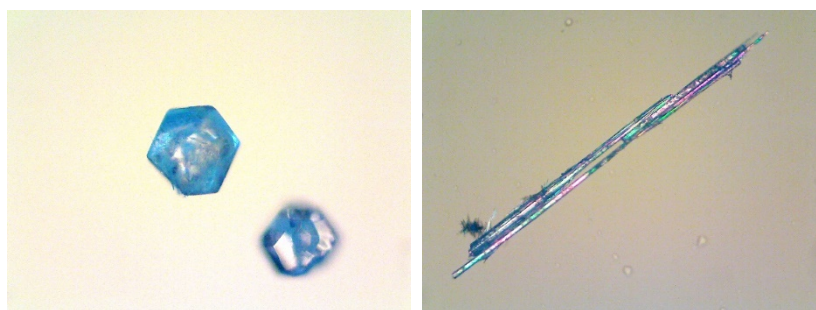


Figure 2.7.1. Optical microscopy (10x magnification, 1.6 mm field of view) of CBZ grown in toluene containing no CI.

The magnetorheological (gelation) effects on crystal habit became apparent when crystallisation in a bare-CI MR fluid resulted in a shift in crystal habit from block and needle to predominantly needle (Fig. 2.7.2a). An effect of particle functionalities on crystal morphology was observed when crystallisation in oleic acid grafted particles (oleic acid-CI) shifted the crystal habit completely towards block, both at 200 (Fig. 2.7.2c) and 1000 G (Fig. 2.7.3c), and the crystallisation in PEG-CI (Fig. 2.7.2b and 2.7.3b) and bare-CI (Fig. 2.7.2a and 2.7.3a) produced needle structures. Control experiments containing toluene and 20 μL of oleic acid showed needle formation as opposed to blocks, confirming that the combined effect of gelation and particle functionalities is responsible for the crystal habit shift (Fig. 2.7.3d).

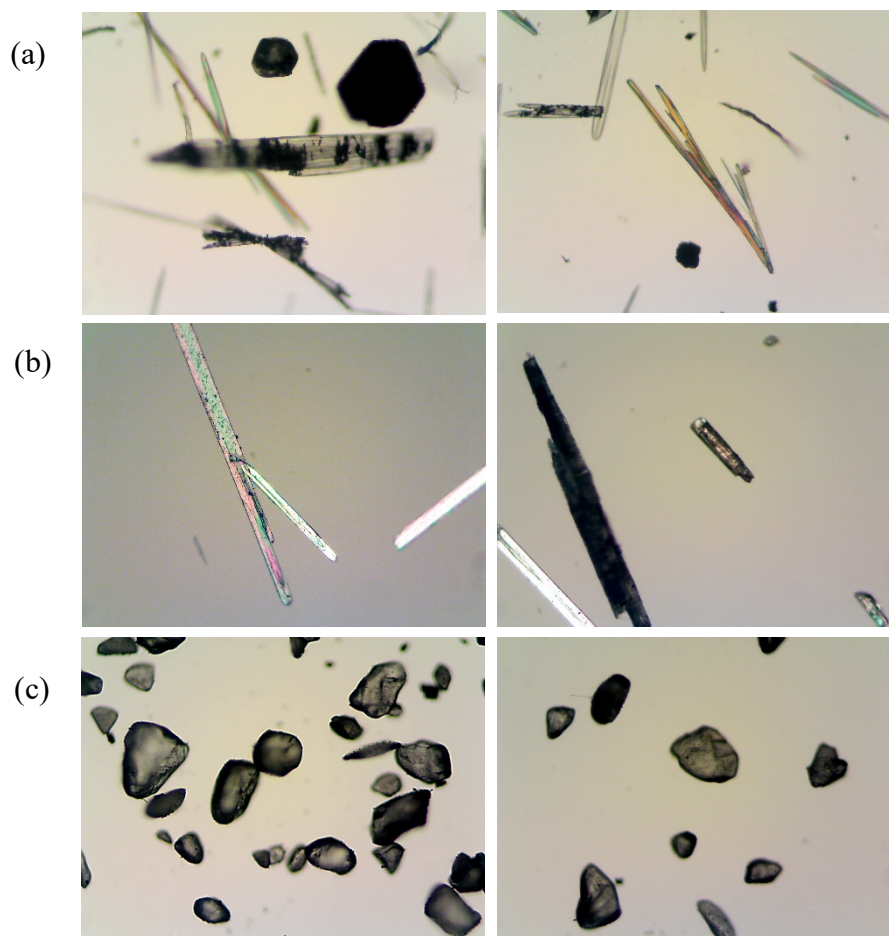


Figure 2.7.2. Optical microscopy (10x magnification, 1.6 mm field of view) of CBZ grown in toluene containing (a) bare CI, (b) PEG-CI and (c) Oleic acid-CI in a 200 G magnetic field.

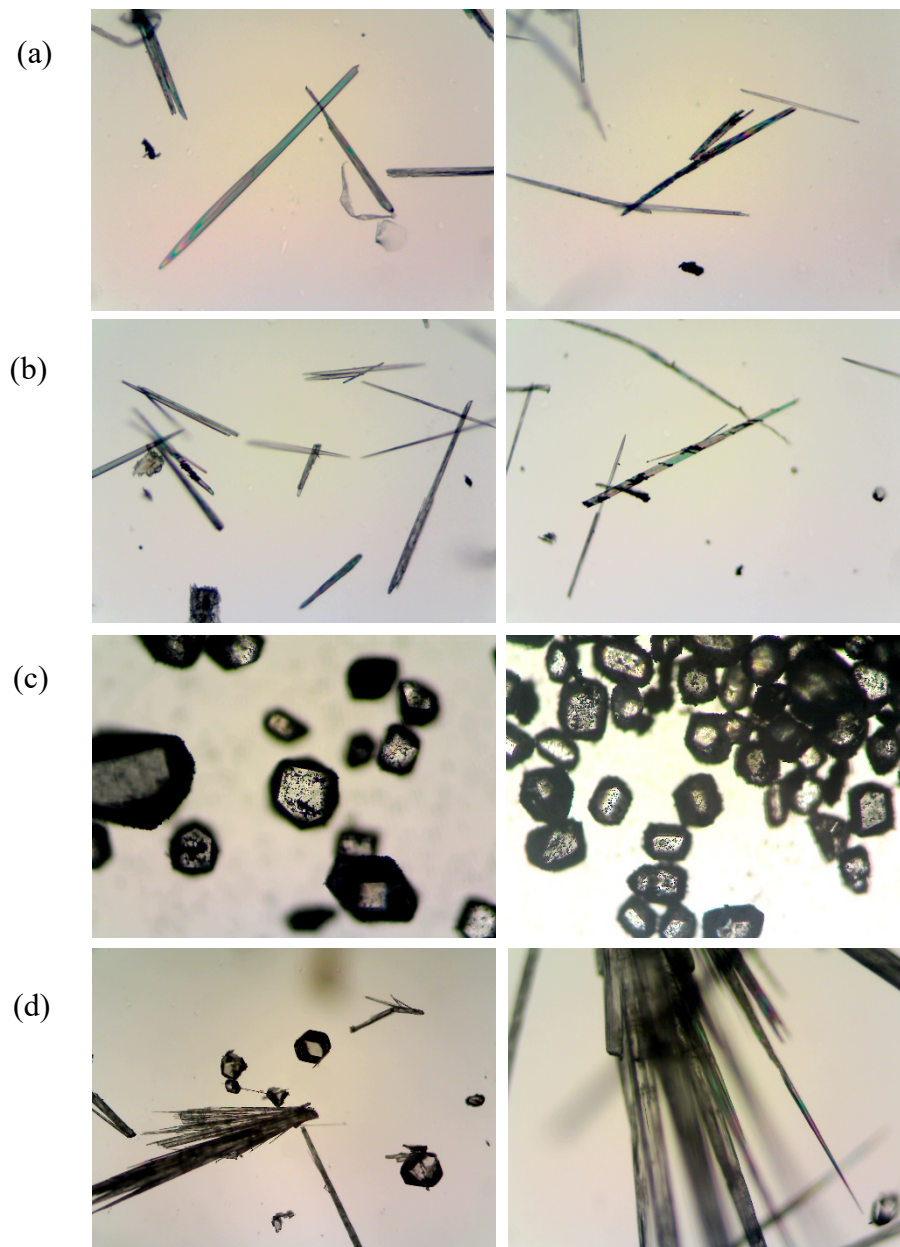


Figure 2.7.3. Optical microscopy (10x magnification, 1.6 mm field of view) of CBZ grown in toluene containing (a) bare CI, (b) PEG-CI, (c) Oleic acid-CI and (d) 20uL of Oleic acid in a 1000 G magnetic field.

Comparisons of the optical images in Fig. 2.7.2 (200 gauss) and Fig. 2.7.3 (1000 gauss) reveal few differences between these crystals. However, it can be noted that the crystallisations at 200 G produced slightly larger needles than those at 1000 G, and that the block formations at 1000 G had more flat surfaces (Fig. 2.7.3c). From this result we can see that the magnetic field strength has little effect on crystal habit and the cause of the effect of particle functionalities on crystal habits is not clear.

To better understand the effect of particle functionality on CBZ crystal habits we considered the molecular packing of each form (Fig. 2.7.4). It is important to note that the differences among crystal forms lies solely in the packing of the carboxamide dimer units, described by the pattern of weak hydrogen bonding interactions present in all the forms [78]. The polymorphism between the triclinic and trigonal (needle) morphologies arises from the alternative packing of these dimers, where they are packed with offset π - π stacking of the aromatic rings (Fig. 2.7.4a and 2.7.4b). In the monoclinic forms the dimer units pack edge-to-face π - π stacking of the aromatic rings (Fig. 2.7.4c and d).

We therefore extended this concept to study the effect of a non-polar aromatic functionality, 1-naphthaleneacetic acid, and a polar aromatic functionality, carminic acid. Crystallisations of CBZ were performed in naphthalene-CI and carminic-CI at 1000 G under conditions identical to previous crystallisations.

The results of these crystallisations (Fig. 2.7.5) suggest that a functionality with no potential for hydrogen bond donation, in this case the non-polar naphthalene, results in a shift towards a block crystal habit (Fig. 2.7.5b). At the same time, a functionality with hydrogen bond donating potential, the polar carminic ligand, results in a needle crystal habit (Fig. 2.7.5a). This indicates that hydrogen bonding interactions between the API and the particle functionality are more significant than π - π interactions in affecting crystal habit. Furthermore, it can be readily seen from the results summarised in Table 2.7.2 that functionalities with no hydrogen bond donating potential like oleic acid and 1-naphthaleneacetic acid, produce a shift towards block crystal habits, while functionalities with the ability for hydrogen bond donation result in needle formations. The lack of hydrogen bond donors in the oleic and naphthalene functionalities means that π - π interactions between the CBZ dimer units dominate and determine crystal habits.

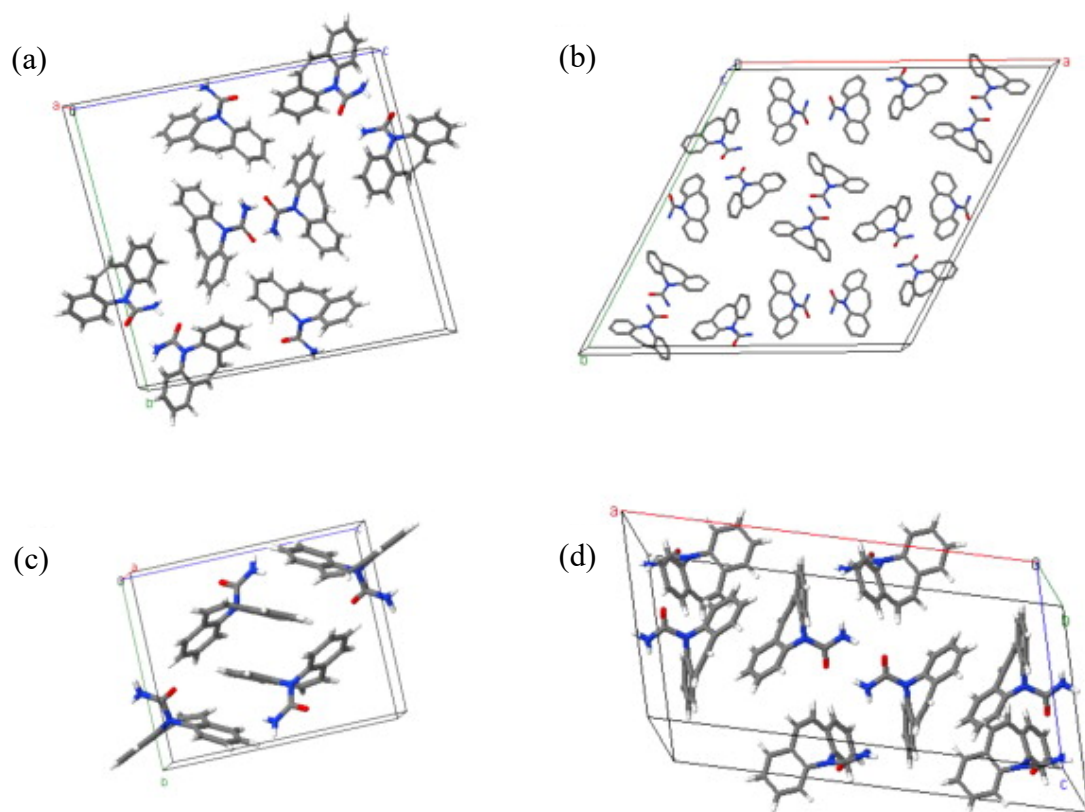


Figure 2.7.4. Packing diagrams of (a) form I, (b) form II, (c) form III and (d) form IV of CBZ showing hydrogen-bonding patterns. Reprint from [78].

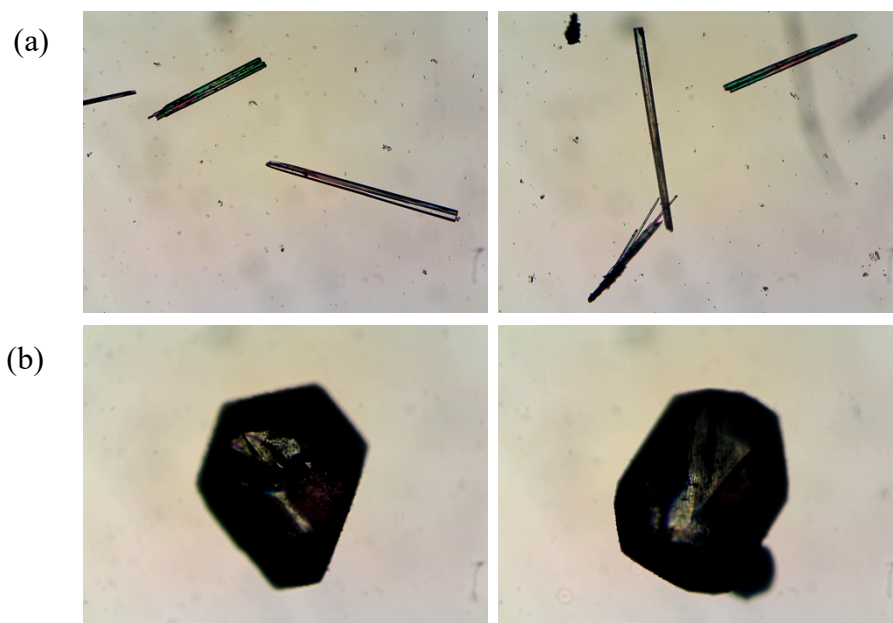


Figure 2.7.5. Optical microscopy (10x magnification, 1.6 mm field of view) of CBZ grown in toluene containing (a) carminic-Cl, (b) naphthalene-Cl in a 1000 gauss magnetic field.

Table 2.7.2. Summary of crystallisations of CBZ in toluene MR fluids at 1000 gauss.

Functionality	Habit	Space Group ^(c)	Form
Pure Toluene	Mixed Needle and Block	Trigonal R3	II + III
Bare	Needle	Trigonal R3	II
Carboxylated mPEG	Needle	Trigonal R3	II
Carminic Acid	Needle	Trigonal R3	II
Oleic Acid	Block	Monoclinic P2 ₁ /c	III
1-Naphthaleneacetic Acid	Block	Monoclinic P2 ₁ /c	III

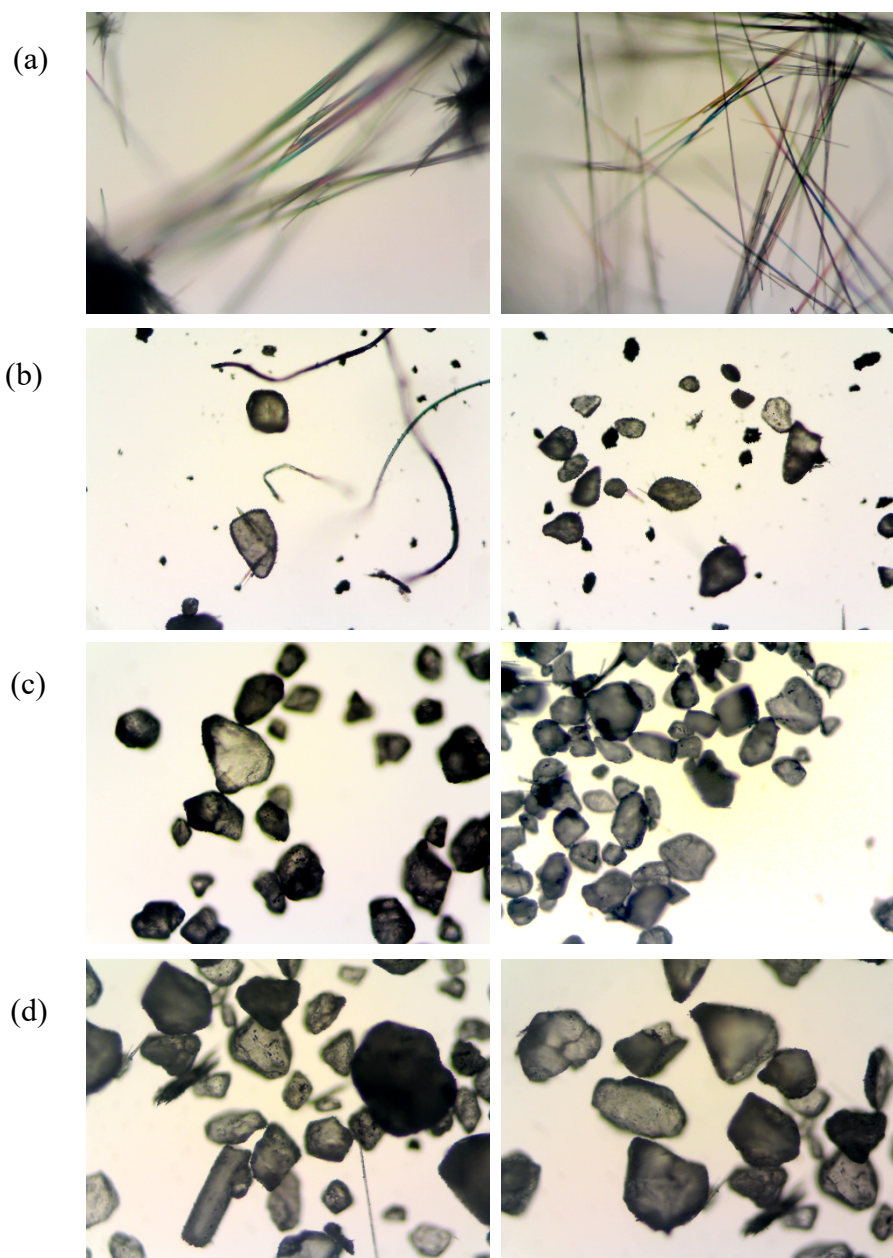
^(c)Space groups were determined by running a pre-experiment data collection on a Rigaku Oxford XRD instrument.

Favourable interactions between particle functionality and solute molecules (API) may direct the CBZ molecules toward an orientation that reduces the entropic cost of nucleation and therefore the particles may serve as active nucleation sites [58].

There is work on the polymorphism of calcium carbonate in chitosan gels that indicates that the gel may act as a high energy surface capable of actively nucleating new crystal forms. The nucleation of the vaterite form at the interface of the chitosan gel is stabilised through hydrogen bonding interactions with other flexible chitosan chains [79]. It is possible that the CI particles act as nucleation sites onto which successive layers of CBZ can deposit and become stabilised through hydrogen bonding interactions with the CI functionalities. Extending this concept may help to explain the variations observed in crystal clarity. For example, some of the crystals, particularly the block formations, appeared dark in colour and seemed to be speckled with CI particles (Fig. 2.7.2c, 2.7.3c, 2.7.5b). In fact, crystals grown in oleic acid and naphthalene functionalities seem to contain more CI particles than those grown in PEG-CI or carminic-CI. The observation that crystals grown in the presence of non-polar functionalities retain more carbonyl iron particles is evidence of an attractive force between the particle functionality and CBZ. Taking into account the fact that a lack of hydrogen bond donors in these functionalities means that π - π interactions dominate; it is likely that these π - π interactions cause CBZ to crystallise by nucleating on the CI particles, rather than on defects native to the container.

2.8 Crystallisation of Carbamazepine in water MR Fluids. In distilled water the solubility of CBZ is significantly lower than in Toluene. Optimising conditions for

crystallisation in water required a decrease in the amount of CBZ to 5 mg, however all other procedures for crystallisation of CBZ remained the same. Under these conditions we observed that crystal habit was only influenced by the effect of gelation, which was responsible for the shift in crystal habit from needle (Fig. 2.8.1a) to block (Fig. 2.8.1b-f). The particle functionalities were rendered ineffective, as the block crystal habit was observed in the bare and functionalised CI. It is likely that the use of a polar solvent, i.e. water, out-competed the hydrogen bonding effects of the functionalities leading to one crystal habit. We posit that the hydrogen bonding interactions of CBZ with water directed the orientation of CBZ molecules causing them to nucleate in a way that produced block formations.



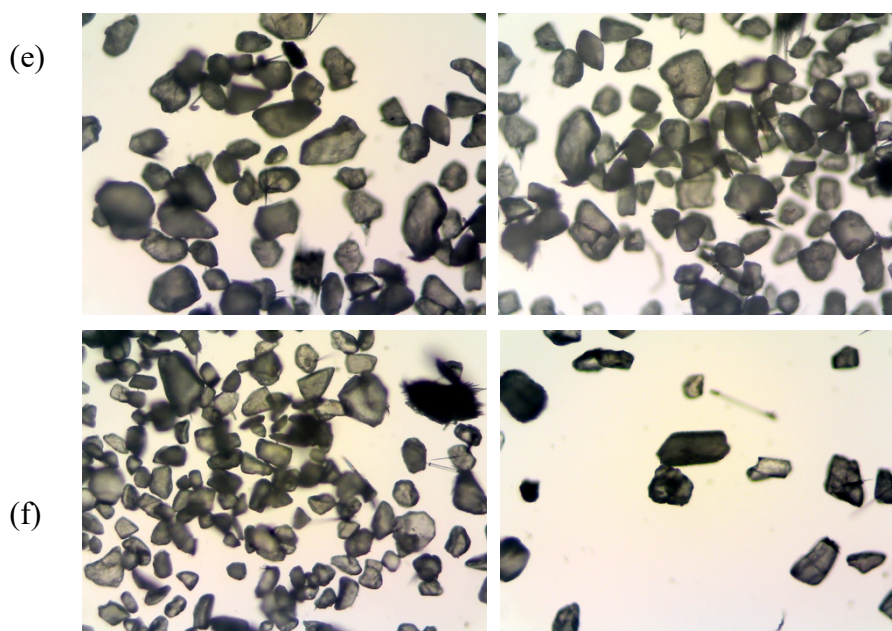


Figure 2.8.1. Optical microscopy (10x magnification, 1.6 mm field of view) of CBZ grown in water containing (a) pure solvent, (b) Bare-CI, (c) PEG-CI, (d) Oleic acid-CI, (e) Carminic-CI and (f) Naphthalene-CI in a 1000 G magnetic field.

Furthermore, the confinement effect of gelation coupled with the hydrogen bonding interactions with water likely created an environment which entropically preferred a block habit.

2.9 Separation of CBZ Crystals from MR Fluid. Magnetorheological fluids have the advantage of being reversible. These fluids can be switched “on” or “off” by a magnetic field, and it is this reversible nature that allows for easy recovery of crystals. In our experiments, the crystals were collected by magnetically separating the particles from the carrier fluid and filtering. The particles were rinsed several times with the carrier fluid, sedimented using a neodymium magnet, and the solution was filtered to collect the crystals. In contrast, LMWG and hydrogels require the use of solvents, or in some cases gel removal may involve acid hydrolysis or heating [80]. These methods of separation can permanently damage the crystals and therefore have serious limitations. Our method is only limited by the possible interactions between carrier fluid and CI particles, for example low pH fluids may dissolve the CI. Overall, MR fluids can serve as effective crystallisation media for API.

2.10 Conclusion. We have demonstrated the use of magnetorheological fluids as a medium for crystal growth. The reversible nature of the MR effect allows for the facile recovery of crystals. The observation that carboxylic acid moieties can be used to modify the surfaces of CI particles provides the ability to design an MR fluid to match a wide range of crystallisation conditions. Clear differences in crystal habit were observed as a result of varying CI particle functionalities, indicating that control of polymorphism is possible. However, the exact nature of the interactions between functionality and API have not yet been determined. Nevertheless, by introducing different particle functionalities, we were able to control the crystal habits of CBZ in toluene MR fluids.

Chapter 3

Synthesis and Surface Modification of Magnetite Nanoparticle Clusters

Chapter 3. Synthesis and Surface Modification of Magnetite (Fe₃O₄) Nanoparticle clusters

3.1 Background. MRI-guided magnetic thermotherapy exploits the heat generation ability and magnetic properties of biocompatible iron oxide (Fe₃O₄) to facilitate local cellular-level heating of deep tumours. The actual therapeutic effects of magnetic hyperthermia treatments depend on the heating efficiency of magnetic nanoparticles (MNPs). These MNPs can generate heat via hysteresis loss, Néel relaxation and Brownian relaxation under the influence of an alternating magnetic field (AMF). The levels of heat-generation required to raise tumour temperatures to values lethal to cancer cells (above 42.5 °C) cannot be realized by the most conventional biocompatible iron oxide nanoparticles [81, 82]. It is known that heat-generation power of nanoparticle clusters is related to the strength of magnetic-dipole interactions between nanoparticles in the cluster and that the magnetic dipole interaction energy is inversely proportional to particle-particle separation (l):

$$E = -\frac{(\mu_0 m_0^2)}{(4\pi l^3)} \quad (1)$$

where μ_0 is the magnetic permeability of a vacuum and m_0 is the magnetic moment [83]. Therefore, decreasing particle-particle separation can enhance heat-generation power. This theory led Hayashi et al. to create a “tight” clustering of magnetic NPs with zero particle-particle separation – significantly increasing the heat-generation efficiency of magnetite (Fe₃O₄).

An alternative application of magnetic heating for cancer cell death is to use the local heating afforded by nanoparticles to trigger a phase transition in a polymer coating, and hence release an anticancer drug [84]. Crucially, for biocompatibility, a highly solvated polymer brush must be used to suspend the nanoparticles in biological media. Poly-N-isopropyl acrylamide (PNIPAM) provides a good alternative to the more commonly used PEG functionality as it provides the high aqueous solubility necessary to disperse nanoparticles, but also exhibits a drastic change in solvation at ~32 °C, referred to as its low critical solution temperature. Low critical solution temperatures (LCST) describe the behaviour of polymer solutions which display a decrease in solubility with a rise in temperature. This phenomenon is

due to an unfavourable entropy effect, where the entropy of mixing is negative, an input of heat energy results in a phase transition in the polymer resulting in a phase separation [85]. This low critical solution temperature (LCST) provides the means for a reversible temperature-induced aggregation of nanoparticles [68].

The LCST behaviour of PNIPAM, coupled with the high heat generation efficiency of clustered magnetite particles can provide an efficient means to direct and concentrate nanoparticles in a tumour. In this chapter, we present the methods of synthesis and surface modification of iron oxide clusters.

3.2. Synthesis of Iron Oxide Clusters. We first attempted to recreate the literature procedure for the synthesis of iron oxide NP clusters [81]. The novelty in our study is based around the functionalisation of these clusters with a temperature sensitive polymer, which we cover later in this chapter (section 3.4).

Iron oxide clusters were synthesised by first polymerising pyrrole-3-carboxylic acid (PyCOOH) using iron (III) ions as an oxidant in an aqueous solution of polyvinyl alcohol (PVA). According to Hong et al. PVA forms coordination bonds with iron cations in solution that form clusters of the water-soluble polymer and iron cations [86], this allowed the reaction to proceed according to dispersion polymerisation. The addition of pyrrole-3-carboxylic acid resulted in the formation of polypyrrole nanoparticles (PPy NPs) containing embedded iron (III) ions. Some of the iron (III) ions in the PPy NPs were then reduced and hydrolysed using hydrazine to produce Fe₃O₄ NPs encapsulated in a pyrrole polymer shell (Fig. 3.2.1) [86]. The particles were collected by centrifugation and redispersed in distilled water repeated three times to wash the NP clusters. The clusters were then stored in distilled water in centrifuge tubes at 4 °C in the dark.

Dynamic light scattering (DLS) analysis was performed on the iron oxide clusters by sonicating the stock solution for 5 min and then taking 1 mL and diluting it into 4 mL of distilled water. The samples were left to equilibrate to room temperature and then sonicated for 5 min before collecting the data. DLS indicated that the clusters had an average hydrodynamic diameter of 133.1 ± 0.2 nm. NP clusters were observed by TEM by drying a droplet of the NP solution on a Cu TEM grid. TEM analysis revealed that cluster sizes were

significantly smaller than those observed by DLS. It can be seen from Fig. 3.2.2a that the clusters are significantly smaller than 133 nm and that they are surrounded by strings of nanoparticles linked together in a network.

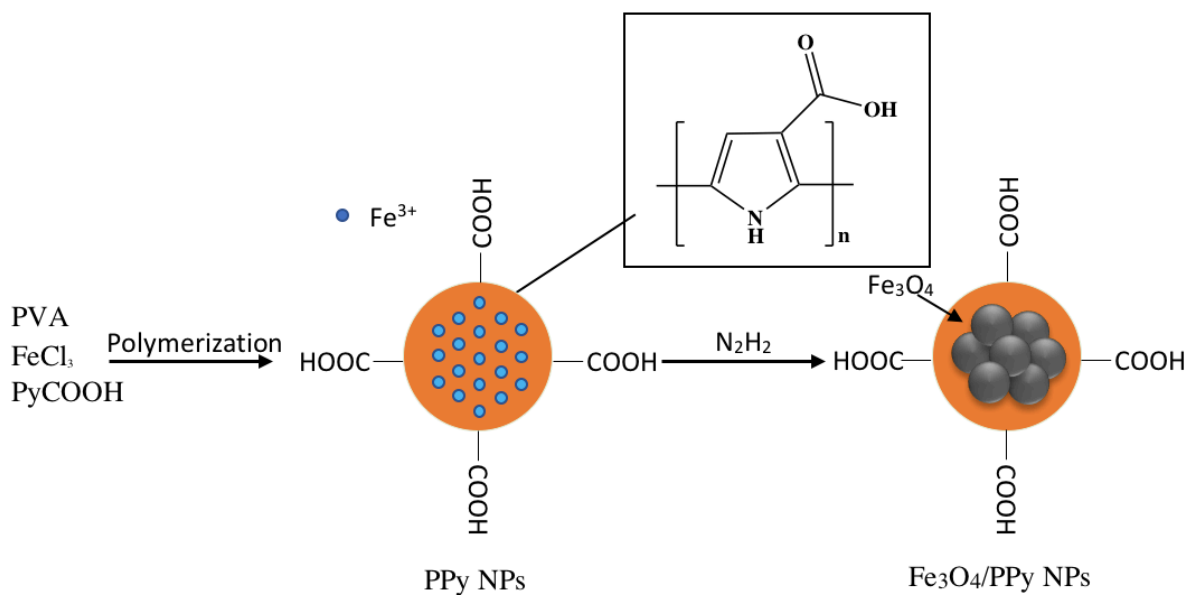


Figure 3.2.1. Schematic Representation of nanoparticle cluster synthesis

Considering that the DLS instrument performs a measurement by assuming spherical particles, it isn't surprising that our measurements registered this network as a single structure and hence recorded such large diameters.

It is also clear from these images that clusters have begun to form, as shown by the concentration of dark structures (Fig. 3.2.2a). However, these iron oxide cores display non-uniform size distributions with sizes ranging between 20-30 nm and lack any uniform shape. Furthermore, the strings of iron oxide NPs (Fig. 3.2.2a) observed in this sample were also incongruent with expected results, where monodisperse clustered structures were expected. The lack of uniform shape and size suggests that there is an issue with the step involving the formation of PPy NPs. Since the PPy NPs act as a scaffold for the iron oxide cores, the resulting shape and size of the PPy NPs should influence the morphology of the resultant

clusters. According to a study on the formation of PPy NPs [86], the complexation of iron cations to polyvinyl alcohol (PVA) is influenced by the PVA concentration.

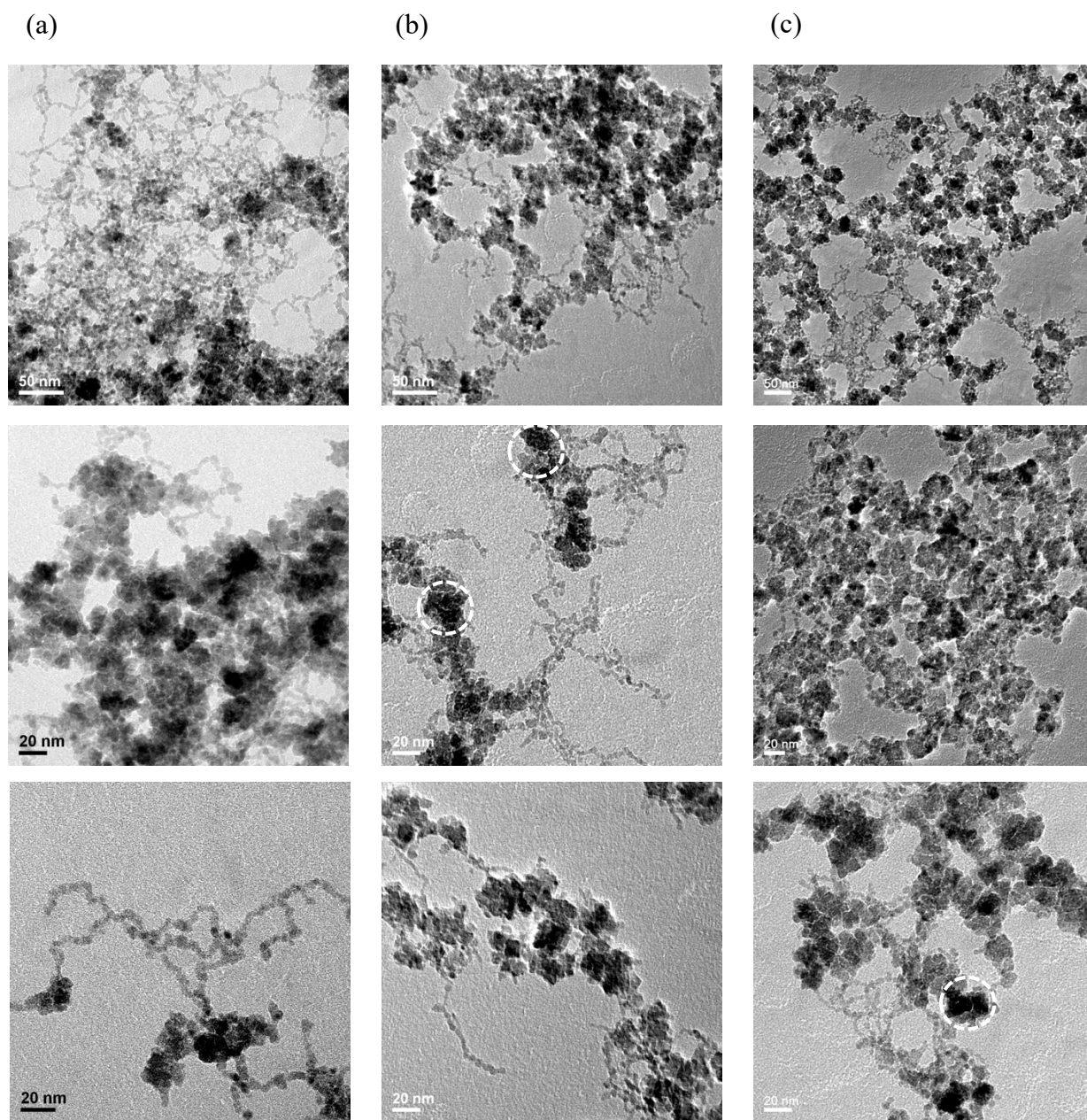


Figure 3.2.2. TEM images of (a) Fe_3O_4 clusters prepared with 3.8% PVA, (b) Fe_3O_4 clusters prepared with 7% PVA and (c) Fe_3O_4 clusters functionalised with PNIPAM.

It is considered that the complex becomes more sterically stable with increasing PVA concentration, where the chain conformation of the polymer switches from a random coil to globular (Fig. 3.2.3). Fig. 3.2.3 shows how the polymer adopts a more spherical tight-knit shape at higher PVA polymer concentrations.

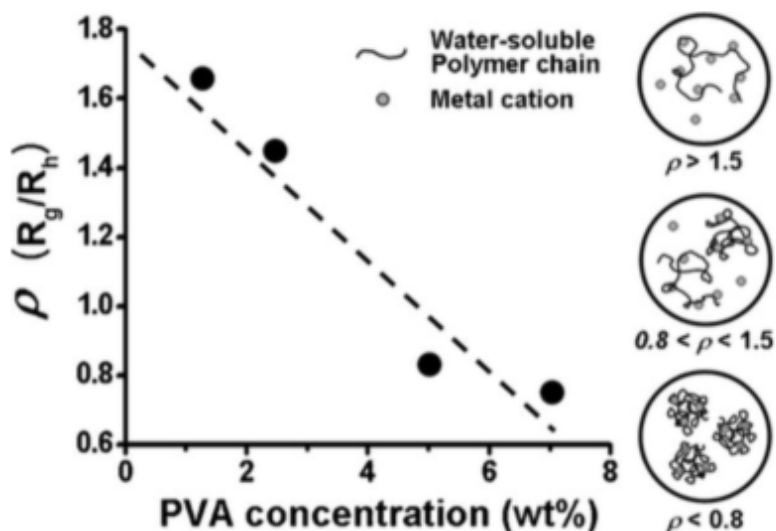


Figure 3.2.3. Changes in shape factor as a function of PVA concentration. Reprint from [86].

Following this reasoning the cluster synthesis was modified by increasing the PVA concentration from 3.8% to 7% in 10 mL of water, unfortunately, we were not able to reproduce this graph as increased PVA concentrations did not produce easily observable differences as seen in Fig. 3.2.2b. It can be readily seen from the separation of the dark black structures that more monodisperse clusters have formed (white circles). Although strings of nanoparticles are still present, they seem to be aggregating more than those in Fig. 3.2.2a. DLS analysis parameters were modified to account for the higher viscosity of PVA compared to water which put the cluster sizes at 91.14 ± 2.5 nm. However, TEM images indicate the clusters are no larger than 50 nm making it clear that the network of particle strings is still interfering with the DLS measurement. Nevertheless, functionalisation of the nanoparticles with a temperature sensitive polymer was attempted.

3.3 Polymer Synthesis and Characterization. To modify the nanoparticle cluster surfaces with poly-N-isopropyl acrylamide (PNIPAM), we had to modify the polymer with a termination that could be easily added to the carboxylic acid terminated surfaces decorating the clusters. Considering that COMU offers a facile and efficient method for amidation [87], we decided to add an amine termination to PNIPAM (Fig. 3.3.1).

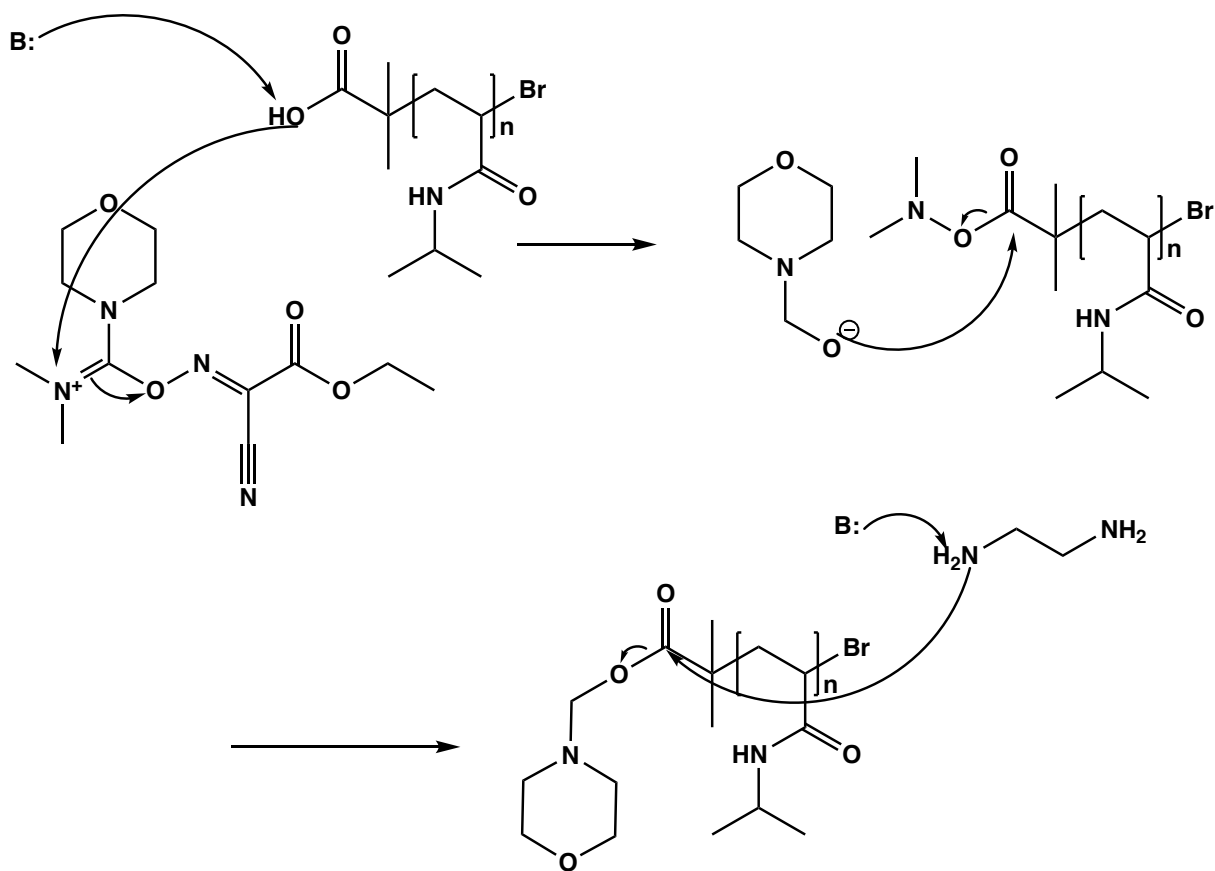


Figure 3.3.1. Coupling mechanism for COMU in the reaction between ethylenediamine and PNIPAM with DIPEA as the base.

The acid terminated poly(N-propylacrylamide) (PNIPAM) was synthesised by atom-transfer radical-polymerization (ATRP) of NIPAM to obtain a 93% yield. The polymer was then modified with ethylenediamine using COMU as a coupling agent, resulting in an amine functionalised PNIPAM (A-PNIPAM) (Fig. 3.3.2). Excess amine was removed by dialysis to

facilitate characterization and the polymer was dried, resulting in a 23% yield. The low yield in the coupling of ethylenediamine to PNIPAM could not be explained. Repeat syntheses resulted in similar yields.

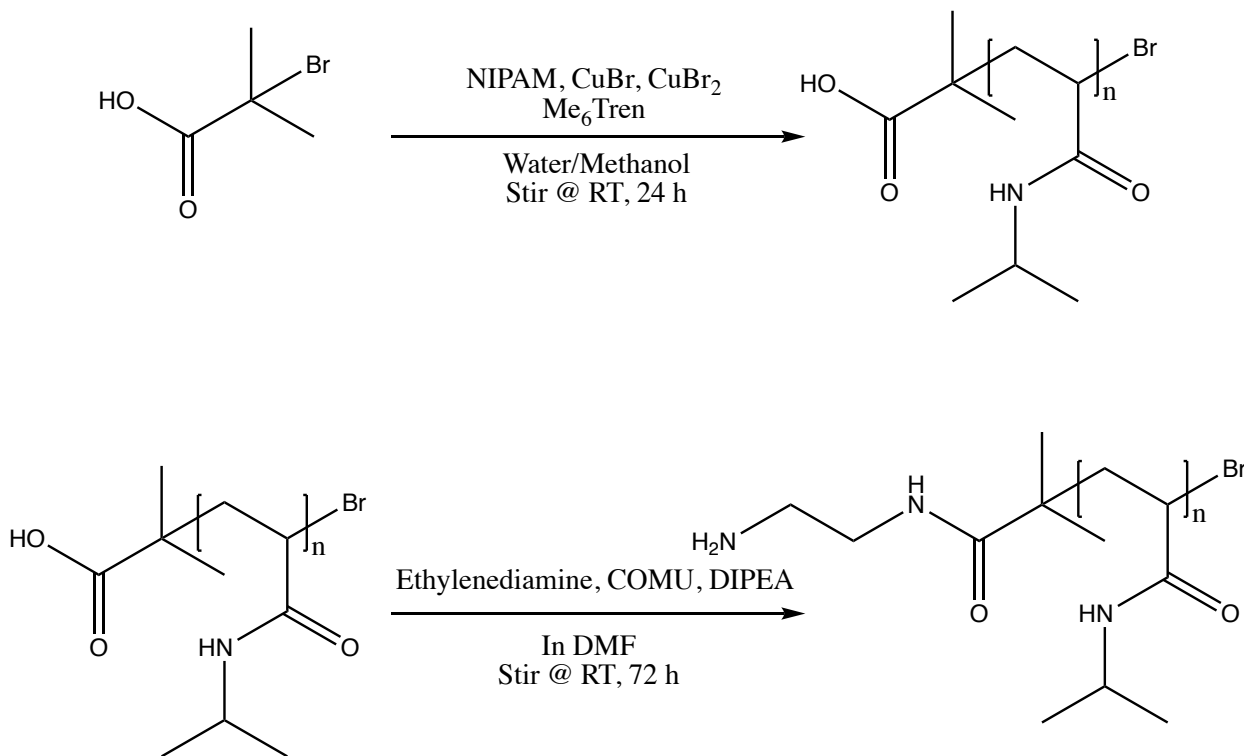


Figure 3.3.2. Synthesis of amine functionalised PNIPAM

The synthesis of acid terminated PNIPAM was confirmed by ¹H NMR spectroscopy (Fig. 3.3.3a) where the resonances at 1.12, 2.46 and 3.99 ppm were attributed to CH₃-C-CH₃, -[CH₂]_n- and CH-Br, respectively. In Fig. 3.3.3, the colours in the spectra represent the agreement of the peaks with predicted values. Green indicates good agreement and yellow indicates weak agreement with predicted values. The molecular structures are labelled with the predicted chemical shifts in ppm. The conversion of PNIPAM to A-PNIPAM was difficult to confirm by ¹H NMR spectroscopy (Fig. 3.3.3b), where the appearance of resonances at 2.87 and 2.94 ppm may correspond to the CH₂ protons in DMF, and therefore be obscuring signals from the protons in ethylenediamine.

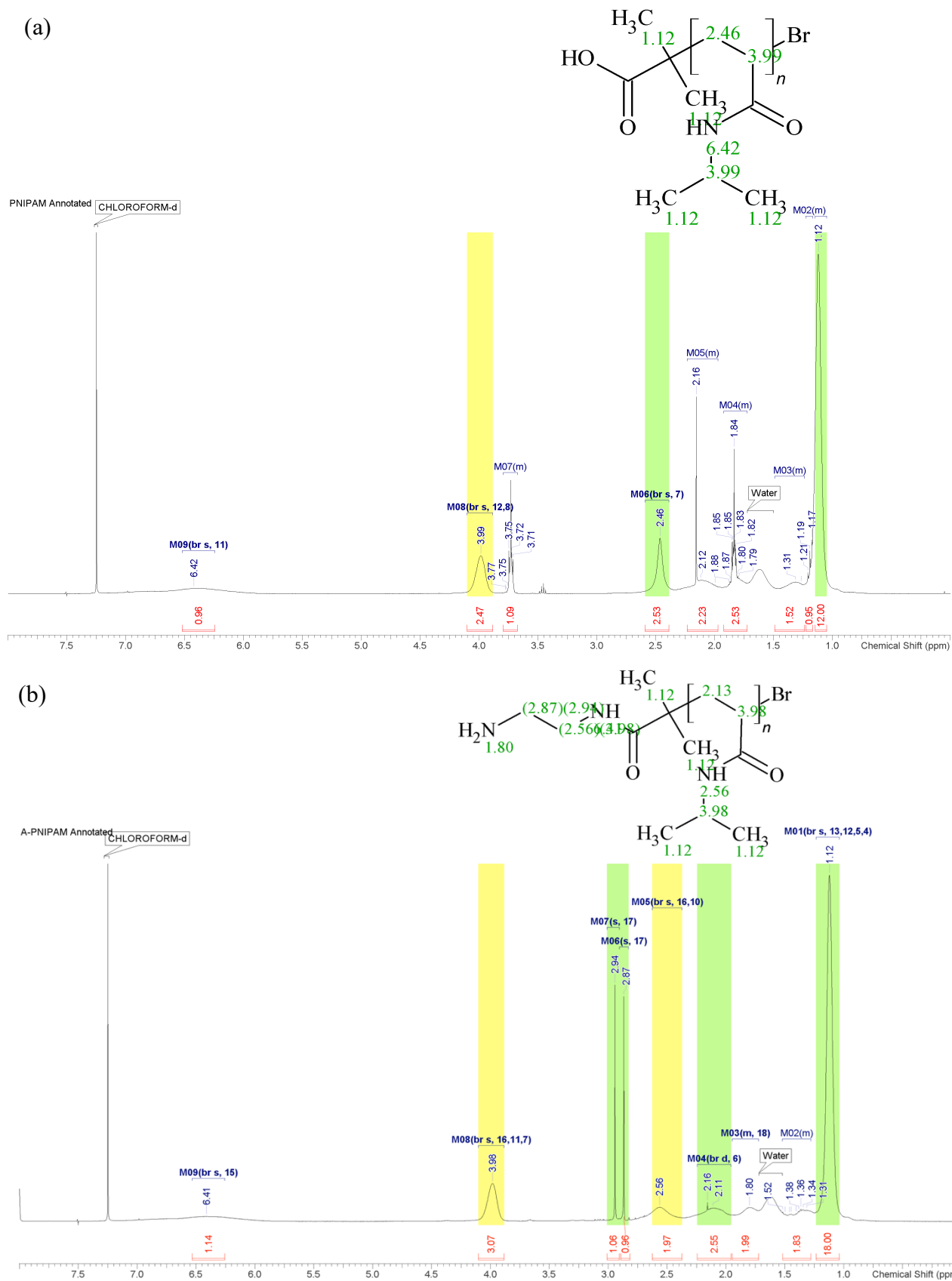


Figure 3.3.3. ^1H NMR spectra of (a) PNIPAM and (b) A-PNIPAM in CDCl_3 .

The FT-IR peaks at 3280, 1638, and 1533 cm^{-1} can be assigned to the NH protons and the amide bond in PNIPAM (Fig. 3.3.4). The FT-IR peaks found in A-PNIPAM are almost identical to the peaks found in PNIPAM however the disappearance of the peak at 1055 cm^{-1} suggests that the C-OH stretch of the terminal acid group has been replaced. MALDI-TOF mass spectrometry (Fig. 3.3.5) provided additional confirmation for the formation of PNIPAM, where the separation of mass peaks in a series corresponds to the molecular weight of the monomer NIPAM (113 Da). The average molecular weight of the synthesised polymer was also determined by mass spectrometry, and in Fig. 3.3.4 it can be readily seen that our polymer has a mass of approximately 11,000 Da.

Confirming the conversion of PNIPAM to A-PNIPAM using the data in Fig. 3.3.4 would, under extremely controlled sample preparation methods, be simple. As we demonstrated in chapter 2, it is possible to take a peak from the MALDI fingerprint for PNIPAM, add the mass corresponding to the addition of ethylenediamine (59.22 Da), and subtract the monomer weight for NIPAM (113 Da) until you arrive at a peak observed in the fingerprint for A-PNIPAM. However, our spectra seem to indicate that we did not obtain A-PNIPAM. For example, if we take the peak from the PNIPAM spectrum at 11024.8 and add the mass corresponding to the addition of ethylenediamine (59.22), we arrive at 11084.02, which is not in the A-PNIPAM spectrum. Furthermore, subtracting the monomer weight for NIPAM gets us to 10971.02 which is also not found in the A-PNIPAM spectrum. This data, coupled with lack of solid NMR spectroscopy evidence suggests that we did not obtain A-PNIPAM as our final product, regardless of having observed our product crash-out of solution above the LCST of 32 °C.

However, Cohen and co-workers [88] demonstrated that small changes in pH and matrix solution composition suppressed or favoured desorption in MALDI-TOF MS. This was due to differences in the incorporation of the analyte molecules into the matrix crystals. In fact, another phenomenon described as the Marangoni effect [89] may have influenced hydrophilic analytes to accumulate at the periphery of the sample deposit leading to discrimination effects between different oligomers and poor reproducibility. Considering our

samples were prepared at different times, our analyte fingerprints cannot be successfully compared to each other.

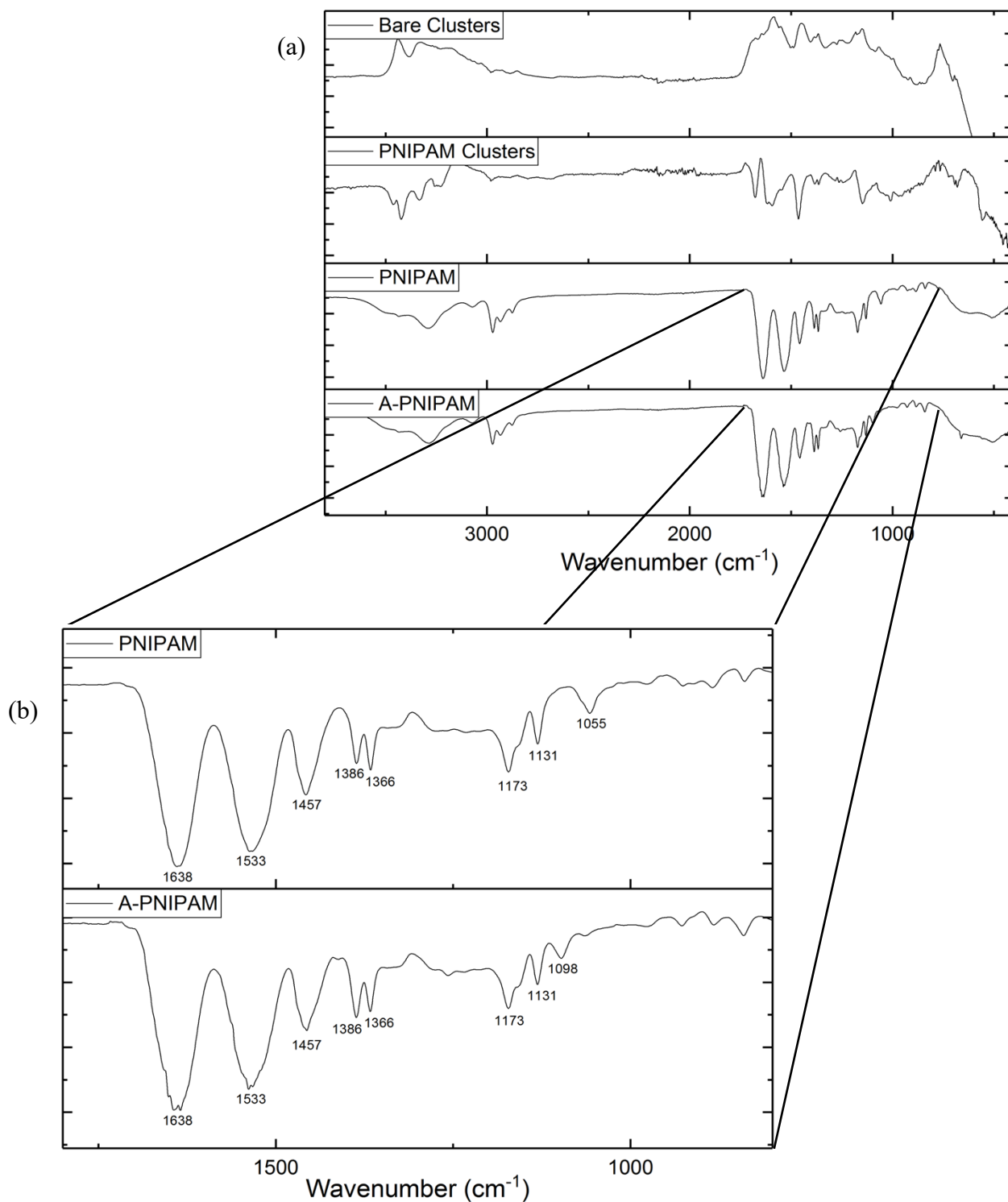


Figure 3.3.4. FT-IR spectra of (a) bare clusters, functionalised clusters, PNIPAM and A-PNIPAM and (b) selected region of PNIPAM and A-PNIPAM.

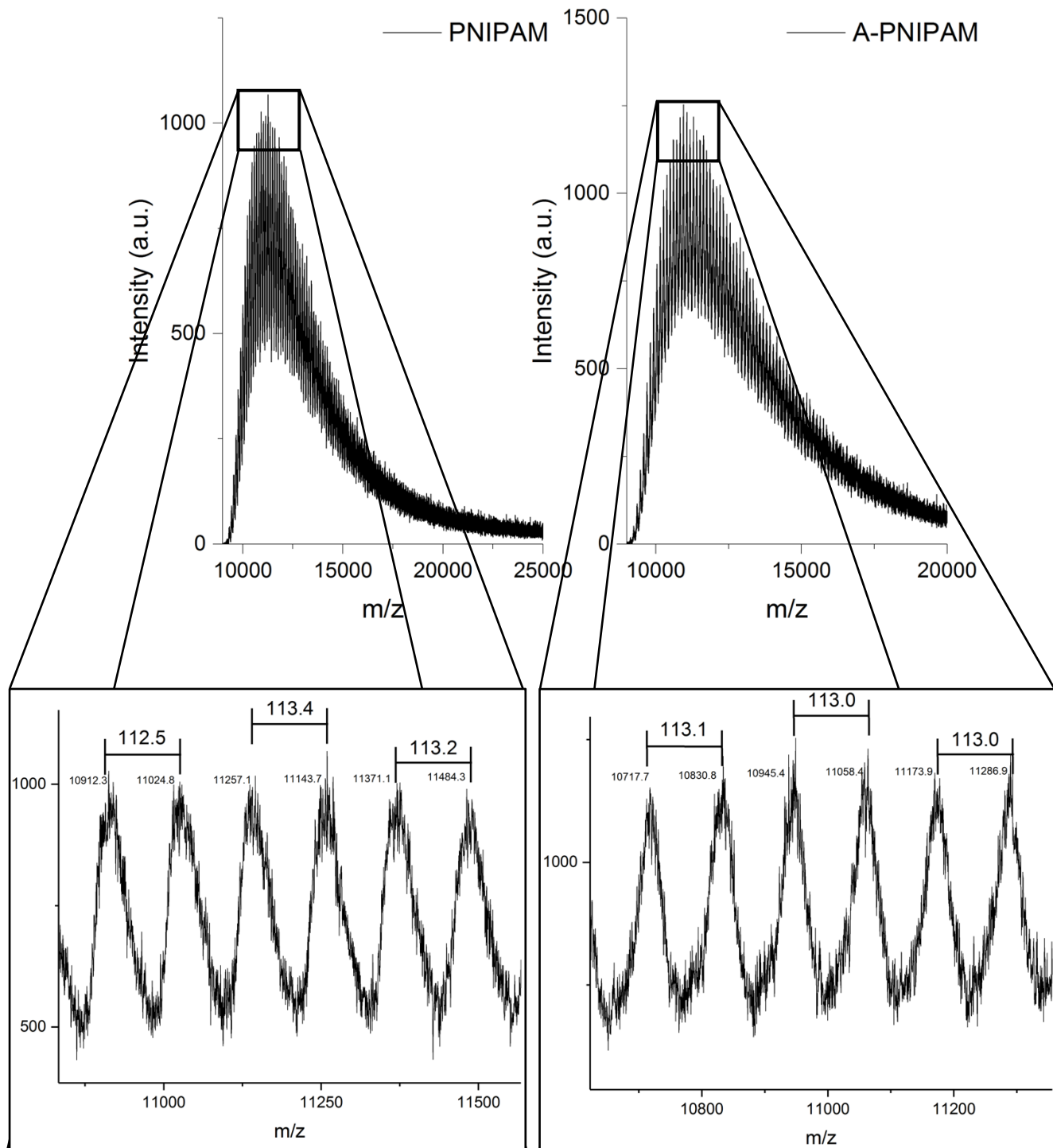


Figure 3.3.5. MALDI-TOF mass spectra of PNIPAM and A-PNIPAM where the zoomed in regions show mass peaks of a series are separated by 113 Da.

With the difficulties faced in characterising our polymer, we decided to attempt to graft the polymer we had synthesised onto our NP clusters. We assumed that if the particles exhibited a phase transition at 32 °C then we can propose that our particles contain some PNIPAM.

3.4 Functionalisation of Clusters. The amine-modified polymers (A-PNIPAM) were reacted with the carboxylic acid groups decorating the iron oxide clusters. This was done via an amidation reaction facilitated by the coupling agent COMU in DMF, following a reaction similar to that in Fig. 3.3.2. The reaction mixture was stirred at room temperature for 72 h before the particles were collected by centrifugation and re-dispersed in water.

TEM images of the functionalised clusters (Fig. 3.2.2c) show a marked change in appearance, where the clusters are surrounded by a large concentration of single nanoparticles. This may be due to the “stickier” nature of the polymer attached to the cluster’s surface. DLS measurements demonstrate a ~10 nm increase in size, indicating that the polymer was successfully grafted onto the cluster’s surface (Table 3.4.1).

The chemical structure and composition of the cluster surface was determined by FT-IR. The bands corresponding to the amine of the pyrrole ring and A-PNIPAM are highlighted by the blue box in Fig. 3.4.1. The peaks at 1682 and 1598 cm^{-1} due to N-H bending can be associated with the secondary amide bonds in A-PNIPAM (orange box). The peak at 1146 cm^{-1} due to C-N stretching in A-PNIPAM is shown in the green box. The appearance of the absorption bands attributed to A-PNIPAM indicates that the clusters were successfully grafted with the A-PNIPAM polymer.

Additionally, thermogravimetric analysis (TGA) was performed under nitrogen to accurately estimate the total organic content (TOC) on the nanoparticle clusters. The data in Table 3.4.1 was calculated using the TGA curve shown in Fig. 3.4.2 where the average grafting density was calculated from the ratio of the weight loss (200 – 600 °C) to the total surface area of the clusters, assuming the average molecular weight of A-PNIPAM from Fig. 3.3.5. A grafting density of 1.21 chains/ nm^2 was calculated for the PNIPAM functionalised clusters. In addition, the zeta potentials of the bare clusters and A-PNIPAM clusters were -38.6 and -24.0 mV, respectively (Table 3.4.1). These differences indicate a change has occurred to the bare cluster’s surface after functionalisation. However, the decrease in zeta

potential suggests that the A-PNIPAM clusters have a lower colloidal stability compared to the bare clusters, likely due to the bulky nature of the grafted polymer.

To determine if the grafted polymer could induce a phase transition on the NP clusters and cause them to aggregate, we performed a DLS analysis of the clusters as a function of temperature.

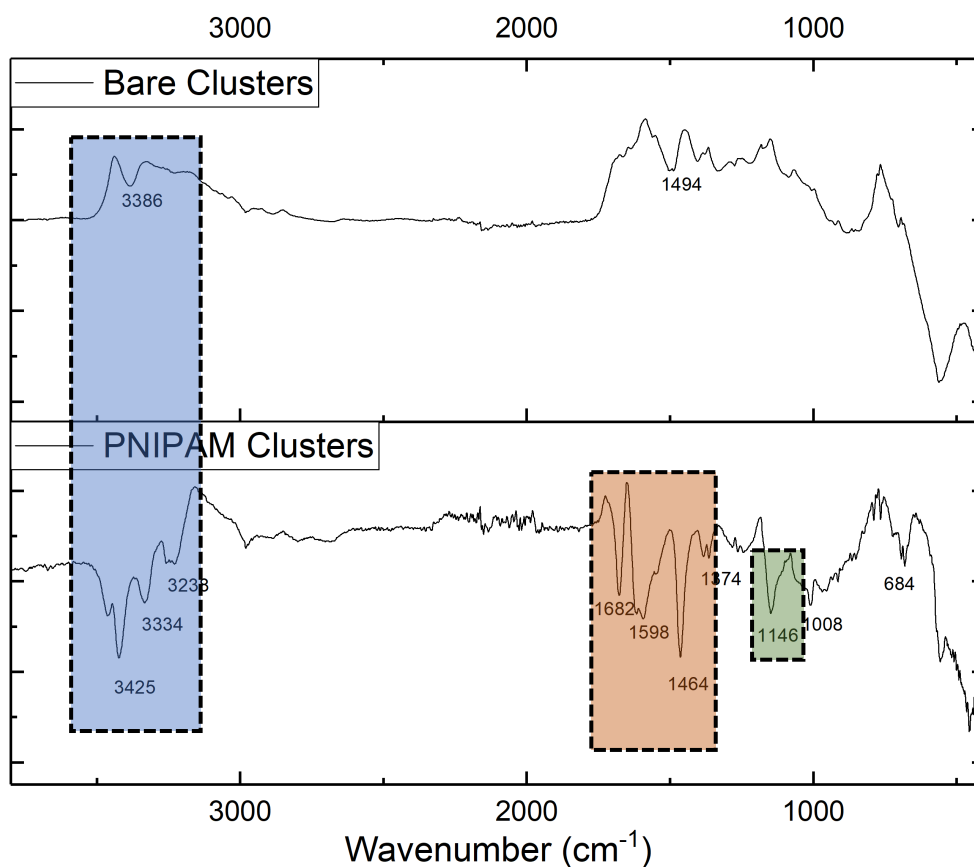


Figure 3.4.1. FT-IR spectra of bare clusters and clusters functionalised with A-PNIPAM.

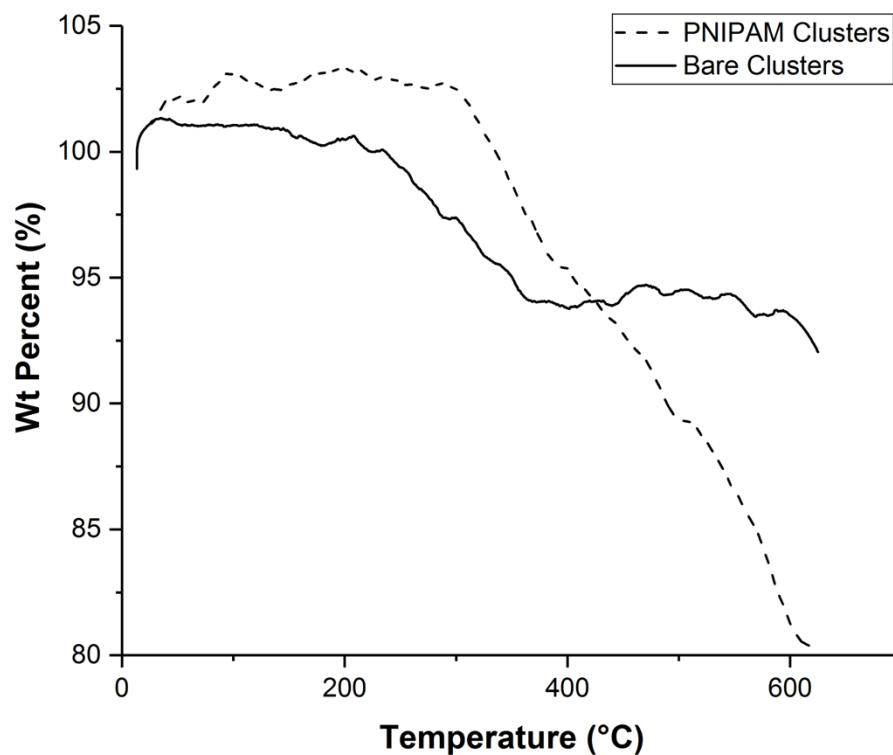


Figure 3.4.2. TGA Curves for Bare (Un-functionalised) and A-PNIPAM functionalised Clusters.

Table 3.4.1. Properties of Bare and Functionalised Clusters

Cluster Size (nm) ^a	Coating	Weight Loss (200 – 600 °C) (wt %) ^b	Inorganic Fraction (wt %) ^b	Grafting Density (Chains/nm ²) ^c	Zeta Potential (mV) ^d
91.14 ± 2.5	Bare (i.e Polypyrrole)	7.27	92.7	0.09	-38.6
102.7 ± 0.6	A-PNIPAM	19.2	80.8	1.21	-24.0

^(a)Cluster size as determined by DLS measurements. ^(b)Weight loss (200 – 600 °C) and inorganic fraction was determined by TGA. ^(c)Grafting density was calculated from the average molecular weight of the polymer (Fig. 3.3.5), weight loss (200-600 °C), inorganic fraction and average cluster diameter [Appendix].

3.5 Thermally Induced Aggregation. The count rate and size of the clusters vs temperature was monitored using DLS. The sample was allowed to equilibrate for 5 min every 5 °C before three measurements were taken at a given temperature. In Fig. 3.5.1, blue line represents the change in hydrodynamic size as a function of temperature, and the red line indicates count rate.

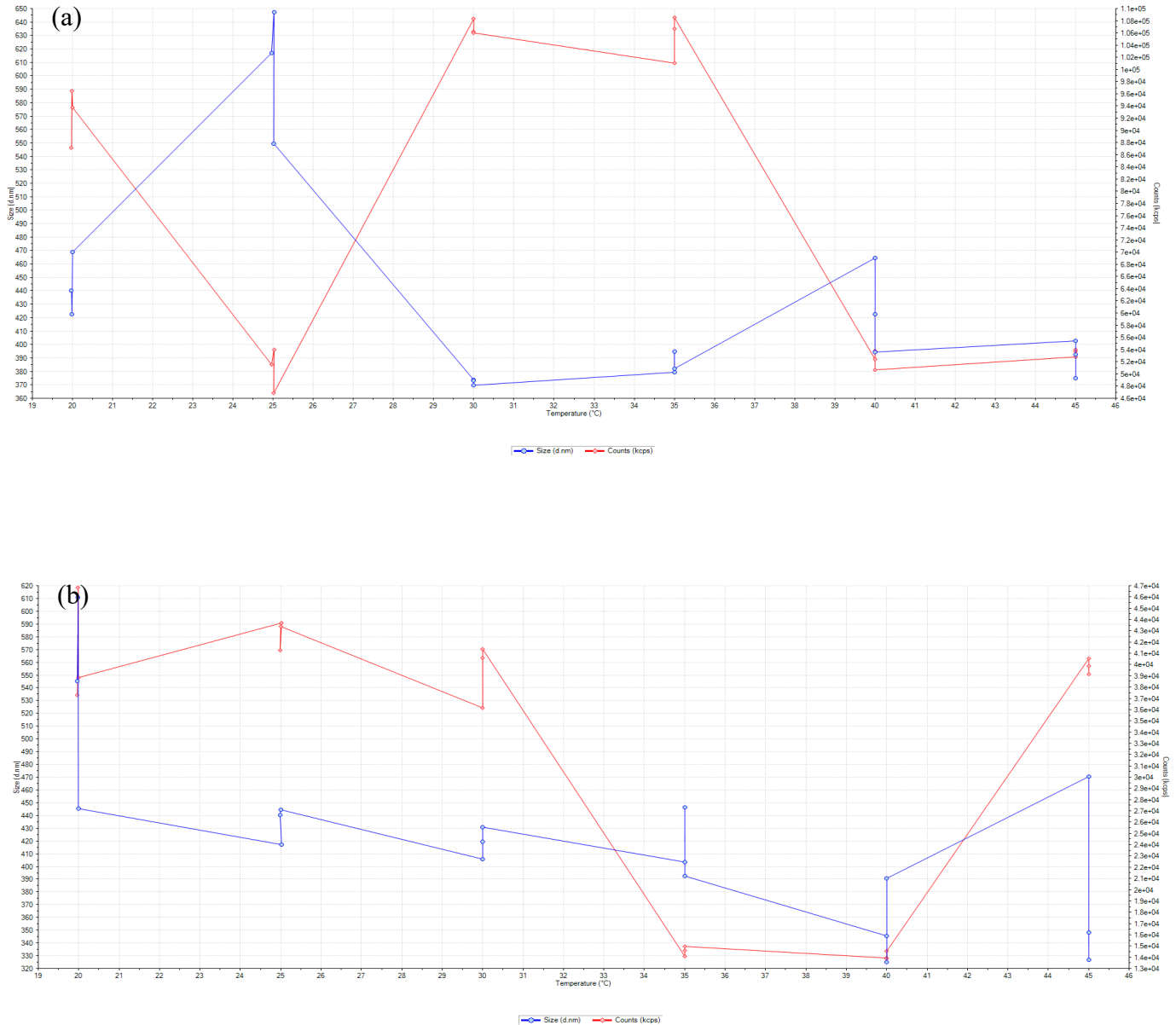


Figure 3.5.1. DLS data showing cluster size (blue line) and count rate (red line) vs temperature of (a) bare clusters and (b) A-PNIPAM clusters. Where three measurements were taken every 5 °C with an equilibration time of 5 min per measurement.

The behaviour of the particles was observed from 20 to 45 °C by measuring the count rate vs. temperature in a 1 mg/mL sample of particles. The count rate provides a sensitive measure of aggregation and provides an indicator of the point of aggregation. Upon heating, the count rate of the A-PNIPAM clusters significantly decreases above the LCST of PNIPAM in water (32 °C), followed by a slight decrease in particle size (Fig. 3.5.1b). The behaviour of these particles goes against expected results, where aggregation would be indicated by an increase in count rate followed by an increase in size. The response of the bare clusters may provide some explanation for this behaviour (Fig. 3.5.1a). The polymer coating on the bare iron oxide clusters is reported to have a glass-transition temperature (T_g) of 44 °C, meaning that at this temperature the polymer phase should soften and dilate, resulting in an increase in observed size [39]. As seen in Fig. 3.5.1a, the count rate decrease observed at 40 °C is mirrored by a decrease in size, which correlates with expected behaviour. The competing effects from the LCST of PNIPAM and the T_g of the polypyrrole polymer to which the PNIPAM is attached, may explain why the size of the A-PNIPAM clusters seems to exhibit a slow and insignificant decrease.

Although some changes in size and count rate were observed through DLS, visual inspection of the solutions (Concentration: 1 mg/mL) above the LCST of PNIPAM showed no turbidity or precipitates. According to work done by Reimhult et al. [68], PNIPAM coated nanoparticles exhibited concentration dependent aggregation and precipitation, where concentrations of 5 mg/mL resulted in observably turbid samples. It has also been established that a grafting density of >2 chains/nm² on irregularly shaped NPs is required for colloidal stability under high dilution and elevated temperatures [37]. Therefore, the combination of low grafting densities (1.21 chains/nm²), and low particle concentrations may explain the lack of observable aggregation above the LCST.

3.6 Conclusion. With some modifications to the literature synthesis we were able to obtain iron oxide NP clusters. Also, we managed to synthesise PNIPAM successfully and efficiently as discussed in section 3.3. However, modification of PNIPAM with ethylenediamine proved more difficult. Our product was identified by MALDI-TOF MS as a polymer of PNIPAM, due to its high molecular weight and a 113 Da separation of mass peaks in a series, however, the spectrum did not fit with that expected for A-PNIPAM. Furthermore,

we were unable to identify our polymer by other means, except that it displayed the LCST behaviour of PNIPAM. In an attempt to functionalise NP clusters with our PNIPAM based polymer we observed the appearance of several absorption bands associated with PNIPAM. Furthermore, TGA resulted in a 19.2 % mass loss, suggesting that our polymer had been successfully grafted onto the NP clusters. Observing the count rate and size of the clusters as a function of temperature failed to confirm if the polymer had any effect on the behaviour of the clusters. Furthermore, we could not rule out if the combined effects of the glass transition temperature of the native polypyrrole coating and the LCST of PNIPAM were the reason we did not observe a decrease in particle size with increasing temperature.

Chapter 4

Experimental

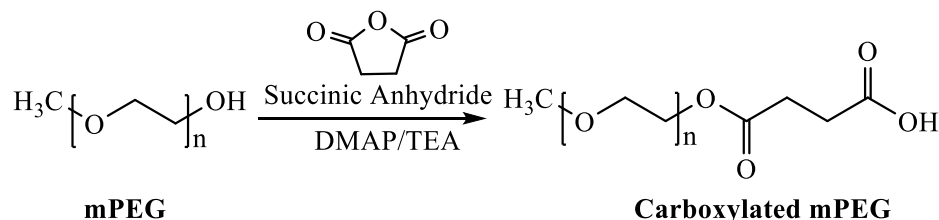
Chapter 4. Experimental

4.1. MR Fluids for Controlling Pharmaceutical Crystal Growth

Materials. Carbonyl iron (CI) microparticles consisting of $\geq 97\%$ iron particles (Sigma Aldrich), silicone oil 100 mPa, poly(ethylene glycol) methyl ether 5000 (mPEG), succinic anhydride, 4-(dimethylamino)pyridine (DMAP), triethylamine (TEA) (all from Sigma Aldrich), oleic acid (Scientific Laboratory Supplies), Carbamazepine (CBZ) 98% (Fisher Scientific).

Preparation of magnetic suspensions. Bare carbonyl iron (CI) microparticles were suspended in silicone oil (viscosity $\eta_c=100\text{mPa}$), water or toluene with 40 wt.% particle concentrations. In the case of silicone oil, the suspensions were mechanically stirred, otherwise suspensions were sonicated or mixed by vortex before each measurement.

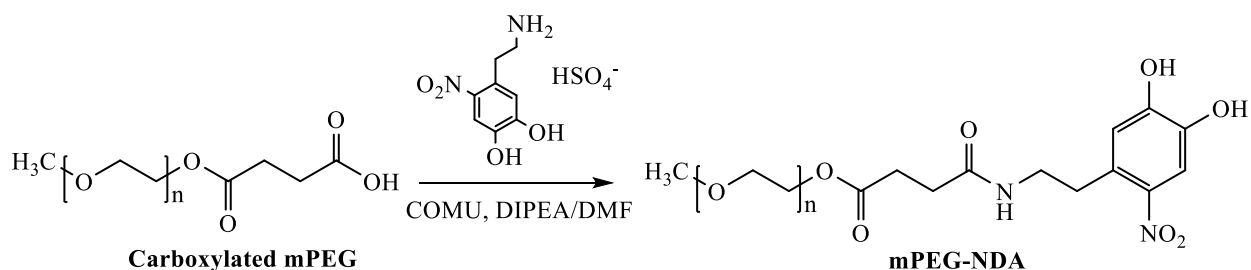
Synthesis of acid terminated mPEG. Dried mPEG (25 g, 5 mmol) was dissolved in dry THF in a two-neck round-bottomed flask. Succinic anhydride (0.60 g, 6 mmol), DMAP (0.73 g, 6 mmol), and TEA (0.84 mL, 6 mmol) were added to the solution and reacted at room temperature under a nitrogen atmosphere for 24hrs. The mixture was evaporated



by rotovap to remove solvent and the residue was dissolved in 20 mL of 1M aqueous solution of NaHCO_3 , and then cooled to $0-5^\circ\text{C}$ and filtered. The filtrate was adjusted to a pH of 4 with 6N HCl and extracted with chloroform. The obtained organic phase was washed with deionised water. The solution was then concentrated using a rotovap and precipitated into excess diethyl ether. The precipitates were filtered and dried under high vacuum to obtain a mass of 15.22 g (60%). ^1H NMR (400 MHz, CDCl_3): mPEG δ (ppm) = 3.35 ($\text{CH}_3\text{-O}$), 3.62 ($\text{O-CH}_2\text{-CH}_2\text{-O}$); acid terminated mPEG δ (ppm) = 2.62 ($\text{-CO-CH}_2\text{-CH}_2\text{-COOH}$), 3.63 ($\text{O-CH}_2\text{-CH}_2\text{-O}$), 3.45 ($\text{CH}_3\text{-O}$). ATR-FTIR: mPEG ν (cm^{-1}) = 1056 (C-O, ether), 2930 ($\text{-CH}_2\text{-}$); acid terminated mPEG ν (cm^{-1}) = 1056 (C-O, ether), 1734 (-C=O , ester), 2930 ($\text{-CH}_2\text{-}$).

MALDI-TOF MS: Mass peaks in a series separated by 44 Da (monomer weight of PEG), and peak values correspond to the addition of succinic anhydride (100 Da).

Synthesis of NDA terminated mPEG. Acid terminated mPEG (0.51 g, 0.1 mmol), COMU (51 mg, 0.12 mmol), and DIPEA (17 μ L, 0.1 mmol) were weighed in a flask and dissolved in 20 mL of DMF for 1 h under a nitrogen atmosphere. 6-nitrodopamine



hydrogensulfate (89 mg, 0.3mmol) and DIPEA (34 μ L, 0.2mmol) were stirred in 1 mL DMF and added to the above solution before being stirred at room temperature for 72 h. The solution was then acidified with a few drops of 2M HCl, precipitated in excess cold diethyl ether and collected by centrifugation. The product was dissolved in distilled water and dialyzed (membrane cutoff size of 1 kDa) against distilled water until the water remained clear (24 hr). The product was dried by rotovap to obtain a yield of 0.37 g (70%). ^1H NMR (400 MHz, CDCl_3): mPEG δ (ppm) = 2.45 (-CO-CH₂-), 2.67(-CH₂-CONH), 3.39 (CH₃-O), 3.47 (NH-CH₂-CH₂-Ar), 3.66 (O-CH₂-CH₂-O), 6.77 (CH, Ar), 7.66 (CH, Ar). ATR-FTIR: ν (cm^{-1}) = 1056 (C-O, ether), 1645 (-C=O, amide), 1734 (-C=O, ester), 2930 (-CH₂-). MALDI-TOF MS: Mass peaks in a series separated by 44 Da (monomer weight of PEG), and peak values correspond to the addition of nitrodopamine (166 Da).

Functionalisation of CI with Carboxylic Acid Moieties. Bare CI powder (5g) was dispersed by sonication in 30 mL of ethanol and purged with nitrogen. After 20 min of sonication, 1 g of acid terminated moiety (Polyethylene glycol (PEG), oleic acid, carminic acid or 1-naphthaleneacetic acid) was added to the dispersion and sonicated for 3 h at 40°C under nitrogen. The product was collected by centrifugation and re-dispersed in ethanol, acetone or water depending on the moiety used. This sequence was repeated six times to wash the particles, and then the suspension was filtered by vacuum filtration and collected after drying. Yields varied according to functionality: PEG-COOH-CI (3.98g, 78%), oleic acid-CI (4.67g, 93%), carminic acid-CI (3.40g, 68%) and 1-naphthaleneacetic acid-CI (4.40g, 88%).

Crystallisation of Carbamazepine in Toluene. A solution containing carbonyl iron (functionalised or bare) (1 g, 17.9 mmol), and carbamazepine (20 mg, 0.085 mmol) in toluene (1.724 mL, 16.2 mmol) was made up in a small 5 mL vial. Each sample was sonicated for 1 min and then heated for 10 min in a 70°C water bath. The vial was shaken vigorously for 2 sec and then secured between the poles of an EPR magnet by wedging a Styrofoam holder between the poles. The magnet was set to a field strength of 1000 G. Crystals of carbamazepine typically form 8-12 h after gelation of the magnetorheological fluid, therefore each sample is left to crystallise for 12 h. The recovery of crystals was performed by decanting the toluene solution into a filter by magnetically separating the CI particles. The particles were rinsed several times with toluene and the process was repeated to collect as many crystals as possible. Crystal yields ranged from 0.33 – 1.11 mg.

Crystallisation of Carbamazepine in Water. The process was identical to crystallisations in toluene with one modification. The solutions contained 3 mg of carbamazepine because its solubility is significantly lower in water than in toluene. Crystal yields ranged from 0.85 – 1.93 mg.

Characterisation. The size and shape of carbonyl iron particles was observed by SEM (JEOL7800F, 1-30 kV) on 200 mesh TEM grids of Formvar stabilised with carbon.

Hydrolysis of PEG Ligands for Characterisation of Functionalised CI. A sample of PEG functionalised CI (4 g) was stirred in a 50 mL alcoholic solution of sodium hydroxide (2.0 M, methanol/water 9/1) for 24 h at RT. The dispersion was centrifuged to separate out the particles, and the resulting solution was neutralised with HCl (8.3 mL, 6 M). The precipitated salt was filtered, and the filtrate was dried by rotovap, this step was repeated to remove all the salt, and the dry product was dissolved in 5 mL of D₂O. qNMR spectroscopy was performed to quantify the PEG content. A maleic acid standard in D₂O (5 mL, 0.866 mmol) was chosen because the signal would not obstruct the expected signal for PEG. Each NMR tube contained 0.5 mL of maleic acid standard and 0.4 mL of sample. Integration of the 2H signal at 6.3 ppm for maleic acid was used as a reference for the integration of the 4H signal for PEG circ. 3.54 ppm.

Maleic Acid Displacement of Carboxylic Acid Moieties for Characterisation of Functionalised CI. Functionalised CI (carminic-CI or 1-naphthaleneacetic acid-CI) was dispersed by sonication in 20 mL of ethanol. After 5 min, maleic acid (100 mg, 0.86 mmol)

was added to the dispersion and sonicated for 1 h at 40°C under nitrogen. The particles and solution were magnetically separated, and the solution was collected and dried under rotovap. The product was dissolved in 5 mL of the appropriate deuterated solvent (CDCl₃ for 1-naphthaleneacetic acid and D₂O for carminic acid) for NMR analysis.

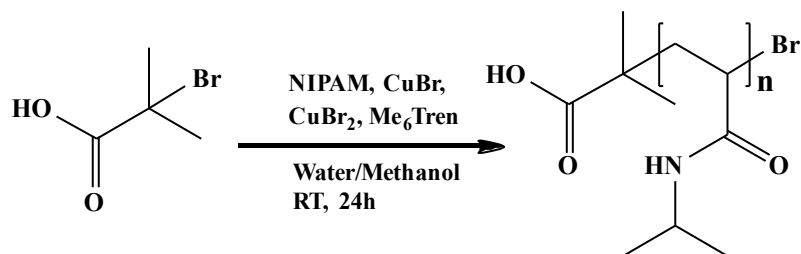
4.2. Synthesis and Surface Modification of Magnetite NP Clusters

Materials. Iron(III) chloride, poly(vinyl alcohol) (PVA, $M_w = 31,000-50,000$), hydrazine monohydrate and Me₆Tren were purchased from Sigma-Aldrich. Pyrrole-3-carboxylic acid was purchased from Alfa-Aesar (MA, USA). NIPAM was purchased from Tokyo Chemical Industry (UK).

Initial Cluster synthesis. A solution of PVA (10 mL, 0.94 mM) was stirred at 85°C for 1 h and then cooled to RT. FeCl₃ (51.9 mg, 0.32 mmol) was added to the PVA solution and stirred for 1 h at RT before adding pyrrole-3-carboxylic acid (31.1 mg, 0.28 mmol) and stirring in the dark at RT for 72 h. Finally, hydrazine monohydrate (1.07 mL, 22 mmol) was added and stirred for 72 h at 90°C in the dark to yield clustered iron oxide nanoparticle clusters. The NPs were collected by centrifugation and re-dispersed in distilled water. This process was repeated three times to wash the unmodified NP clusters.

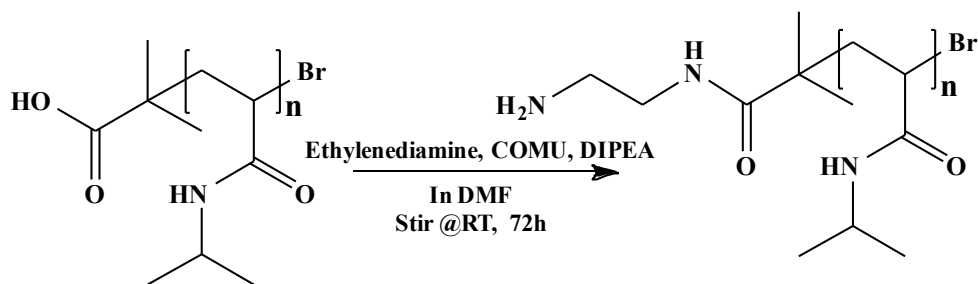
Modified Cluster Synthesis. A solution of PVA (10mL, 1.75mM) was stirred at 85°C for 1 h and then cooled to RT. All other steps remained the same as in the initial cluster synthesis.

PNIPAM Synthesis. NIPAM (1 g, 8.8 mmol), CuBr (13 mg, 0.09 mmol), CuBr₂ (2 mg, 0.009 mmol), and 2-methyl-2-bromopropionic acid (16.7 mg, 0.1 mmol) were weighed into a round-bottom flask, and 9 mL of Milli-Q water and 1 mL of methanol were added. The flask was closed with a septum and purged with nitrogen for 20 min before being cooled in an ice bath.



In a separate flask, Tris[2-(dimethylamino)ethyl]amine (Me₆Tren) (40 μL , 0.15 mmol) was dissolved in 1 mL of Milli-Q water, closed with a septum and purged with nitrogen for 20 min. The ligand solution was then injected into the monomer solution. After 24 h, the flask was opened to air, and the polymer was isolated by heating to 50°C. The supernatant was disposed, and the polymer was dried. The dried product was dissolved in THF and precipitated in cold diethyl ether. The polymer was collected by centrifugation and dried under high vacuum, to yield 926 mg (93%). ¹H NMR (400 MHz, CDCl₃): δ (ppm) = 1.12 (CH₃-C-CH₃), 2.46 (-[CH₂]-n), 3.99 (CH-Br). ATR-FTIR: ν (cm⁻¹) = 1533, 1638, 3280 (NH, amide in PNIPAM). MALDI-TOF MS: Mass peaks in a series separated by 113 Da (monomer weight of NIPAM).

Synthesis of ethylenediamine-coupled PNIPAM (A-PNIPAM). Acid terminated PNIPAM (500 mg, 0.05 mmol), COMU (34.3 mg, 0.08 mmol), and DIPEA (34.8 μL , 0.2 mmol) were weighed into a round bottom flask. This mixture was dissolved in 20 mL of DMF, purged with nitrogen and stirred at RT for 1 h. In a 5 mL round bottom flask, ethylenediamine (33.5 μL , 0.5 mmol), DIPEA (52.3 μL , 0.3 mmol), and 1 mL of DMF were added and purged with nitrogen for 20 min, before being injected into the above solution.



The resulting solution was stirred at RT for 72 h, after which it was acidified with a few drops of HCl (2 M). The polymer was precipitated by dropping the solution in cold diethyl ether and collected by centrifugation. The collected polymer was dissolved in water and dialyzed against distilled water until the water remained clear (membrane cutoff size 1 kDa). The ethylenediamine-coupled PNIPAM (A-PNIPAM) was collected by drying under a high vacuum to yield 113.5 mg (23%). Characterisations did not confirm successful conversion.

Functionalisation of Iron Oxide Clusters with A-PNIPAM. Iron oxide clusters (2.3 mg, 9.94 μmol), COMU (4.26 mg, 9.94 μmol), and DIPEA (1.73 μL , 18 μmol) were weighed into a 10 mL round bottom flask. The mixture was dissolved in 4 mL of DMF, purged with nitrogen and stirred at RT for 1 h. In a 5 mL round bottom flask, A-PNIPAM (100 mg, 9.94 μmol) and DIPEA (1 μL , 10.4 μmol) were mixed in 1 mL of DMF and purged with nitrogen for 20 min before being injected into the above solution. The resulting solution was stirred at RT for 72 h, after which the solution was exposed to air and the particles were collected by centrifugation and re-dispersed in water.

Characterisation. The size and shape of the iron oxide clusters was observed by TEM (JEOL 2010, 200 kV). The hydrodynamic diameters and zeta potentials were measured using dynamic light scattering (DLS, Malvern Zetasizer Nano ZS). The inorganic and organic fractions of the iron oxide clusters and functionalised iron oxide clusters were measured using thermogravimetry (TGA, PL Thermal Sciences STA 625). The Fourier-transform infrared (FTIR) spectra were collected using an ATR-FTIR instrument (Perkin Elmer Spectrum Two FT-IR Spectrometer). PNIPAM and A-PNIPAM polymers were characterised by ATR-FTIR, NMR and Matrix Assisted Laser Desorption/Ionisation-Time of Flight mass spectrometry (MALDI-TOF MS, Bruker UltraFlex, linear ion positive mode, 1000 shots).

Chapter 5. Conclusions and Future Work

Exploiting the magnetorheological effect, we obtained a media that successfully crystallised an active pharmaceutical ingredient. The display of field dependent viscosity and high yield stress allowed for the crystallisation of carbamazepine crystals from a supersaturated solution in toluene. Furthermore, we demonstrated control over crystal morphology by attaching functionalities to the surface of the iron particles which interacted with solute molecules and affected crystal habit. We observed that carboxylic acid moieties display a high affinity for carbonyl iron particles, and hence can be used to design MR fluids that match a wide range of crystallisation conditions. Our study further suggests that hydrogen-bonding interactions between API and particle functionalities can overcome the π - π interactions between API molecules, this results in a crystal habit shift. Likewise, functionalities with no hydrogen-bonding potential allow the π - π interactions between API molecules to dominate and hence determine crystal habit. To date, there have been no reports of crystallisations in MR fluids, or other magnetic media. Therefore, the results of this study along with future work can contribute to our understanding of crystallisations. The hope is that this work can act as step towards improving pharmaceutical crystallisations.

Although unsuccessful, our attempts to modify NP clusters with a temperature sensitive polymer will continue. The applications of such a material can have a significant and positive impact in the world of cancer therapy.

Future Work

In an effort to understand the reasons behind crystal habit shifts in MR fluids, future work should focus on the effects of hydrogen bonding interactions between particle functionalities and active pharmaceutical ingredients (API). It is important to quantify the hydrogen bond-donating potential of the particle functionality relative to the API. Quantifying this would provide a variable that can be monitored and changed in order to determine its effect on API interactions and hence crystal habit. The effect of carbonyl iron particle size should also be explored, as grafting densities for these particles would vary and hence affect interactions between API and functionality.

References

1. Zhang, X. Z.; Gong, X. L.; Zhang, P. Q.; Wang, Q. M. *J. Appl. Phys.* **2004**, *96*, 2359–2364.
2. Carlson, J.; Jolly, M. R. *Mechatronics* **2000**, *10*, 555–569.
3. Li, W. H.; Zhang, X. Z.; Du, H. *Adv. Struct. Mater.* **2013**, 357–374.
4. Rabinow, J. *AIEE Trans* **1948**, *67*, 1308–1315.
5. Behrooz, M.; Yarra, S.; Mar, D.; Pinuelas, N.; Muzinich, B.; Publicover, N. G.; Pekcan, G.; Itani, A.; Gordaninejad, F. *SPIE Smart Structures and Materials + Nondestructive Evaluation and Health Monitoring* **2016**, 9803.
6. Yamaguchi, H.; Niu, X.-D.; Ye, X.-J.; Li, M.; Iwamoto, Y. *J. Magn. Magn. Mater.* **2012**, *324*, 3238–3244.
7. Kumbhar, B. K.; Patil, S. R.; Sawant, S. M. *JESTECH* **2015**, *18*, 432–438.
8. Danan, H.; Herr, A.; Meyer, A. J. P. *J. Appl. Phys.* **1968**, *39*, 669–670.
9. Coey, J. M. D. *Magn. Magn. Mater.*; Cambridge University Press: Cambridge **2015**, 7–11
10. Genç, S.; Phulé, P. P. *Smart Mater. Struct.* **2002**, *11*, 140–146.
11. Olabi, A.; Grunwald, A. *Mater. & Des.* **2007**, *28*, 2658–2664.
12. Carlson, J. D. *International Conference on Electrorheological (ER) Fluids and Magneto-rheological (MR) Suspensions* **2001**, 1–7.
13. Winslow, W. M. *J. Appl. Phys.* **1949**, *20*, 1137–1140.
14. Genç S. Synthesis and Properties of Magnetorheological (MR) Fluids. Doctoral Dissertation, University of Pittsburgh **2003**, 23–40.
15. Yu, W. *Encyclopedia of Polymer Science and Technology* **2013**, 1–15.
16. Carlson, D.; Clarke, M. *Mater. Tech.* **1998**, *13*, 96–99.
17. Shen, Y.; Golnaraghi, M. F.; Heppler, G. R. *J. Intel. Mater. Sys. Struct.* **2004**, *15*, 27–35.
18. Deng, H.-X.; Gong, X.-L.; Wang, L.-H. *Smart Mater. Struct.* **2006**, *15*.
19. Wright, R. I.; Kidner, M. R. F. *Modal Analysis* **2004**, *10*, 1221–1237.
20. Khan, Z. H.; Kumar, A.; Husain, S.; Husain, M. *Advances in Nanomaterials Advanced Structured Materials* **2016**, 1–23.

21. Zhu, K.; Ju, Y.; Xu, J.; Yang, Z.; Gao, S.; Hou, Y. *Acc. Chem. Res.* **2018**, *51*, 404–413.
22. Papaefthymiou, G. C. *Nano Today* **2009**, *4*, 438–447.
23. Jun, Y.-W.; Huh, Y.-M.; Choi, J.-S.; Lee, J.-H.; Song, H.-T.; Kim, Yoon, S.; Kim, K.-S.; Shin, J.-S.; Suh, J.-S.; Cheon, J. *J. Am. Chem. Soc.* **2005**, *127*, 5732–5733.
24. Xu, C. Modification of Superparamagnetic Nanoparticles for Biomedical Applications. Doctoral Dissertation, Brown University **2009**, 1–24.
25. Suslick, K. S.; Fang, M.; Hyeon, T. *J. Am. Chem. Soc.* **1996**, *118*, 11960–11961.
26. Xu, Z.; Shen, C.; Hou, Y.; Gao, H.; Sun, S. *Chem. Mater.* **2009**, *21*, 1778–1780.
27. Sun, S.; Zeng, H. *J. Am. Chem. Soc.* **2002**, *124*, 8204–8205.
28. Zhang, L.; Wu, J.; Liao, H.; Hou, Y.; Gao, S. *Chem. Comm.* **2009**, No. 29, 4378–4380.
29. Zeng, Y.; Hao, R.; Xing, B.; Hou, Y.; Xu, Z. *Chem. Comm.* **2010**, *46*, 3920–3922.
30. Hou, Y.; Xu, Z.; Sun, S. *Angewandte Chemie International Edition* **2007**, *46*, 6329–6332.
31. Coey, J. M. D. *J. Appl. Phys.* **2003**, *93*, 8224–8229.
32. Néel, L. *Journal de Physique et le Radium* **1959**, *20*, 215–221.
33. Gobbo, O. L.; Sjaastad, K.; Radomski, M. W.; Volkov, Y.; Prina-Mello, A. *Theranostics* **2015**, *5*, 1249–1263.
34. Lee, N.; Yoo, D.; Ling, D.; Cho, M. H.; Hyeon, T.; Cheon, J. *Chem. Rev.* **2015**, *115*, 10637–10689.
35. Chou, L. Y. T.; Ming, K.; Chan, W. C. W. *Chem. Soc. Rev.* **2011**, *40*, 233–245.
36. Chen, K.; Xu, X.; Guo, J.; Zhang, X.; Han, S.; Wang, R.; Li, X.; Zhang, J. *Biomacromolecules* **2015**, *16*, 3574–3583.
37. Zirbs, R.; Lassenberger, A.; Vonderhaid, I.; Kurzhals, S.; Reimhult, E. *Nanoscale* **2015**, *7*, 11216–11225.
38. Kurzhals, S.; Zirbs, R.; Reimhult, E. *ACS Appl. Mater. Interfaces* **2015**, *7*, 19342–19352.
39. Hayashi, K.; Nakamura, M.; Miki, H.; Ozaki, S.; Abe, M.; Matsumoto, T.; Sakamoto, W.; Yogo, T.; Ishimura, K. *Theranostics* **2014**, *4*, 834–844.
40. Reimhult, E. *New Biotechnology* **2015**, *32*, 665–672.
41. Amstad, E.; Kohlbrecher, J.; Müller Elisabeth; Schweizer, T.; Textor, M.; Reimhult, E. *Nano Letters* **2011**, *11*, 1664–1670.

42. Chikazumi, S.O. and Charap, S.H., **1964**, Physics of Magnetism. John Wiley, New York.
43. Shekunov, B.; York, P. *J. Cryst. Growth* **2000**, *211*, 122–136.
44. Erdemir, D.; Lee, A. Y.; Myerson, A. S. *Acc. Chem. Res.* **2009**, *42*, 621–629.
45. Karpinski, P. H. *Chem. Eng. Technol.* **2006**, *29*, 233–237.
46. Bučar, D.-K.; Lancaster, R. W.; Bernstein, J. *Angewandte Chemie International Edition* **2015**, *54*, 6972–6993.
47. Threlfall, T. *Org. Process Res. Dev.* **2003**, *7*, 1017–1027.
48. Censi, R.; Di Martino, P. *Molecules* **2015**, *20*, 18759–18776.
49. Bauer, J.; Spanton, S.; Henry, R.; Quick, J.; Dziki, W.; Porter, W.; Morris, J. *Pharm. Res.* **2001**, *18*, 859–866.
50. Rietveld, I. B.; Céolin, R. *J. Pharm. Sci.* **2015**, *104*, 4117–4122.
51. Hilfiker, R.; Hilfiker, R. *Polymorphism in the Pharmaceutical Industry*; Wiley-VCH: Weinheim, **2006**; pp 309–332.
52. Bansal, A. K.; Kumar, L.; Amin, A. *Pharm. Tech.* **2008**, *32*.
53. Gao, Z.; Rohani, S.; Gong, J.; Wang, J. *Eng.* **2017**, *3*, 343–353.
54. Liesegang, R.E. *Naturwiss. Wochenschr.*, **1896**, *11*, 353–362
55. Steed, J. W. *Chem. Commun.* **2011**, *47*, 1379–1383.
56. Kumar, D. K.; Steed, J. W. *Chem. Soc. Rev.* **2014**, *43*, 2080–2088.
57. Foster, J. A.; Piepenbrock, M.-O. M.; Lloyd, G. O.; Clarke, N.; Howard, J. A. K.; Steed, J. W. *Nat. Chem.* **2010**, *2*(12), 1037–1043.
58. Diao, Y.; Whaley, K. E.; Helgeson, M. E.; Woldeyes, M. A.; Doyle, P. S.; Myerson, A. S.; Hatton, T. A.; Trout, B. L. *J. Am. Chem. Soc.* **2012**, *134*, 673–684.
59. López-López, M. T.; Kuzhir, P.; Laciš, S.; Bossis, G.; González-Caballero, F.; Durán, J. D. G. *J. Phys.: Condens. Matter* **2006**, *18*, S2803–S2813.
60. Phulé, P. P.; Ginder, J. M.; Jatkar, A. D. *MRS Proceedings* **1996**, *459*, 99–104.
61. Karkoub, M. A.; Zribi, M. *Int. J. Syst. Sci.* **2006**, *37*, 35–44.
62. Hu, G.; Zhou, W.; Li, W. *Smart Mater. Struct.* **2015**, *24*, 087001.
63. Ashtiani, M.; Hashemabadi, S.; Ghaffari, A. *J. Magn. Magn. Mater.* **2015**, *374*, 716–730.
64. Climent, E.; Maxey, M. R.; Karniadakis, G. E. *Langmuir* **2004**, *20*, 507–513.

65. Huang, Y.; Jiang, Y.; Yang, X.; Xu, R. *J. Magn.* **2015**, *20*(3), 317–321.
66. Gorodkin, S. R.; James, R. O.; Kordonski, W. I. *J. Phys.: Conference Series* **2009**, *149*, 012051.
67. Yoon, K.; Kang, H. C.; Li, L.; Cho, H.; Park, M.-K.; Lee, E.; Bae, Y. H.; Huh, K. *M. Polym. Chem.* **2015**, *6*, 531–542.
68. Kurzhals, S.; Zirbs, R.; Reimhult, E. *ACS Appl. Mater. Interfaces* **2015**, *7*, 19342–19352.
69. Amstad, E.; Gehring, A. U.; Fischer, H.; Nagaiyanallur, V. V.; Hähner, G.; Textor, M.; Reimhult, E. *J. Phys. Chem. C* **2010**, *115*, 683–691.
70. Lassenberger, A.; Bixner, O.; Gruenewald, T.; Lichtenegger, H.; Zirbs, R.; Reimhult, E. *Langmuir* **2016**, *32*, 4259–4269.
71. Huang, Y.; Jiang, Y.; Yang, X.; Xu, R. *J. Magn.* **2015**, *20*, 317–321.
72. Wu, W.; He, Q.; Jiang, C. *Nanoscale Res. Lett.* **2008**, *3*, 397–415.
73. Müller-Maatsch, J.; Gras, C. *Handbook on Natural Pigments in Food and Beverages* **2016**, 385–428.
74. Harris, R. K.; Ghi, P. Y.; Puschmann, H.; Apperley, D. C.; Griesser, U. J.; Hammond, R. B.; Ma, C.; Roberts, K. J.; Pearce, G. J.; Yates, J. R.; Pickard, C. J. *Org. Process Res. Dev.* **2005**, *9*, 902–910.
75. Lang, M.; Kampf, J. W.; Matzger, A. J. *J. Pharm. Sci.* **2002**, *91*, 1186–1190.
76. Kobayashi, Y.; Ito, S.; Itai, S.; Yamamoto, K. *Int. J. Pharm.* **2000**, *193*, 137–146.
77. Bonin, C. J.; Amar, A.; Pusiol, D. J. *arXiv:1003.3001v1* **2010**, 1–24. [physics.chem-ph]
78. Grzesiak, A. L.; Lang, M.; Kim, K.; Matzger, A. J. *J. Pharm. Sci.* **2003**, *92*, 2260–2271.
79. Xiao, J.; Zhu, Y.; Liu, Y.; Liu, H.; Zeng, Y.; Xu, F.; Wang, L. *Cryst. Growth Des.* **2008**, *8*, 2887–2891.
80. Lloyd, G. O.; Steed, J. W. *Nat. Chem.* **2009**, *1*, 437–442.
81. Hayashi, K.; Sato, Y.; Sakamoto, W.; Yogo, T. *ACS Biomater. Sci. Eng.* **2016**, *3*, 95–105.
82. Li, G. C.; Shiu, E. C.; Hahn, G. M. *Int. J. Radiat. Oncol.* **1980**, *6*, 577–582.
83. Mørup, S.; Hansen, M. F.; Frandsen, C. *Beilstein J. Nanotechnol.* **2010**, *1*, 182–190.

84. Golovin, Y.; Golovin, D.; Klyachko, N.; Majouga, A.; Kabanov, A. *J. Nanoparticle Res.* **2017**, *19*.
85. Somcynsky, T. *Polym. Eng. Sci.* **1982**, *22*, 58–63.
86. Hong, J.-Y.; Yoon, H.; Jang, J. *Small* **2010**, *6*, 679–686.
87. El-Faham, A.; Funosas, R. S. S.; Prohens, R.; Albericio, F. *Chem. Eur. J.* **2009**, *15*, 9404–9416.
88. Cohen, S. L.; Chait, B. T. *Anal. Chem.* **1996**, *68*, 31–37.
89. Marie, A.; Fournier, F.; Tabet, J. C. *Anal. Chem.* **2000**, *72*, 5106–5114.

Appendix

Estimating the mass of PEG polymer required for functionalisation of carbonyl iron

Particle Size = 2 μm

Estimated grafting density = 2×10^6 chains/ μm^2

Density of carbonyl iron = 7.86×10^{-12} g/ μm^3

Volume of particle = $\frac{4}{3}\pi r^3 = \frac{4}{3} \cdot \pi \cdot 1^3 \mu\text{m}^3$

Surface area of particle = $4\pi r^2 = 4 \cdot \pi \cdot 1^2 \mu\text{m}^2$

Mass of polymer = 5488

Mass of polymer chains = $\frac{2 \times 10^6 \cdot 4\pi \cdot 5488 \text{g/mol}}{6.022 \times 10^{23}} = 2.29 \times 10^{-13}$ g

Mass of particle = $\left(\frac{4}{3}\pi\right) \cdot (7.86 \times 10^{-12}) = 3.29 \times 10^{-11}$ g

Mass of particle/Mass of chains = $\frac{3.29 \times 10^{-11} \text{g}}{2.29 \times 10^{-13} \text{g}} = 144$

Mass of polymer required for 1 g of carbonyl iron = $\frac{1 \text{ g}}{144} = 6.94$ mg

Calculating the grafting density of PEG on carbonyl iron from qNMR

Particle Size = 2 μm

Density of carbonyl iron = 7.86×10^{-12} g/ μm^3

Volume of Particle = $\frac{4}{3}\pi r^3 = \frac{4}{3} \cdot \pi \cdot 1^3 \mu\text{m}^3$

Surface Area of Particle = $4\pi r^2 = 4 \cdot \pi \cdot 1^2 \mu\text{m}^2$

Mass of PEG from qNMR = 0.54 ± 0.06 mg

Number of polymer chains = $\frac{5.4 \times 10^{-4} \text{g}}{5486 \text{g/mol}} \cdot 6.022 \times 10^{23} = 5.93 \times 10^{16}$

Number of particles = $\frac{4\text{g}}{\left(\frac{4}{3}\pi \cdot 7.86 \times 10^{-12}\right)} = 1.21 \times 10^{11}$

Chains/Particle = $\frac{5.82 \times 10^{16}}{1.21 \times 10^{11}} = 4.90 \times 10^5$

$$\text{Chains}/\mu\text{m}^2 = \frac{4.81 \times 10^5}{4\pi} = 3.90 \times 10^4$$

Estimating the efficiency of functionalisation from UV-Visible Spectroscopy data

$$\text{Conc}_{0 \text{ min}} = 2.13 \times 10^{-4} \text{ M}$$

$$\text{Abs}_{0 \text{ min}} = 0.561$$

$$\text{Abs}_{20 \text{ min}} = 0.316$$

$$\text{Conc}_{20 \text{ min}} = \left(\frac{\text{A}_{20 \text{ min}}}{\text{A}_{0 \text{ min}}} \right) \cdot \text{Conc}_{0 \text{ min}}$$

$$\text{Conc}_{20 \text{ min}} = \left(\frac{0.316}{0.561} \right) \cdot 2.13 \times 10^{-4} \text{ M} = 1.20 \times 10^{-4} \text{ M}$$

$$\text{Conc}_{20 \text{ min}} - \text{Conc}_{0 \text{ min}} = 9.30 \times 10^{-4} \text{ M}$$

$$\text{C}_{\text{grafted}} = 9.30 \times 10^{-4} \text{ M} \cdot 0.001 \text{ L} \cdot 5488 \text{ g/mol} = 5.1 \times 10^{-4} \text{ g}$$

$$\text{C}_{\text{grafted}} = 0.51 \text{ mg}$$

$$\text{Estimated C}_{\text{grafted}} = 1 \text{ g}/144 = 6.94 \times 10^{-3} \text{ g}$$

$$\text{Grafting Efficiency} = \frac{0.51}{6.94} \cdot 100 = 7.3\%$$

Grafting Density Calculations for Magnetite NP Clusters

Bare Clusters

$$\text{Cluster Size} = 91.14 \text{ nm}$$

$$\text{Density of Iron Oxide (Magnetite)} = 5.18 \times 10^{-21} \text{ g/nm}^3$$

$$\text{Mass Loss (From TGA)} = 0.160032 \text{ mg}$$

$$\text{Inorganic Fraction} = 2.03997 \text{ mg}$$

$$\text{Volume of Clusters} = \frac{4}{3} \pi r^3 = \frac{4}{3} \cdot \pi \cdot 45.57^3 = 3.9639 \times 10^5 \text{ nm}^3$$

$$\text{Surface Area of Clusters} = 4\pi r^2 = 4 \cdot \pi \cdot 45.57^2 = 2.6096 \times 10^4 \text{ nm}^2$$

$$\text{Mass of Polymer PVA} = 41,000$$

$$\text{Number of Polymer Chains} = \frac{0.160032 \times 10^{-3}}{41,000} \cdot 6.022 \times 10^{23} = 2.351 \times 10^{15}$$

$$\text{Number of Particles} = \frac{2.03997 \times 10^{-3}}{(3.9639 \times 10^5 \text{ nm}^3)(5.18 \times 10^{-21} \text{ g/nm}^3)} = 9.94 \times 10^{11}$$

$$\text{Chains per Particle} = \frac{2.351 \times 10^{15}}{9.94 \times 10^{11}} = 2370 \text{ chains/particle}$$

$$\frac{\text{Chains}}{\text{nm}^2} = \frac{2370}{2.61 \times 10^4} = 0.091 \text{ chains/nm}^2$$

A-PNIPAM Clusters

Cluster Size = 102.7 nm

Density of Iron Oxide (Magnetite) = $5.18 \times 10^{-21} \text{ g/nm}^3$

Mass Loss (From TGA) = 0.3836 mg

Inorganic Fraction = 1.6164 mg

$$\text{Volume of Clusters} = \frac{4}{3} \pi r^3 = \frac{4}{3} \cdot \pi \cdot 51.35^3 = 5.672 \times 10^5 \text{ nm}^3$$

$$\text{Surface Area of Clusters} = 4\pi r^2 = 4 \cdot \pi \cdot 51.35^2 = 3.314 \times 10^4 \text{ nm}^2$$

Mass of A-PNIPAM = 11,058 g/mol

$$\text{Number of Polymer Chains} = \frac{0.3836 \times 10^{-3}}{11,058} \cdot 6.022 \times 10^{23} = 2.089 \times 10^{16}$$

$$\text{Number of Particles} = \frac{1.6164 \times 10^{-3}}{(5.672 \times 10^5 \text{ nm}^3)(5.18 \times 10^{-21} \text{ g/nm}^3)} = 5.502 \times 10^{11}$$

$$\text{Chains per Particle} = \frac{2.089 \times 10^{16}}{5.502 \times 10^{11}} = 37,970 \text{ chains/particle}$$

$$\frac{\text{Chains}}{\text{nm}^2} = \frac{37,970}{3.314 \times 10^4} = 1.206 \text{ chains/nm}^2$$